EXPERIMENTAL STUDY OF THE RESIDUAL STRESS-INDUCED SELF-ASSEMBLY OF MEMS STRUCTURES DURING DEPOSITION

A Dissertation

by

SANG-HYUN KIM

Submitted to the Office of Graduate Studies of
Texas A&M University
in partial fulfillment of the requirements for the degree of

DOCTOR OF PHILOSOPHY

August 2005

Major Subject: Aerospace Engineering

EXPERIMENTAL STUDY OF THE RESIDUAL STRESS-INDUCED SELF-ASSEMBLY OF MEMS STRUCTURES DURING DEPOSITION

A Dissertation

by

SANG-HYUN KIM

Submitted to the Office of Graduate Studies of
Texas A&M University
in partial fulfillment of the requirements for the degree of

DOCTOR OF PHILOSOPHY

Approved by:

Chair of Committee,	James G. Boyd IV
Committee Members,	Johnny Hurtado
	Won-jong Kim
	Ibrahim Karaman
Head of Department,	Helen L. Reed

August 2005

Major Subject: Aerospace Engineering

ABSTRACT

Experimental Study of the Residual Stress-Induced
Self-Assembly of MEMS Structures During Deposition. (August 2005)
Sang-Hyun Kim, B.S.; M.S., Pusan National University, Pusan, Korea
Chair of Advisory Committee: Dr. James G. Boyd

The possibility of using residual stresses favorably as a means of self-assembling MEMS during material deposition is experimentally investigated. Two atomic force microscope cantilevers are placed in contact at their free ends. Material is isothermally electroplated onto one (the deposition) cantilever, but no material is deposited onto the other (spring) cantilever. The deposited layer contains residual stresses that deform the deposition cantilever. The deposition cantilever in turn deforms the spring cantilever, thereby doing work in the spring cantilever and proving that the two structures can self-assemble during deposition processing. An insoluble nickel electroplating process and an all-sulfate nickel solution are used for the deposition. The deflection of the self-assembled cantilevers is measured in-situ as a function of the deposited thin film thickness through the optical method of atomic force microscopy.

The experimental results are compared to an analytical model which consists of Euler-Bernoulli beam theory that is modified to account for moving boundaries as the

material is deposited. The model accounts for the through-thickness variation of the intrinsic strain during the electroplating. Closed-form solutions are not possible, but numerical solutions are plotted for the cantilever deflection and work on the spring cantilever as functions of the deposition thickness.

With love,

this dissertation is dedicated to

my parents who have always sacrificed all their life for their children,

my parents-in-law who presented me more than a lovely wife, and

my wife Kuiyeon,

my adorable kid Junghoon.

ACKNOWLEDGMENTS

I wish to thank all of the people whose assistance, support and love have contributed by whatever amount to this research effort. I would first like to thank my advisor, Dr. James G. Boyd for his generous guidance and encouragement. Without his academic advice and support, this work would not have been completed. I also thank Dr. Johnny Hurtado, Dr. Won-jong Kim and Dr. Ibrahim Karaman who served as my committee members and Dr. Zoubeida Ounaies who served as a committee member substitute on my dissertation defense. All of them gave me huge impressions from their life for being virtuous as well as academic achievements in school. I would also like to express my gratitude to Dr. William Lackowski at MCF who helped me with various problems and issues in AFM and experimental troubleshooting. The following people deserve my sincere thanks for their expertise and assistance: Yullia Vasilyeva and Shyamashree Chatterjee at MCF and Rick Littleton at MIC.

I would like to express my heartfelt gratitude to my parents, without whom I would not be what I am today. Their love and encouragement have been invaluable. In addition, I especially need to thank my parents-in-law for their love, trust and support throughout the study.

I thank my wife, Kuiyeon, for her love, patience, prayers and encouragement. She has been my strongest source of strength and inspiration. My burden was lighter because she carried half of it. My son, Junghoon has been another blessing to me. I would like to

tell my son, “ You don’t have to miss your daddy at night any more. I will spend much more time with you from now on.”

Finally I would like to express my sincere gratitude to God who is always with me and leads the path that I will walk.

TABLE OF CONTENTS

Page

Page

Page

LIST OF FIGURES

Page

Page

Page

Page

LIST OF TABLES

Page

I. INTRODUCTION

Micro Electromechanical Systems (MEMS) are made by a sequence of material deposition (sputtering, evaporation, CVD, spincoating, electroforming) and material removal steps (reactive ion etching, wet etching). In many cases, the processing method required for one type of material (metal, ceramic, or polymer) is incompatible with the processing method required of a second type of material. In this case, it is necessary to separately fabricate the two MEMS components and then assemble them. In addition, it is sometimes necessary to assemble MEMS structures to make an out-of-plane device.

Hence, there is an incentive to develop new assembly techniques for MEMS. Self-assembly may be an efficient and cost effective method of assembling MEMS and Nano Electromechanical Systems (NEMS). One such technique of self-assembly is the possibility of using residual stresses favorably as a means of self-assembly. In order to explore this possibility it is important to understand the behavior of thin films and their response residual stresses.

Researchers have analytically studied the influence of intrinsic stresses on micro-structures during deposition and etching. However, no experimental study has been done.

The following sections provide a brief background on MEMS, self-assembly, and residual stresses in thin films.

This thesis follows the style and format of *Journal of Microelectromechanical Systems*.

A. Assembly in Micro Electromechanical Systems

Surface micromachining is one of the most common methods for manufacturing MEMS. Surface micromachining involves the deposition of several very thin layers (approximately one micrometer) of material that combine to form structures and mechanically moving parts. Because thin film deposition is inherently a planar technology, a fundamental problem with surface micro-machining is its inability to produce highly three-dimensional (3-D), or out-of-plane, structures.

A common solution to this limitation is the use of pop-up structures that can be lifted or rotated out-of-plane, and even assembled and locked into place [1]. A disadvantage of these structures is that they sometimes need to be manually assembled. Fig. 1 shows the SEM image of a microlens manually assembled after fabrication. Manual assembly usually consists of rotating the plates by hand using micromanipulators. It also requires multiple structural and sacrificial layers to fabricate the hinge structures. While this may be useful for assembling a few discrete devices, it does not lend itself to efficient assembly of large numbers of components or of complex systems. Manual assembly is not practical for mass assembly and fabrication. Microstructures may also be damaged by the micromanipulators.

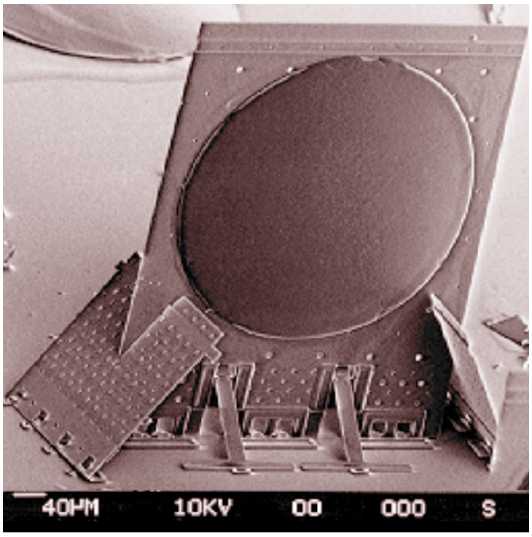

Fig. 1. SEM image of the manually assembled microlens [1]

Another assembly method is to add MEMS actuators to a design so the actuators can assemble the MEMS after the planar fabrication is complete. This method also uses the pop-up structures and the hinged components. The pop-up structures, the hinged components, and the actuators are initially coplanar, and the structures can be lifted or rotated by using the actuators which are mechanically linked to the structures. Approaches using electrical resistance thermal actuators [2], electrostatic actuators [3]-[6] and magnetic actuator [7] have been reported. Fig. 2 shows SEM images of assembled MEMS using electrostatic comb drive actuators. As shown in Fig. 2, a scanning micromirror (a) or xyz stage (b), which are hinge-connected to the comb drive actuators, is fabricated on the substrate. When the voltage is applied to the comb drive actuator, the linear movement of the comb drive actuator makes the structures lifted or rotated. However, actuator-driven assembly is inefficient because the actuators increase

the device complexity and cost. Most actuators also occupy a relatively large chip area (on the order of $100\mu m$ x $100\mu m$) in addition to the structure itself.

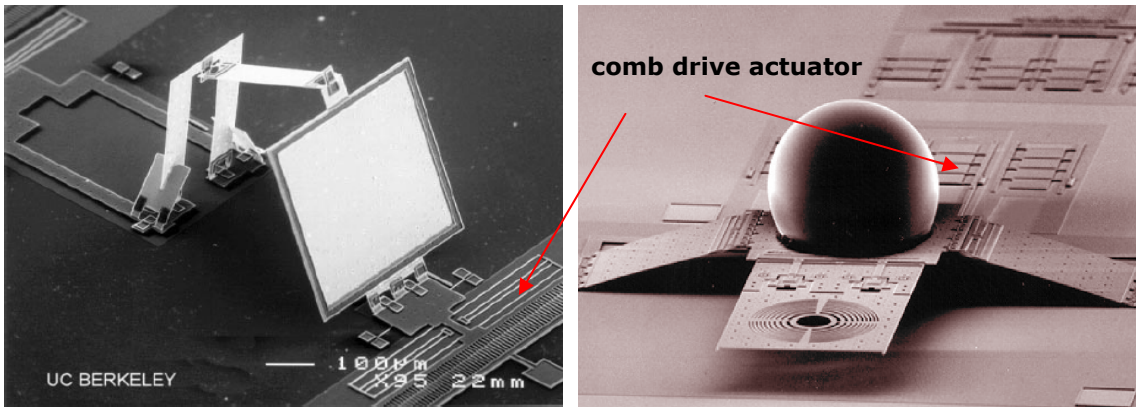

(a) (b)

Fig. 2. SEM image of assembly using actuation mechanism (a) scanning micromirror [3] (b) xyz stage [5]

Magnetic forces including plastic deformation magnetic assembly have also been used to assemble microstructures [8], and this required the incorporation of a magnetic material on the sections of the structures requiring assembly. A stress-induced curved bimorph cantilever was utilized to self-assemble a movable optical microshutter which has been fabricated by polysilicon surface micromachining [9].

B. Self-Assembly of MEMS

A variety of self-assembly processes have been demonstrated on a microscopic scale in an effort to eliminate the need for manual or robotic assembly of micromachined structures for multiple components.

Surface tension forces have been used to self-assemble MEMS. The first self-assembly using surface tension was proposed by Syms [10], [11]. In this approach the surface tension properties of molten solder or glass was used as the assembly mechanisms. The solder method involves using a standard hinged plate with a specific area metalized as solder wettable pads. Once the solder is in place, it is heated to its melting point, and the force produced by the natural tendency of liquids to minimize their surface energy (and thereby surface area) rotates the free plate out of plane. The studies carried out by Syms focused on fabrication techniques assisted by a simple model. Later Harsh *et al* reported an in-depth characterization of solder self-alignment for 3-D MEMS through modeling and experimental studies [12], [13]. Meltable pads of thick photoresist have been used to self-assemble micromirrors by utilizing surface tension forces [14], [15]. Thermally shrunk polyimide joints [16] have also been used for 3-D assembly. Fig. 3 shows the SEM image of the solder self-assembled hinge plate [12].

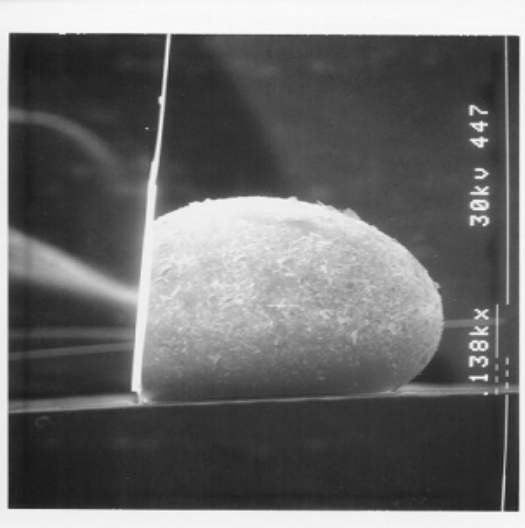

Fig. 3. SEM image of the solder self-assembled hinge plate [12]

C. Self-Assembly of MEMS Using Residual Stresses

Residual stresses commonly arise during the fabrication of MEMS. Residual stresses are stresses that exist within a body even when there are no externally applied forces on the body. There are two types of residual stresses: extrinsic stress and intrinsic stress [17]-[22]. Extrinsic stresses due to externally applied stimuli such as a temperature change. Thermal stresses are the most common form of extrinsic stresses and they arise either in structures with inhomogeneous thermal expansion coefficients subjected to a uniform temperatures change or in a homogeneous structure exposed to a thermal gradient.

Intrinsic stresses originate from lattice mismatch strains, substitutional or interstitial impurities, and growth processes during deposition processes used in microfabrication including chemical and physical vapor deposition, evaporation, sputtering, and electro deposition. Intrinsic stresses also develop during the film nucleation and are called growth stresses. A difference, or "misfit", in the lattice constants of the film and the substrate results in an accommodation of the first atomic planes of the film to the parameters of substrate, the lattice is deformed, and dislocations may arise. Dislocations as well as other lattice defects, whether point defects or other ones including impurity atoms, variations of interatomic spacings with crystal size, cause intrinsic stresses due to the local lattice expansion or contraction. Transformation stresses occur when part of a material undergoes a volume change during a phase transformation.

An important role is played by grain boundaries; the stress increases during boundary coalescence. Also surface effects are involved [22]. However, both these

mechanisms are as yet poorly understood. Different kinds of origin of stresses can prevail at different deposition methods.

Fig. 4 illustrates a model for the generation of internal stress during deposition of a film. The stress-free widths of the film and substrate are shown in the top part of each figure. These are the widths that the film and substrate would have if they were free, or not joined together. However, when the film is deposited onto the substrate the two layers reach a common width. If the free film width is less (more) than the free substrate width, then the deposited film will be in tension (compression) and the substrate will be in compression (tension), as indicated by the arrows in Fig. 4.

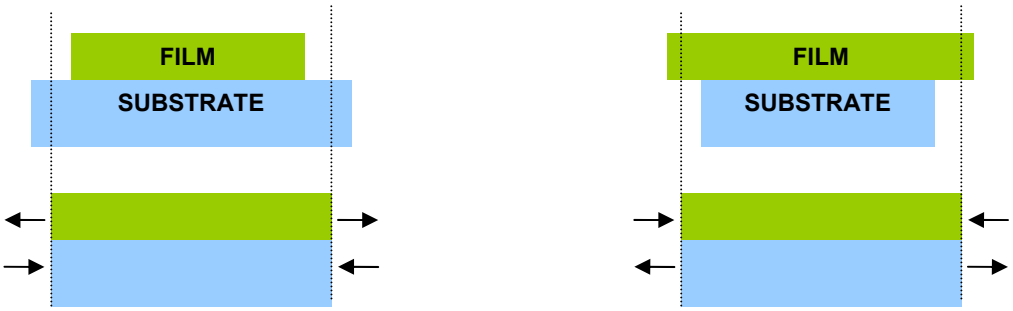

(a) Film is stretched and bent up

(b) Film is shrunk and bent down

Fig. 4. Sequence of events leading to (a) residual tensile stress in film; (b) residual compressive stress in film

The mechanical response of thin-film structures is affected by residual stress, even if structures do not fail. For instance, a residual bending moment will warp released structures such as cantilevers [23], as shown in Fig. 5. Thus, intrinsic stresses usually have deleterious effects in thin film processing. For example, stresses can cause

substrate curvature and in-plane distortions leading to alignment errors in integrated circuit processing and can lead to film buckling, warping, blistering, cracking, delamination and void formation.

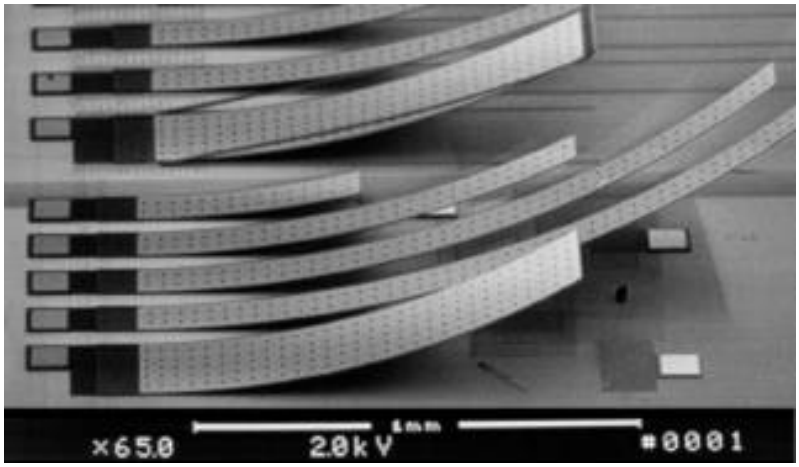

Fig. 5. SEM photography of residual stress cantilevers [23]

There have been a few attempts to develop useful applications of intrinsic stresses in MEMS. Mi *et al* [24] used residual stresses to control the curvature of a micromirror. Layers of polysilicon and silicon dioxide were deposited with no curvature using LPCVD, and when the oxide was etched away, the polysilicon was deformed into a curved structure with a radius of curvature of 6.4mm.

Prinz *et al* [25] used residual stresses to make cylindrical nano structures. A laminate consisting of B doped Si, undoped Si, B doped Si, Ge, and B doped Si was deposited with no curvature. The undoped Si layer was etched away, allowing the upper three layers (b doped Si, Ge, B doped Si) to deform (or “roll up”) into cylinders with radii of curvature from 0.3 to 2 micrometers.

It would be useful if intrinsic stresses could be used to enable a structure to assemble itself during processing, as in self-adjusting microstructures [26]. Such assembly could include both in-plane and out-of-plane motion to lock two parts together, make an electrical contact between separated parts, or close an open region.

Much research has been done to analyze the stress and deformation in thin films due to intrinsic stresses. This work dates to the Stoney formula [27] for the curvature of thin films on a thick substrate. Freund proposed a theory that predicted the response of thin films to mismatch strain produced during the film growth [28]. This was an improvement over the Stoney formula, as it eschewed the assumption that the deposited layer is very thin compared to the thin-film substrate. However, these works did not include the effects of externally applied loads during deposition or etching. An externally applied force will naturally occur during the assembly of two components.

Suppose that two components are to be assembled by deposition or etching of one component. The minimum requirement for assembly is that the part being deposited or etched must do work on the other part. Thus, the part being deposited or etched is subject to an external load in addition to intrinsic stresses.

An analysis has recently been performed to study the mechanics of using residual stress changes due to deposition and etching to self-assemble MEMS [29]. However, this research did not include experimental results. Thus, the present research was undertaken to experimentally verify and analytically expand the results of [29].

II. ANALYTICAL MODELING

The possibility of usefully using residual (or intrinsic) stresses as a means of self-assembling MEMS during material deposition is analytically investigated.

A. Self-Assembly and Residual Stress

Suppose that two parts are to be assembled by deposition onto one part. In order for the two parts to self-assemble, the part being deposited must do work on the other part. Thus, the part being deposited is subject to an external load in addition to residual stress. The part subject to deposition or etching is modeled as an Euler-Bernoulli beam in Fig. 6. The other part is modeled as a linear spring of stiffness K_s. The Euler-Bernoulli beam theory can easily be extended to plate theory.

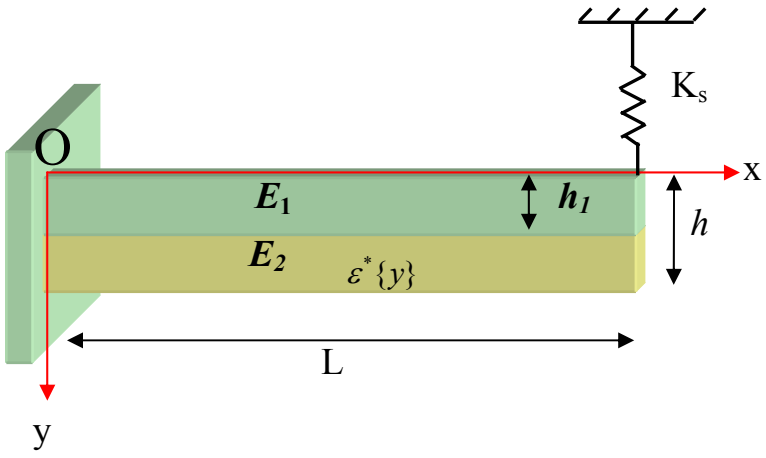

Fig. 6. A cantilever beam connected to a linear spring

The prismatic beam has constant length L, constant width b, and variable thickness h. The substrate is designated as region 1 and has a constant thickness h_1. The deposited material has a variable thickness h_2, and $h = h_1 + h_2$. The spring is attached to the center of the end of the beam $\left[(x, y, z) = (L, 0, b/2)\right]$ when $h = h_1$ in such a way that there is initially no load on the spring or beam. Material is then deposited on the surface $y = h$ $(h \geq h_1)$, which causes the beam to bend and the spring to either compress or stretch, depending on the sign of the mismatch strain in the deposited material.

The goal of the present derivation is to obtain an equation for the beam deflection as a function of h during deposition.

The input to the problem is the increment of thickness, dh, i.e. all changes in the configuration are due only to a changing h. There is no time dependence, so all rates can be replaced by increments. For example, the increment of bending stress $d\sigma$ can be used instead of the time derivative $d\sigma / dt$.

Brackets are used to denote the functional dependence of variables. For example, the bending stress $\sigma\{x, y; h\}$ is a function of x and y as well as the thickness h.

The bending stress and elastic strain $\varepsilon^e\{x, y; h\}$ are related by Hooke's law,

$$\sigma\{x, y; h\} = E\{y\}\varepsilon^e\{x, y; h\} \tag{1}$$

where the Young's modulus is given by

$$E\{y\} = \begin{cases} E_1 & 0 \leq y \leq h_1 \\ E_2 & h_1 < y \leq h \end{cases} \tag{2}$$

The elastic strain is the sum of the total strain $\varepsilon\{x, y; h\}$ and the mismatch strain $\varepsilon^m\{x, y\}$

$$\varepsilon^e\{x,y;h\} = \varepsilon\{x,y;h\} + \varepsilon^m\{x,y\} \tag{3}$$

where the mismatch strain is due to growth processes or lattice mismatch between the deposited material and the deposited surface. The total strain satisfies the compatibility equations, i.e. it can be derived by taking the derivatives of a continuous and single-valued displacement field. In general, neither the elastic strain nor the mismatch strain can be obtained from continuous displacement fields. The total strain obeys the Kirchhoff kinematic assumptions of Euler-Bernoulli beam theory,

$$\varepsilon\{x,y;h\} = -y\kappa\{x;h\} + \varepsilon^r\{x;h\} \tag{4}$$

where $\kappa\{x;h\}$ is the curvature about the z axis and $\varepsilon^r\{x;h\}$ is the strain of the reference layer, $y = 0$. The increment of total strain is given by

$$d\varepsilon\{x,y;h\} = -yd\kappa\{x;h\} + d\varepsilon^r\{x;h\} \tag{5}$$

The reference value $\varepsilon^*\{y\}$ of the mismatch strain is the mismatch strain that results from deposition on a strain-free substrate; for example, a flat substrate that is free of stress. The reference mismatch strain $\varepsilon^*\{y\}$ at a given y does not change in time, so $d\varepsilon^* = 0$.

As material is deposited with non-zero mismatch strain, both the substrate and the deposited layer will bend. Thus, material will be deposited on a strained surface with non-zero curvature. This bending strain $\varepsilon^d\{x,y\}$ on the deposition surface must be subtracted from $\varepsilon^*\{y\}$ to obtain the total mismatch strain,

$$\varepsilon^m\{x,y\} = \varepsilon^*\{y\} - \varepsilon^d\{x,y\} \tag{6}$$

The strain $\varepsilon^d\{x,y\}$ is the value of $\varepsilon\{x,y;h\}$ evaluated on the deposition surface, $y=h$, *at the time that the material was deposited.* Thus, the value of $\varepsilon^d\{x,y\}$ at any point y is equal to $\varepsilon\{x,y;h\}$ evaluated at $h=y$:

$$\varepsilon^d\{x,y\} = -y\kappa\{x;y\} + \varepsilon^r\{x;y\} \tag{7}$$

The most useful form of the mismatch strain is obtained by substituting (7) into (6):

$$\varepsilon^m\{x,y\} = \varepsilon^*\{y\} - \varepsilon^d\{x,y\} = \varepsilon^*\{y\} + y\kappa\{x;y\} - \varepsilon^r\{x;y\} \tag{8}$$

Although the strain $\varepsilon\{x,y;h\}$ at a given point (x,y) changes as $\kappa\{x;h\}$ changes with h, the strain $\varepsilon^d\{x,y\}$ is not a function of h, and $d\varepsilon^d\{x,y\}=0$. The mismatch strain $\varepsilon^m\{x,y\}$ is also constant with respect to h, and $d\varepsilon^m\{x,y\}=0$, and it follows from (3) that

$$d\varepsilon^e\{x,y;h\} = d\varepsilon\{x,y;h\} \tag{9}$$

The elastic strain on the deposition surface is obtained by substituting (8) and (4) into (3) and evaluating at $y=h$ to obtain

$$\varepsilon^e\{x,h;h\} = \varepsilon^*\{y=h\} \tag{10}$$

The equilibrium equations for the moment about the z axis and the horizontal force (x-direction) provide two equations for the two increments $d\kappa\{x;h\}$ and $d\varepsilon^r\{x;h\}$.

The moment equilibrium is given by

$$dM\{x;h\} = b\int_0^h d\sigma\{x,y;h\}ydy + bh\sigma\{x,h;h\}dh \tag{11}$$

where $M\{x;h_1\} = 0$. The stress increment is obtained by substituting (9) into (1):

$$d\sigma\{x,y;h\} = \begin{cases} E_1 d\varepsilon\{x,y;h\} \ , \ 0 \le y \le h_1 \\ E_2 d\varepsilon\{x,y;h\} \ , h_1 < y \le h \end{cases} \tag{12}$$

The stress on the deposition surface is obtained by substituting (10) into (1):

$$\sigma\{x,h;h\} = E_2\varepsilon^e\{x,h;h\} = E_2\varepsilon^*\{h\} \tag{13}$$

Substitution of (12), (13) and (5) into (11) yields the moment increment

$$\begin{aligned} dM\{x;h\} = &\left(-\frac{1}{3}bE_2h^3 - \frac{1}{3}bh_1^3(E_1-E_2)\right)d\kappa\{x;h\} + bE_2\varepsilon^*\{h\}dh \\ &+\left(\frac{1}{2}bE_2h^2 + \frac{1}{2}bh_1^2(E_1-E_2)\right)d\varepsilon^r\{x;h\} \end{aligned} \tag{14}$$

A similar procedure for the horizontal force equilibrium yields

$$\begin{aligned} 0 &= b\int_0^h d\sigma\{x,y;h\}dy + b\sigma\{x,h;h\}dh = b\int_0^h E\{y\}(-yd\kappa\{x;h\} + d\varepsilon^r\{x;h\})dy + bE_2\varepsilon^*\{h\}dh \\ &= \left(-\frac{1}{2}E_2h^2 - \frac{1}{2}(E_1-E_2)h_1^2\right)d\kappa\{x;h\} + E_2\varepsilon^*\{h\}dh + \left(E_2h + (E_1-E_2)h_1\right)d\varepsilon^r\{x;h\} \end{aligned} \tag{15}$$

$d\varepsilon^r\{x;h\}$ can be eliminated from (14) and (15) to obtain the moment increment in terms of the curvature increment and the thickness increment:

$$\frac{dM\{x;h\}}{bE_1} = \frac{1}{12\overline{E}}f\{h\}d\kappa\{x;h\} + \frac{\varepsilon^*\{h\}}{2\overline{E}}g\{h\}dh \tag{16}$$

where $\bar{E} = E_1 / E_2$ and

$$f\{h\} = \left(h + (\bar{E} - 1)h_1\right)^{-1}\left(-h^4 - 4h^3 h_1(\bar{E} - 1) + 6h^2 h_1^2(\bar{E} - 1) - 4hh_1^3(\bar{E} - 1) - h_1^4(\bar{E} - 1)^2\right)$$
$$g\{h\} = \left(h + (\bar{E} - 1)h_1\right)^{-1}\left(h^2 + 2hh_1(\bar{E} - 1) - h_1^2(\bar{E} - 1)\right) \tag{17}$$

Consider the case of deposition of material with the same Young's modulus as the substrate ($\bar{E} = 1$) and zero moment. In this case $dM\{x;h\} = 0$, $g\{h\} = h$, $f\{h\} = -h^3$, and it is possible to derive a closed-form expression for $\kappa\{x;h\}$ and $\varepsilon^m\{x,y\}$. In this case, (16) gives

$$d\kappa\{x;h\} = \frac{6\varepsilon^*\{h\}}{h^2}dh \tag{18}$$

which can be integrated to solve for $\kappa\{x;h\}$:

$$\kappa\{x;h\} = 6\varepsilon^*\{h\}\int_{h_1}^{h} h^{-2}dh + \kappa(x;h_1) \tag{19}$$

where $\kappa\{x;h_1\} = 0$. Performing the integration in (19) results in

$$\kappa\{x;h\} = 6\varepsilon^*\Big|_{y=h}\left(\frac{1}{h_1} - \frac{1}{h}\right) \quad = \quad \frac{6\varepsilon^*\Big|_{y=h}}{h_1}\left(1 - \frac{h_1}{h}\right) \tag{20}$$

The mismatch strain can be obtained by setting (14) equal to zero and using $E_1 = E_2$ to get

$$d\varepsilon^r\{x;h\} = \frac{1}{2}hd\kappa\{x;h\} - \frac{\varepsilon^*\{h\}}{h}dh \tag{21}$$

followed by substituting (18) into (21) to yield

$$d\varepsilon^r\{x;h\} = \frac{3\varepsilon^*\{h\}}{h}dh - \frac{\varepsilon^*\{h\}}{h}dh = \frac{2\varepsilon^*\{h\}}{h}dh \tag{22}$$

Equation (22) can be integrated to solve for $\varepsilon^r\{x;h\}$:

$$\varepsilon^r\{x;h\} = 2\varepsilon^*\{h\}\int_{h_1}^{h} h^{-1}dh + \varepsilon^r\{x;h_1\},$$

where, $\varepsilon^r\{x;h_1\} = 0$. Performing the integration results in

$$\varepsilon^r\{x;h\} = 2\varepsilon^*\{h\}\ln\left(\frac{h}{h_1}\right) \tag{23}$$

and substituting (23) and (20) into (8) yields,

$$\varepsilon^m\{y\} = \begin{cases} 0 & , \quad 0 \le y < h_1 \\ -2\varepsilon^*\{h\}\ln\dfrac{y}{h_1} + \varepsilon^*\{h\}\left(6\dfrac{y}{h_1} - 5\right) & , \quad h_1 \le y \le h \end{cases} \tag{24}$$

Freund [28] derived (24) and pointed out that the mismatch strain differs significantly from its initial value $\varepsilon^*\{y\}$ even for relatively thin deposition layers.

For the case of a spring attached to the beam the increment of moment is non-zero and is given by

$$dM\{x;h\} = dP\{h\}(x - L) \tag{25}$$

where $dP\{h\}$ is the increment of load applied to the beam at $x = L$ by the spring. To derive the beam deflection and work it is necessary to introduce the approximate increment of curvature as

$$d\kappa\{x;h\} = \frac{d^2}{dx^2} dv\{x;h\} \tag{26}$$

where $v\{x;h\}$ is the displacement of the beam in the y direction. Equations (25) and (26) can be substituted into (16) to yield

$$\frac{dP\{h\}}{bE_1}\left(x - L\right) = \frac{f\{h\}}{12\bar{E}} \frac{d^2}{dx^2} dv\{x;h\} + \frac{\varepsilon^*\{h\}}{2\bar{E}} g\{h\} dh \tag{27}$$

Integrating (27) twice with respect to x results in

$$\frac{dP\{h\}}{bE_1}\left(\frac{1}{6}x^3 - \frac{1}{2}Lx^2\right) + c_1 x + c_2 = \frac{f\{h\}}{12\bar{E}} dv\{x;h\} + \frac{\varepsilon^*\{h\}}{4\bar{E}} x^2 g\{h\} dh \tag{28}$$

The boundary conditions $v\{0;h\} = \frac{d}{dx} v\{0;h\} = 0$ yield $0 = c_1 = c_2$, so that (28) becomes

$$\frac{dP\{h\}}{bE_1}\left(\frac{1}{6}x^3 - \frac{1}{2}Lx^2\right) = \frac{f\{h\}}{12\bar{E}} dv\{x;h\} + \frac{\varepsilon^*\{h\}}{4\bar{E}} x^2 g\{h\} dh \tag{29}$$

The load increment on the beam is equal and opposite to the force increment on the spring:

$$dP\{h\} = -K_s dv\{L;h\} \tag{30}$$

Equation (30) can be used in (29) to obtain

$$\frac{dv\{L;h\}}{dh} = \left(\frac{1}{3}\frac{L^3 K_s}{bE_1} - \frac{f\{h\}}{12\bar{E}}\right)^{-1} \frac{\varepsilon^*\{h\} L^2}{4\bar{E}} g\{h\} \tag{31}$$

Equation (31) is an ordinary linear differential equation for the end-deflection $v\{h\}$ as a function of the deposited layer thickness h.

B. Reference Mismatch Strain

In the previous section, a linear ordinary differential is derived for the end deflection of the cantilever beam as a function of the thickness of the deposited layer. However, in order to numerically solve this equation, the reference mismatch strain $\varepsilon^*\{h\}$ must be known. The reference mismatch strain will be determined by interpreting experimental results in terms of the relation between the cantilever curvature and the mismatch strain.

Freund [28] proposed the connections between the cantilever curvature and the mismatch strain for the homogeneous case $(E_1 = E_2)$.

The curvature and the reference strain are given by

$$\kappa\{x;h\} = \frac{I^{(1)}\{h\}J^{(0)}\{h\} - I^{(0)}\{h\}J^{(1)}\{h\}}{\left[I^{(1)}\{h\}\right]^2 - I^{(0)}\{h\}I^{(2)}\{h\}} \tag{32}$$

$$\varepsilon^r\{x;h\} = \frac{I^{(2)}\{h\}J^{(0)}\{h\} - I^{(1)}\{h\}J^{(1)}\{h\}}{\left[I^{(1)}\{h\}\right]^2 - I^{(0)}\{h\}I^{(2)}\{h\}} \tag{33}$$

where,

$$I^{(i)}\{h\} = \int_0^h y^i E\{y\}dy \text{ and } J^{(i)}\{h\} = \int_0^h y^{(i)} E\{y\}\varepsilon^m\{y\}dy \tag{34}$$

When the curvature and the reference strain are expressed in the term of the mismatch strain for the inhomogeneous case,

$$\kappa\{x;h\} = -\frac{6}{h^2}\frac{A\{h\}}{D\{h\}}\int_0^h \varepsilon^m\{y\}dy + \frac{12}{h^3}\frac{B\{h\}}{D\{h\}}\int_0^h y\varepsilon^m\{y\}dy \tag{35}$$

$$\varepsilon^r\{x;h\} = -\frac{4}{h}\frac{C\{h\}}{D\{h\}}\int_0^h \varepsilon^m\{y\}dy + \frac{6}{h^2}\frac{A\{h\}}{D\{h\}}\int_0^h y\varepsilon^m\{y\}dy \tag{36}$$

where,

$$A\{h\} = \frac{h_1^2}{h^2}(E-1)+1,\ B\{h\} = \frac{h_1}{h}(E-1)+1,\ C\{h\} = \frac{h_1^3}{h^3}(E-1)+1,$$

$$D\{h\} = 4\left[\frac{h_1}{h}(E-1)+1\right]\left[\frac{h_1^3}{h^3}(E-1)+1\right] - 3\left[\frac{h_1^2}{h^2}(E-1)+1\right]^2, \text{ and } E = \frac{E_1}{E_2} \tag{37}$$

From (8), the mismatch strain is simply expressed by

$$\varepsilon^m\{y\} = \varepsilon^*\{y\} + y\kappa\{x;y\} - \varepsilon^r\{y\} \tag{38}$$

Substituting (35) and (36) into (38) yields:

$$\varepsilon^*\{y\} = \varepsilon^m\{y\} - \frac{2}{yD\{y\}}\left[2C\{y\}-3A\{y\}\right]\int_0^y \varepsilon^m\{y\}dy - \frac{6}{y^2D\{y\}}\left[2B\{y\}-A\{y\}\right]\int_0^y y\varepsilon^m\{y\}dy \tag{39}$$

Therefore, the reference mismatch strain $\varepsilon^*\{y\}$ can be determined if the mismatch strain $\varepsilon^m\{y\}$ is obtained. This mismatch strain can be obtained through the experiment results.

In the experiment, one would measure the end beam deflection $\nu\{L;h\}$ of cantilever as a function of the deposited layer thickness (h) when no spring is attached to the cantilever. The (approximate) cantilever curvature is expressed by the second derivative of the deflection $\nu\{x;h\}$ with respect to x

$$\kappa\{x;h\} = \frac{d^2}{dx^2}\nu\{x;h\} \tag{40}$$

Where, in this particular case, $\kappa\{x;h\} = \kappa\{h\}$ because κ is not a function of x because there is no spring to load the cantilever and it is assumed that the deposited layer is applied in a manner that is not a function of x.

Integrating (40) twice with respect to x results in

$$\nu\{x;h\} = \frac{1}{2}\kappa\{h\}x^2 + c_1 x + c_2 \tag{41}$$

The boundary conditions $\nu\{0;h\} = \frac{d}{dx}\nu\{0;h\} = 0$ yield $c_1 = c_2 = 0$, so that (41) becomes

$$\nu\{x;h\} = \frac{1}{2}\kappa\{h\}x^2 \tag{42}$$

The end deflection of the cantilever is then

$$\nu(L;h) = \frac{\kappa\{h\}}{2}L^2 \tag{43}$$

Therefore the curvature is expressed by

$$\kappa\{h\} = \frac{2\nu\{L;h\}}{L^2} \tag{44}$$

From (44), for each value of *h*, the curvature can be experimentally obtained from the end beam deflection.

The out-of-plane variation of the mismatch strain $\varepsilon^m\{y\}$ can be approximated as a polynomial function of y

$$\varepsilon^m\{y\} = a + by + cy^2 + dy^3 + ey^4 \cdots \tag{45}$$

and the unknown parameters (a,b,c, . . .) can be determined from from (35).

Finally the reference mismatch strain $\varepsilon^*\{y\}$ can be determined from (39).

III. BACKGROUND FOR EXPERIMENTS

The goal of the experiment is to physically realize the device of Fig. 6 in the chapter titled "Analytical Modeling". The device will consist of two cantilevered beams in contact at their ends, as shown in Fig. 7. One cantilever will be thickened by material deposition on one side, and the second cantilever – the linear spring – will not undergo deposition.

The deposition cantilever also serves as the sensing cantilever because its end deflection will be measured using an Atomic Force Microscope (AFM). A silicon nitride coating is applied to both sides of the cantilevers for electrical isolation. Thin layers of Cr/Au are evaporated on the tip side (bottom) of the deposition cantilever in order to provide electrical conductivity for subsequent electroplating of nickel.

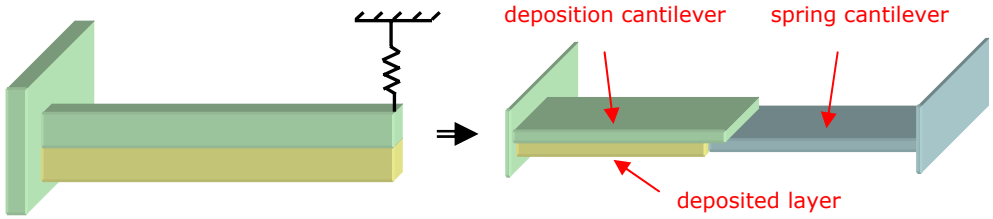

Fig. 7. Linearly placed cantilevers for experiments (a) analytical model (b) experimental model

Material is electroplated onto the deposition cantilever, which produces residual (or intrinsic) stresses that deform the cantilever. This cantilever is attached to a spring cantilever that is not electroplated. The deposition cantilever does work on the spring

cantilever, thereby enabling the two structures to self-assemble. An insoluble nickel electroplating process and an all-sulfate nickel solution are used for the thin film deposition. The plating is done isothermally. The basic figure of this experiment is illustrated in Fig. 8.

The following variables must be measured: the end deflection of deposition cantilever as a function of the deposition thickness, the dimensions of the deposition cantilever, the thickness of the various layers that constitute the deposition cantilever, the elastic stiffness of the deposited material, the stiffness of the spring cantilever.

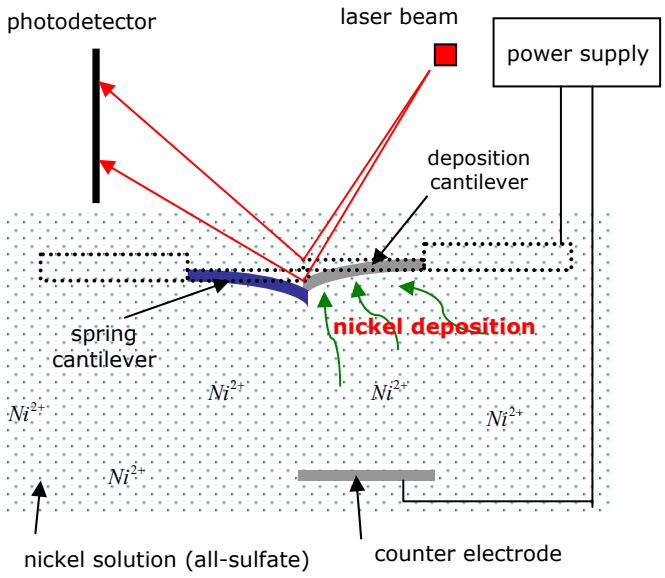

Fig. 8. Basic figure of experiments

A. Deposition Method

Nickel was chosen as the electroplating material because of its economy, convenience, and large intrinsic stress when deposited on gold.

1) General Nickel Electroplating

Electroplated nickel is used extensively for decorative and engineering purposes because the appearance and other properties of electrodeposited nickel can be varied greatly by controlling the composition and the operating parameters of the plating solution [30]-[33]. A typical electroplating cell consists of an anode, cathode, aqueous-metal solution, and a power supply. The sacrificial anode is made of nickel, the cathode is made of another conductive material, and the aqueous-metal solution consists of nickel (Ni^{2+}), hydrogen (H^{+}), and sulfate ions (SO_4^{2-}). When a voltage supply is turned on, the positive ions in the solution are attracted to the negatively biased cathode. The nickel ions that reach the cathode gain electrons from the external circuit and are deposited (or "plated") onto the surface of the cathode forming the electrodeposit. Simultaneously, nickel is electrochemically etched from the nickel anode and dissolved as ions into the solution. The etched nickel can replenish the nickel content in the solution during plating. The shape of anode can be changed. Fig. 9 shows the basic principle of the nickel electroplating process.

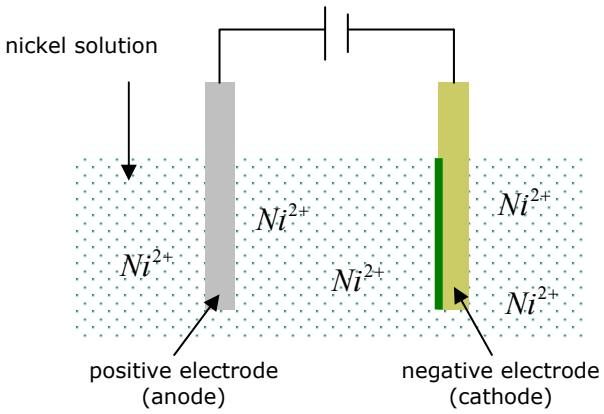

Fig. 9. Basic principle of nickel electroplating process

2) Deposit Thickness of Electroplated Nickel

The thickness of the electroplated layer on the substrate is determined by the time duration of the plating using Faraday's law [31]. Faraday's law states that the amount of electrochemical reaction that occurs at an electrode is proportional to the quantity of electric charge Q passed through an electrochemical cell. The total amount of deposited material m is as followed

$$m = \frac{ItM}{nF} \tag{46}$$

where I is the total current, t is the deposition time, M is molecular weight of the depositing material (58.6934g/mol for nickel), n is the number of electrons involved in the electrochemical reaction (2 for nickel), and F is the Faraday constant. The Faraday constant represents one mole of electrons and its value can be calculated from

$$F = N_A e \tag{47}$$

where N_A is Avogadro's number (6.0255×10^{23} molecules /mol) and e is the charge of a single electron (1.6021×10^{-19} coulombs, C).

$$F = (6.0255\times10^{23})(1.6021\times10^{-19}) = 96,487 C/mol$$

The deposit thickness may be evaluated by considering the volume of the deposit. Since the volume of the deposit V is the product of the plated surface area S, and the thickness d, it follows that $d = V/S$. The volume of the deposit is related to the weight of the deposit m and the density of the deposit material ρ ($8.902 g/cm^3$ for nickel). Thus the deposit thickness is represented by

$$d = \frac{V}{S} = \frac{m}{\rho S} = \frac{1}{\rho S}\frac{ItM}{nF} = \frac{M}{\rho nF}Jt \tag{48}$$

where J is the current density.

The actual thickness of the plated nickel is usually less than calculated thickness due to the cathode current efficiency. In almost all cases, the cathode efficiency may vary from 92 to 97 %. Fig. 10 gives the thickness of deposited film as a function of plating time during nickel electroplating. The thickness of the deposited material is independent of the nickel ion concentration in the solution.

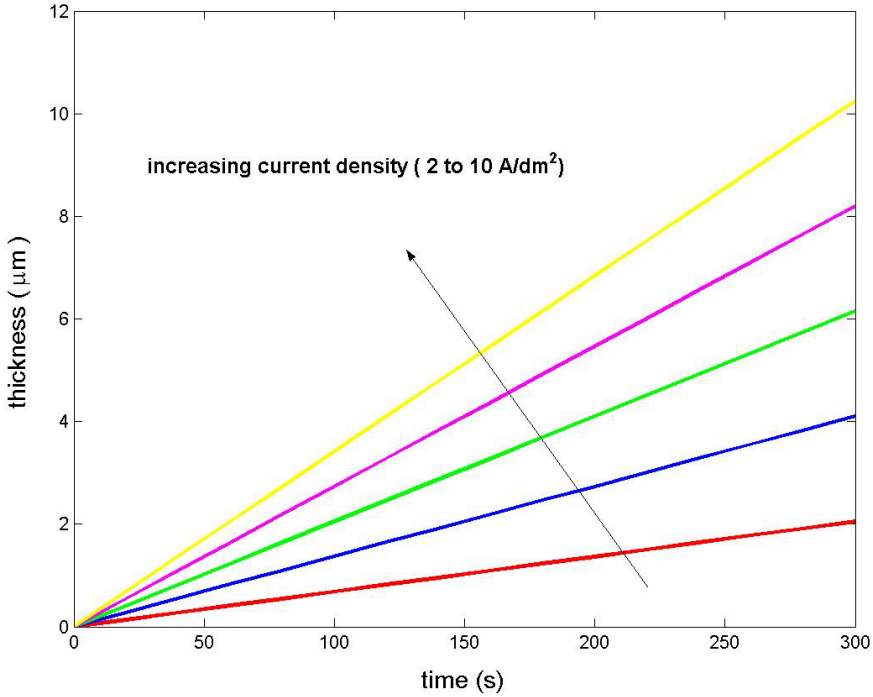

Fig. 10. Deposited film thickness during electroplating as a function of time

3) Nickel Electroplating Solution and Internal Stress

a) Nickel plating solution

The type of anion in the plating solution can have a marked influence on residual stress. In nickel electroplating, the two most popular solutions for engineering applications are Watts nickel and nickel sulfamate [31]. The electrolyte components and the operating conditions of Watts nickel and nickel sulfamate are as shown in Table I, which are used to make the minimum value of the residual stress. The Watts solution is relatively inexpensive and easy to control. The nickel sulfamate plating solutions are

used for the low internal stress but are relatively expensive. Both solutions use the nickel anode.

Other nickel electroplating solutions are also widely used for functional applications. Many of these solutions were developed to meet specific engineering requirements; all are used to a lesser extent than Watts and nickel sulfamate solutions. An all-sulfate solution is used for the experiment herein. This solution has been applied for electrodepositing nickel where the principal or auxiliary anodes are insoluble. Oxygen is evolved at insoluble anodes in all-sulfate solution and as a result, the nickel concentration and pH decrease during plating. The pH is controlled and the nickel ion concentration maintained by adding nickel carbonate $NiCO_3$. Another procedure that has been used in low-pH solutions replenishes the nickel by employing a replenishment tank [32]. The insoluble anodes in all-sulfate solutions may be lead, carbon, graphite or platinum. If a small anode area is required, solid platinum (in the form of wire) may be used.

b) Internal stress

Internal stresses are created within the deposit as a result of the electro-crystallization process and/or the codeposition of impurities such as hydrogen, sulfur, and other elements. Stress in electrodeposited nickel can vary greatly depending on the solution composition and operating conditions [31]. In general, nickel electrodeposited from additive-free Watts solutions exhibits a tensile intrinsic stress that is 125 to 185MPa for the conditions given in Table I. Deposits from sulfamate solutions display

lower tensile intrinsic stress within the range of 0 to 55Mpa, and deposits from all-sulfate solutions have the internal stress of 120MPa. Compressively stressed nickel deposits are obtained from solutions that contain sulfur-containing organic additives similar to the carriers that are added to bright nickel plating solutions. As far as is known, compressively stressed nickel deposits are almost always associated with the codeposition of sulfur.

TABLE I

NICKEL PLATING SOLUTION AND SOME PROPERTIES OF DEPOSITS

	Electrolyte Composition (g/L)		
	Watts Nickel	Nickel Sulfamate	All-Sulfate
Nickel Sulfate, $NiSO_4 \cdot 6H_2O$	225 to 400		225 to 400
Nickel Sulfamate, $Ni(SO_3NH_2)_2$		300 to 450	
Nickel Chloride, $NiCl_2 \cdot 6H_2O$	30 to 60	0 to 30	
Boric Acid, H_3BO_3	30 to 45	30 to 45	30 to 45
	Operating Conditions		
Temperature $^\circ C$	44 to 66	32 to 60	38 to 70
Cathode Current Density, A/dm^2	3 to 11	0.5 to 30	1 to 10
Anodes	Nickel	Nickel	Insoluble
pH	2 to 4.5	3.5 to 4.5	1.5 to 4
	Mechanical Properties		
Internal Stress, MPa	**125 to 185**	**0 to 55**	**120**

4) Operating Condition and Quality Control

Process quality control involves maintaining the concentrations of the main constituents within specified limits, controlling pH, temperature, and current density in order to meet the specified product requirements [31]. Controlling the composition of the

plating bath is one of the most important factors contributing to the quality of electrodeposited nickel. At the outset, the bath must be prepared to the specified composition and adjusted to the proper pH. Thereafter the composition and pH of the solution must be controlled within specified limits.

The basic constituents of nickel electroplating solutions that are regularly controlled are the nickel metal content, the chloride concentration, the boric acid level, and the concentration of all addition agents. The nickel metal concentration is maintained between 60 and 80g liter^{-1} in most commercial applications. It is desirable to have a minimum of 25g liter^{-1} nickel chloride in the solution to promote anode corrosion except when sulfur-activated electrolytic nickel anode materials are used. Boric acid is the most commonly used buffering agent for nickel plating baths. Boric acid is effective in stabilizing the pH in the cathode film within the ranges normally required for best plating performance.

Under normal operating conditions of nickel electroplating with a nickel anode, the pH of the nickel solution will slowly increase as plating process due to the difference between cathode and anode efficiencies. Generally, cathode efficiencies may vary from 92 to 97 percent, whereas anode efficiency is always 100 percent. A decrease in pH accompanied by a decrease in nickel ion concentration indicates that the process is not functioning properly. Sulfuric acid in Watts solutions and nickel carbonate $NiCO_3$ in all-sulfate solutions are added for pH adjustment. The residual stress can reach minimum value within the prescribed limits of pH (2 to 4.5 of pH from Watts solution, at 5 A/dm^2 and 55 $^{\circ}C$). Beyond the limits of pH, the residual stress increases rapidly.

The operating temperature has a significant effect on the properties of the deposits and should be maintained within specified limits ($\pm 2^{\circ}C$) of the recommended value. Increasing the plating solution temperature can reduce the residual stress in a limited range of the temperature. The residual stress may stay in low value within the limits of the temperature (44 to 66 $^{\circ}C$ from Watts solution, at pH 3.0 and 5 A/dm^2) Beyond the limits of the temperature, the residual stress increases.

The nickel plating process should be controlled by estimating the surface area of the parts to be electroplated, and the ampere-hours required to deposit a specified thickness of nickel at a specified current density. The practice of operating the process at a fixed voltage is not recommended. Controlling cathode current density is important for meeting minimum coating thickness requirements, and for producing deposits with consistent and predictable properties. Since current density determines the rate of deposition, it must be as uniform as possible to achieve uniformly thick nickel deposits. The current density of cathode also increases the residual stress. Within the limited range of current density (3 to 11 A/dm^2 from Watts solution, at pH 3.0 and 55 $^{\circ}C$), the residual stress remain in minimum value. Beyond the limits of the current density, the residual stress increases.

B. Measurement of the Cantilever Deflection

The physical basis of AFM sensors is to measure the mechanical response (i.e., bending) of the AFM cantilever due to various local environmental changes that give rise to changes in the forces acting on the cantilever. Much research on the use of AFM

sensors is performed in air, vacuum, or liquid environments has been done [34]-[37]. This has applicability to self-assembled or electrochemically deposited thin films.

In this experiment, the deflection of AFM cantilevers and the deposited film thickness are in situ measured as a function of time in the same experiment conditions.

The deflection of self-assembled cantilevers during electroplating can be measured using the standard optical method. A laser beam bounces off the back of the sensing cantilever onto a position-sensitive photodetector (PSPD). As the cantilever bends, the position of the laser on the detector shifts. However, the position shift on photodetector can not be directly translated to the cantilever deflection. Generally, the cantilever deflection is expressed as the term of the photodetector output voltage signal. When the cantilever is bended, the output voltage signal of the photodetector is also changed. To convert the photodetector output signal difference into a distance moved by the end of the cantilever, the signal sensitivity is done.

The signal sensitivity is the sensitivity measurement of the photodetector's voltage output signal to the cantilever deflection by using the force calibration plot. First, the cantilever is loaded in the cantilever holder and the bottom surface controlled by the piezo is being moved up and down to the cantilever until the cantilever touches the surface. Due to the force between the surface and the cantilever, the cantilever is bended. The deflection of the cantilever is monitored and plotted in a graph of deflection verses piezo movement. An example of such a graph is shown in Fig. 11. On the vertical axis the output of the photodiode is plotted and the horizontal axis gives the position of the

piezo. The curve I-I-III gives the interaction on approach and the other corresponds to the interaction upon retraction.

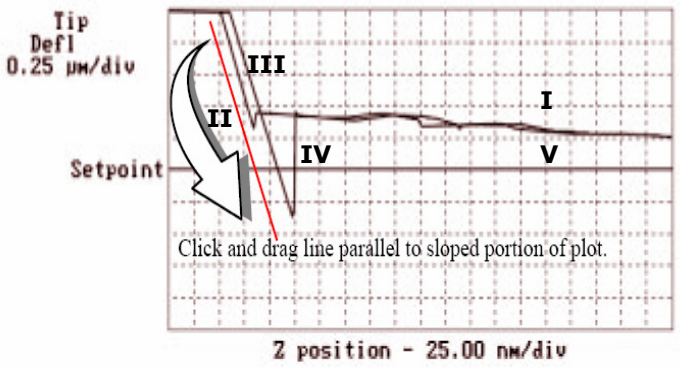

(a)

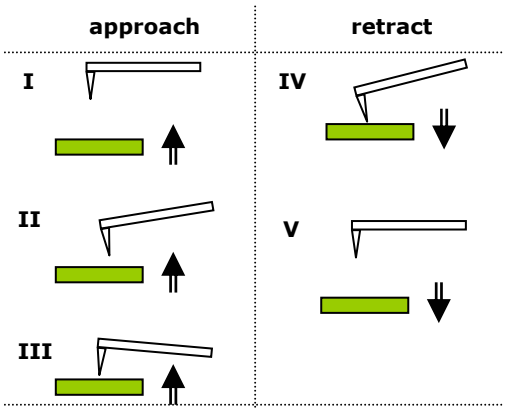

(b)

Fig. 11. Force calibration plot for measuring the deflection of cantilever (a) and its explanation (b)

The photodetector's sensitivity, which is the cantilever deflection per unit output voltage signal of detector, is simply obtained by using the mouse to draw a line parallel to the part of the plot where the tip is on the surface. Finally, the deflection of the

cantilever during plating can be achieved by multiplying the detector's voltage output signal difference to the photodetector sensitivity.

C. Measurement of the Mismatch Strain

X-ray diffraction can be used to measure residual (herein called "mismatch") strains, which can then be used to calculate the residual stress. Unfortunately, classical X-ray stress analysis has a resolution of only about 20 to 35 MPa [38], which corresponds to a strain of about 0.0001 in a structural metal. More recently, X-ray diffraction was used to measure the residual stresses in nickel (0.1 to 1.0 mm thick) that was electroplated onto copper substrates. The resolution of the x-ray technique was estimated to be 10 MPa [39].

In the present experiment we use the measured beam end deflection to calculate the curvature and then the residual strain, for two reasons: 1) we must measure the beam end deflection anyway to validate the analytical model; and 2) the residual strain resolution using the beam end deflection can be calculated from (4) and (44) to be 0.00000013, for h = 7 micrometers, L = 230 micrometers, and an end deflection resolution of 1.0 nanometers. Note that this strain resolution is one thousand times better than the resolution using X-ray diffraction.

D. Measurement of the Spring Constant

The ability to experimentally determine the spring constant of atomic force microscope cantilevers is of fundamental importance in many applications of AFM. To date many methods have been devised for this purpose, including the methods that

monitor the static deflection of the cantilevers and those that utilize the cantilevers' dynamic deflection properties [40]-[45]. However, those methods are performed in vacuum and require the mass of the cantilever which is typically obtained from the density, thickness, and plan view dimensions of the cantilever. Recently, Sader *et al.* proposed a simple, practical, and accurate method to determine the spring constant of cantilever which is working in fluid [46]. The spring constant from Sadar's method is determined from its unloaded resonant frequency. The mass of the cantilever is also required and this is typically obtained from the density, thickness, and plan view dimensions of the cantilever.

For the case of a rectangular cantilever, the spring constant is given by

$$k = m^* \rho_c bhL\omega_{vac}^2 \tag{49}$$

where, ω_{vac} is the fundamental radial resonant frequency of the cantilever in vacuum, $b, h,$ and L are the thickness, width, and length of the cantilever, respectively, ρ_c is the mass density of the cantilever, and m^* is the normalized effective mass which takes the value $m^* = 0.2427m$ for $L/b > 5$ [46]. The vacuum resonant frequency ω_{vac} is related to the resonant frequency in fluid ω_f by

$$\omega_{vac} = \omega_f \left(1 + \frac{\pi \rho_f b}{4 \rho_c h} \Gamma_r(\omega_f) \right)^{1/2} \tag{50}$$

whereas the areal mass density $\rho_c h$ is given by

$$\rho_c h = \frac{\pi \rho_f b}{4}\left[Q_f \Gamma_i(\omega_f) - \Gamma_r(\omega_f) \right] \tag{51}$$

where ρ_f is the mass density of the fluid, Q_f is the quality factor in fluid, Γ_r and Γ_i are, respectively, the real and imaginary components of the hydrodynamic function Γ, which is explained in detail below and plotted in Fig.12. Substituting (50) and (51) into (49) we obtain the spring constant of cantilever which is immersed and operating in

$$k = 0.1906 \rho_f b^2 L Q_f \Gamma_i(\omega_f) {\omega_f}^2 \tag{52}$$

The plan view dimensions of the cantilever are easily obtained if "calibrated cantilevers" are used, which have a highly uniform rectangular geometry and the dimensions are specified to within a high tolerance by the manufacturer. General "practical cantilevers" do not have the highly uniform rectangular geometry but the width b and the length L of the cantilever can be easily measured using an optical technique. The densities ρ and viscosities η of the fluids can be obtained from published data [47].

The analytical expressions for the hydrodynamic function $\Gamma(\omega)$ of beams that are circular and rectangular in cross section are well known and plotted [48], [49]. For the case of the cantilever with the circular cross section, the exact analytical result for $\Gamma(\omega)$ is well known [50] and is given by

$$\Gamma_{circ}(\omega) = 1 + \frac{4iK_1(-i\sqrt{i\,\mathrm{Re}})}{\sqrt{i\,\mathrm{Re}}K_0(-i\sqrt{i\,\mathrm{Re}})} \text{ and } \mathrm{Re} = \frac{\rho\omega b^2}{4\eta} \tag{53}$$

where Re is the Reynolds number, ρ and η are the density and the viscosity of the fluid, respectively. The functions K_0 and K_1 are modified Bessel functions of the third kind [51].

The hydrodynamic function for the rectangular cantilever can be expressed as

$$\Gamma_{rect}(\omega) = \Omega(\omega)\Gamma_{circ}(\omega) \tag{54}$$

where $\Omega(\omega)$ is the correction function and expressed as a rational function in $\log_{10}\mathrm{Re}$. The real and imaginary parts of $\Omega(\omega)$ is

$$\begin{aligned}
\Omega_r(\omega) = {} & (0.91323 - 0.48274\tau + 0.46842\tau^2 - 0.12866\tau^3 + 0.044055\tau^4 - 0.0035117\tau^5 \\
& + 0.00069085\tau^6) \times (1 - 0.56964\tau + 0.48690\tau^2 - 0.13444\tau^3 + 0.045155\tau^4 \\
& - 0.0035862\tau^5 + 0.00069085\tau^6)^{-1} \\
\Omega_i(\omega) = {} & (-0.024134 - 0.029256\tau + 0.016294\tau^2 - 0.00010961\tau^3 + 0.000064577\tau^4 \\
& - 0.000044510\tau^5) \times (1 - 0.59702\tau + 0.55182\tau^2 - 0.18357\tau^3 + 0.079156\tau^4 \\
& - 0.014369\tau^5 + 0.0028361\tau^6)^{-1}
\end{aligned} \tag{55}$$

$$\tau = \log_{10}\mathrm{Re} \text{ and } \Omega(\omega) = \Omega_r(\omega) + i\Omega_i(\omega) \tag{56}$$

The real and imaginary components of the hydrodynamic function $\Gamma(\omega)$ as a function of the Reynolds number $\mathrm{Re} = \rho\omega b^2 / 4\eta$ is re-plotted in Fig. 12. We note that the hydrodynamic function only depends on the Reynolds number and is independent of the cantilever thickness and density.

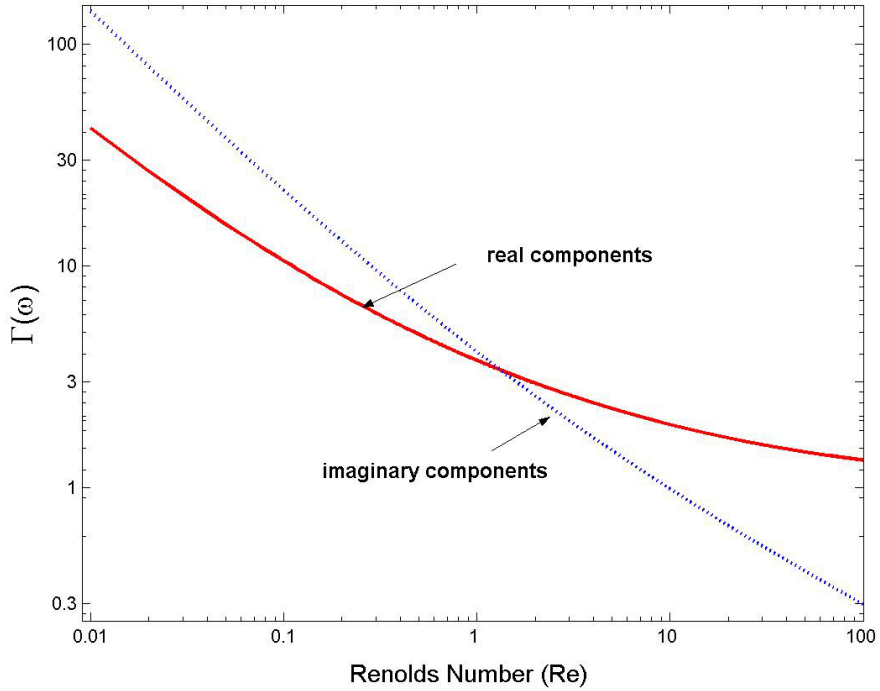

Fig. 12. Plot of the real and imaginary components of hydrodynamic function as a function of the Reynolds number

The quality factor Q_f and the resonant frequency ω_f of the cantilever in fluid can be measured by experiment [49]. First they can be obtained by measuring the thermal noise spectra of cantilevers. The cantilever signal is measured using the optical deflection system of the Nanoscope III Multimode AFM, with the detection laser beam focused on the end of the cantilever. The thermal noise spectra is measured using a National Instruments data acquisition (DAQ) card, carrying out a digital fast Fourier transform of the signal using Labview software which is also available from National Instruments. The fundamental mode resonance peaks of the measured spectra are fitted to the response of a simple harmonic oscillator (SHO), using a nonlinear least squares

fitting procedure. A white noise floor is included in the fitting procedure to ensure accurate fits to the noise spectra

$$A_{SHO}(\omega) = \left[A_{white}^2 + \frac{{A_0}^2 {\omega_0}^4}{(\omega^2 - {\omega_0}^2)^2 + \frac{\omega^2 {\omega_0}^2}{Q^2}} \right]^{\frac{1}{2}} \tag{57}$$

where $A_{SHO}(\omega)$ is the amplitude response function, A_{white} is the amplitude of the white noise floor, A_0 is the zero frequency in the absence of dissipative effects, and Q is the quality factor. These four parameters are obtained by performing a nonlinear least squares fit to data near the peak of each resonance. This method requires other equipment and software such as a DAQ card, Labview and Mathematica.

The other method to obtain the quality factor and the resonant frequency is using the Tapping Mode of AFM [49]. In this method, the cantilevers are vibrating at their base using the Tapping Mode cantilever tune software in the Nanoscope III AFM from Digital Instruments. The frequency response of the cantilever can be measured by driving the cantilever at a range of frequencies in the neighborhood of its fundamental mode resonance peak. The resonant frequency is the first peak of the cantilever tune and it is measured by oscillating the cantilever die, and finding the frequency that produces the maximum response. The quality factor represents the amount of damping in the mechanical oscillator and it is measured by frequency sweeping an excitation to the cantilever and normalizing the width of the peak to its frequency. This approach using

Tapping Mode of AFM gives the same results of Q_f and ω_f as that obtained from the thermal noise spectrum.

These two approaches allow easy and accurate determination of the quality factor and the resonant frequent comparing to the experimental results from Sadar's paper [49].

Now all parameters are obtained and the spring constant of cantilever in fluid can be determined by experiments.

E. Measurement of Deposited Layer Thickness

The thickness of the film to be deposited on the sensing cantilever is measured by using a stylus measurement method, which required the presence of a groove or a step between the substrate and the film surface such that the stylus is vertically displaced as it traverses the sample [52], [53]. The gold layer is initially coated on the portion of the sensing cantilever. Therefore the nickel is deposited only on the portion of the sensing cantilever during electroplating and makes a step between the plated and unplated layers.

DEKTAK^3, a commercial surface profile measuring system, provides an electro-mechanical method for measuring film thickness; a diamond stylus with the radius of $12.5\mu m$ is scanned across the cantilever surface and any vertical movement of the stylus being detected by an inductance transducer [54], as shown in Fig. 13. The resultant electrical signal is amplified and the output fed to a recorder. The vertical movement of the stylus is in the range of $10nm$ to $65.5\mu m$ and its vertical resolution is $1nm$. The basic principle of measuring the step height between the plated and unplated layers of the cantilever surface is shown in Fig. 14.

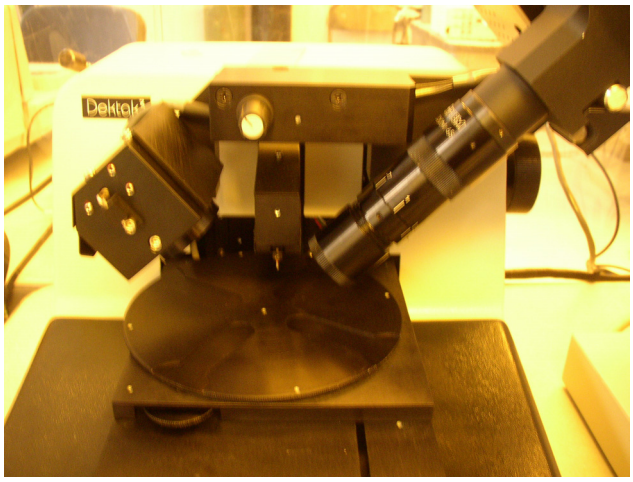

Fig. 13. DEKTAK[3], a commercial surface profile measuring system for measuring the plating layer thickness

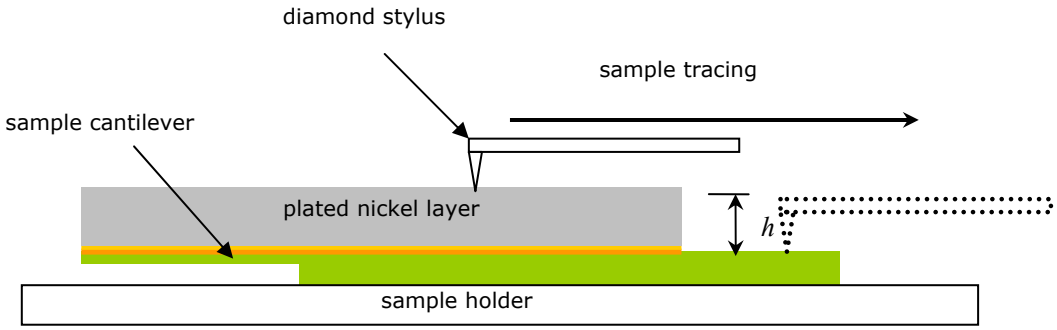

Fig. 14. Basic figure of measuring the plating layer thickness

As its highest sensitivity, the performance of DEKTAK[3] is easily affected by the stage level and it is very important to position the sample surface to within ±0.01° of level.

F. Mechanical Properties of the Deposited Material

The mechanical properties of an electroplated material are highly dependent upon the composition of the plating bath along with the current and temperature, and need to be calibrated by experiment [55]. Young's modulus of the electroplated nickel is obtained from the spring constant of the composite cantilever beam using the laminar beam theory [56].

The spring constant of the rectangular cantilever is expressed as

$$k = \frac{3EI}{L^3} \tag{58}$$

where E is Young's modulus, I is the moment of inertia and L is the length of the cantilever beam.

In order to get the spring constant of the composite cantilever beam, it is necessary to introduce the notation of neutral axis, denoted z_N. The neutral axis defines the plane in the cantilever where the resulting stress is zero when bending the cantilever. The position of the neutral axis in the structure is defined as

$$z_N = \frac{\sum_i E_i z_i h_i}{\sum_i E_i h_i} \tag{59}$$

where E_i is the young's modulus of the i^{th} layer, z_i is the distance from the bottom of the structure to the middle of the i^{th} layer and h_i is the thickness of the i^{th} layer. The moment of inertia I_i for the i^{th} layer is defined as

$$I_i = \int_A y^2 dA = \int_{z_i - z_N - h_i/2}^{z_i - z_N + h_i/2} y^2 b dy = \frac{b t_i^{\,3}}{12} + b h_i (z_i - z_N)^2 \tag{60}$$

where A is the cross sectional area, y is the distance to the neutral axis and $z_i - z_N$ is the distance between the center of the i^{th} layer and the neutral axis. The effective stiffness EI for a composite cantilever can then be expressed by summing the product of Young's modulus and the moment of inertia for each layer

$$EI = b \sum_i E_i \left(\frac{h_i^{\,3}}{12} + h_i (z_i - z_n)^2 \right) \tag{61}$$

Therefore, the spring constant of the composite cantilever beam is

$$k = \frac{3EI}{L^3} = \frac{3b}{L^3} \sum_i E_i \left(\frac{h_i^{\,3}}{12} + h_i (z_i - z_n)^2 \right) \tag{62}$$

The spring constant of the composite cantilever with two layers

$$z_N = \frac{\sum_i E_i z_i h_i}{\sum_i E_i h_i} = \frac{E_f \frac{h_f}{2} h_f + E_c (h_f + \frac{h_c}{2}) h_c}{E_f h_f + E_c h_c} \tag{63}$$

$$k = \frac{3b}{L^3} \sum_i E_i \left(\frac{h_i^{\,3}}{12} + h_i (z_i - z_n)^2 \right) = \frac{3b}{L^3} \left\{ E_f \left[\frac{h_f^{\,3}}{12} + h_f (z_f - z_n)^2 \right] + E_c \left[\frac{h_c^{\,3}}{12} + h_c (z_c - z_n)^2 \right] \right\} \tag{64}$$

The spring constant, the deposited film thickness and in-plane geometry data are measured by the experiments and, therefore, the elastic modulus of the deposited material is determined.

G. Uncertainty Analysis of Experiment

The true value of a measurand is the real world value. Because our instruments do not perfectly measure this real world value, the true value of the measurand is never known. The indicated value of the measurand is the value given by the instrument. The error is the difference between the indicated value and the true value. Because the true value is never known, the error is also never known. Therefore, we define a term called the uncertainty, which is a range in which we believe the error to lie.

In the previous section, we discussed how the spring constant of the cantilever and the elastic modulus of the deposited material are determined through the experiment. However, these values have their own errors because of the experimental uncertainty [57]-[60]. The experimental uncertainty is divided into two categories: the experimental error associated with repeated measurements, and the uncertainty due to not knowing the exact values for the dimensions and material properties. Generally, the cantilever dimensions should be considered to be uncertain because these parameters are affected by manufacturing variability. The parameters which depend on the change of the experimental environment, such as air density and viscosity are also considered to be uncertain.

In this section, we study the sensitivity analysis of the individual parameters and how variation of the individual parameters affects other parameters such as the spring constant and the elastic modulus of the deposited material. The study also considers the possibility that the alignment of the AFM cantilevers is not perfectly centered. For the purpose of simplicity, the errors in the spring constant and the elastic modulus of the

deposited material is estimated by adding up all the errors involved in the measurement of cantilever dimensions, resonant frequency, etc., according to the Sadar's equation and the Euler-Bernoulli beam theory.

1) Propagation of Uncertainty

Given the uncertainty ($\triangle x_i$) in the measurands (x_i), we must calculate the uncertainty in a function (f) of those measurands, i.e. we must calculate how the uncertainty propagates. Generally, the uncertainty of the measurement is estimated analytically using uncertainty propagation methods [57]. This method is a special application of Taylor's series and can be expressed as

$$f\left[(x_1+\Delta x_1),(x_2+\Delta x_2),\cdots,(x_n+\Delta x_n)\right]=f(x_1,x_2,\cdots,x_n)+\Delta x_1\frac{\partial f}{\partial x_1}+\Delta x_2\frac{\partial f}{\partial x_2}+\cdots+\Delta x_n\frac{\partial f}{\partial x_n}+\text{ higher-order terms} \tag{65}$$

where the x_n's are variables and the Δx_n's are determined or assumed incremental variations in the respective x_n's. The higher-order terms are neglected.

This equation can be rewritten, changing the Δx_n's to u_n's merely to represent uncertainties better:

$$f\left[(|x_1|+|u_1|),(|x_2|+|u_2|),\cdots,(|x_n|+|u_n|)\right]-f\left[|x_1|,|x_2|,\cdots,|x_n|\right]=u_f=\left|u_{x_1}\frac{\partial f}{\partial x_1}\right|+\left|u_{x_2}\frac{\partial f}{\partial x_2}\right|+\cdots+\left|u_{x_n}\frac{\partial f}{\partial x_n}\right| \tag{66}$$

Equation (66) evaluates the maximum uncertainty of the function. The most probable uncertainty corresponds to the Pythagorean summation of the discrete uncertainties, or

$$u_f = \sqrt{\left(u_{x_1}\frac{\partial f}{\partial x_1}\right)^2 + \left(u_{x_2}\frac{\partial f}{\partial x_2}\right)^2 + \cdots + \left(u_{x_n}\frac{\partial f}{\partial x_n}\right)^2} \tag{67}$$

where x_i is the nominal value of variables, u_i is the discrete uncertainties, and u_f is the overall uncertainty, respectively.

2) Uncertainty of Spring Constant

The spring constant of the AFM cantilever using Sadar's equation is expressed in (52) and written again

$$k = 0.1906\rho_f b^2 L Q_f \Gamma_i(\omega_f)\omega_f{}^2$$

The overall uncertainty (u_k) and the relative uncertainty of the spring constant are

$$u_k = \frac{\partial k}{\partial \rho_f}u_{\rho_f} + \frac{\partial k}{\partial b}u_b + \frac{\partial k}{\partial L}u_L + \frac{\partial k}{\partial Q_f}u_{Q_f} + \frac{\partial k}{\partial \Gamma_f}u_{\Gamma_f} + \frac{\partial k}{\partial \omega_f}u_{\omega_f} \tag{68}$$

$$\frac{u_k}{k} = \left[\left(\frac{u_{\rho_f}}{\rho_f}\right)^2 + \left(\frac{2u_b}{b}\right)^2 + \left(\frac{u_L}{L}\right)^2 + \left(\frac{u_{Q_f}}{Q_f}\right)^2 + \left(\frac{u_{\Gamma_i}}{\Gamma_i}\right)^2 + \left(\frac{2u_{\omega_f}}{\omega_f}\right)^2\right]^{1/2} \tag{69}$$

a) Uncertainty of air density

The density of air depends on the temperature and is ruled by

$$\rho_f = \rho_{f_0} T_0 / T \tag{70}$$

where ρ_{f_0} is the air density at $0^\circ C\,(1.2929 kg/m^3)$ [43], and T is the temperature. The experiment is working at the room temperature $(25^\circ C)$ and its air density is $1.1845 kg/m^3$. The uncertainty of temperature come from the temperature change

during experiment and error of temperature measurement (assume $\pm 1^{\circ}$). Considering the uncertainty of the temperature, the uncertainty of the density (u_{ρ_f}) is $0.004 kg/m^3$. Therefore, the relative uncertainty of the air density is

$$\frac{u_{\rho_f}}{\rho_f} = \frac{0.004}{1.1845} = 0.0034 \Rightarrow 0.34\%$$

b) Uncertainty of resonant frequency

The nominal resonant frequency of the AFM cantilever used in experiment is $170 KHz$ and the resolution of AFM for measuring the resonant frequency is $0.01 KHz$.

$$\frac{u_{\omega_f}}{\omega_f} = \frac{0.01}{170} = 0.000059 \Rightarrow 0.0059\%$$

The current AFM cantilever used in the experiment has the probe tip at the end of cantilever and the effect of the probe tip in the uncertainty of the resonant frequency of AFM cantilever should be considered. The SEM image of the probe tip of cantilever is shown in Fig. 15.

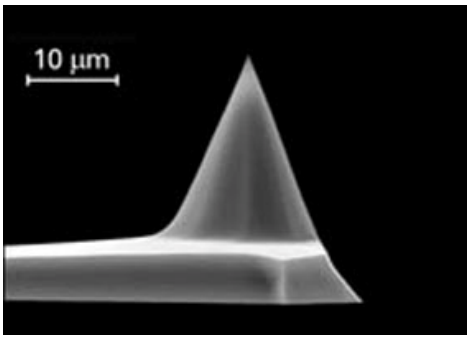

Fig. 15. SEM image of the probe tip of AFM cantilever

ω_1 and ω_2 are the resonant frequency of the tipless cantilever and cantilever with tip, respectively, and expressed by

$$\omega_1 = \sqrt{\frac{k}{m^*}} = \sqrt{\frac{k}{0.2427m}} \text{ and } \omega_2 = \sqrt{\frac{k}{m^* + m_{tip}}} \tag{71}$$

where k is the spring constant of the cantilever, m and m^* are the mass of cantilever and the probe tip.

A typical probe tip height is $10 \sim 15\mu m$ with a radius of curvature of less than $10nm$ at the probe tip end. The macroscopic half-cone angles are $20 \sim 25^\circ$ viewed along the cantilever axis and $25 \sim 30^\circ$ seen from the side, and virtually zero when viewed from the probe tip end.

The relatively uncertainty of the resonant frequency due to the tip is

$$\frac{\omega_1 - \omega_2}{\omega_1} = \frac{\sqrt{\frac{k}{m^*}} - \sqrt{\frac{k}{m^* + m_{tip}}}}{\sqrt{\frac{k}{m^*}}} = (1 - \frac{\sqrt{m^*}}{\sqrt{m^* + m_{tip}}}) = 0.75\% \tag{72}$$

Therefore, considering all perturbations and errors for measuring the resonant frequency, the relative uncertainty of the resonant frequency is less than 1%.

c) Uncertainty of quality factor

The quality factor shows how fast a system decay or damping occurs and defined as

$$Q_f = 2\pi \frac{W}{\Delta W} \tag{73}$$

where W is the energy stored in a system and ΔW is the energy dissipated per cycle. The quality factor is also expressed in the terms of the resonant frequency of the system, as shown in Fig. 16.

$$Q_f = 2\pi \frac{\omega_{\max}}{\Delta\omega} \tag{74}$$

where $\omega_{\max}$ is the resonant frequency where its amplitude is maximum and $\Delta\omega$ is the bandwidth of the response which is defined as $\Delta\omega = \omega_1 - \omega_2$

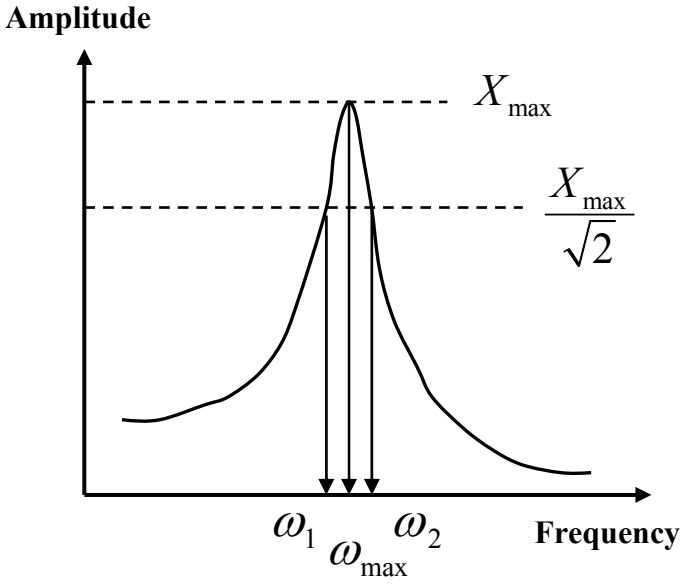

Fig. 16. Plot of the amplitude as a function of the frequency

The uncertainty (u_{Q_f}) and the relatively uncertainty of the quality factor are

$$u_{Q_f} = \frac{\partial Q}{\partial \omega} u_w + \frac{\partial Q}{\partial \Delta\omega} u_{\Delta\omega} = \frac{2\pi}{\Delta\omega} u_w + 2\pi\omega\left(-\frac{1}{\Delta\omega^2}\right) u_{\Delta\omega} \tag{75}$$

$$\frac{u_{Q_f}}{Q_f} = \left|\frac{u_{\omega_f}}{\omega}\right| + \left|-\frac{u_{\Delta\omega}}{\Delta\omega}\right| \Rightarrow \sqrt{\left(\frac{u_{\omega_f}}{\omega}\right)^2 + \left(-\frac{u_{\Delta\omega}}{\Delta\omega}\right)^2} \tag{76}$$

The bandwidth of the response $(\Delta\omega)$ is $1.389kHz$ when the nominal resonant frequency of the cantilever is $170KHz$ from the experiment.

$$u_{\Delta\omega} = \left|\frac{\partial\Delta\omega}{\partial\omega_2}u_{\omega_2}\right| + \left|\frac{\partial\Delta\omega}{\partial\omega_1}u_{\omega_1}\right| = \left|u_{\omega_2}\right| + \left|-u_{\omega_1}\right| \tag{77}$$

The uncertainty of ω_1 or ω_2 is equal to the AFM resolution for measuring the resonant frequency (u_{ω_f}), that is, $u_{\omega_1} = u_{\omega_2} = 0.01KHz$. The relative uncertainty of the bandwidth of the response is

$$\frac{u_{\Delta\omega}}{\Delta\omega} = \left|\frac{u_{\omega_2}}{\Delta\omega}\right| + \left|-\frac{u_{\omega_1}}{\Delta\omega}\right| = \sqrt{2\left(\frac{u_{\omega_1}}{\Delta\omega}\right)^2} = \sqrt{2\times\left(\frac{0.01}{1.389}\right)^2} = 0.01018$$

Therefore, total relative uncertainty of the quality factor is

$$\frac{u_{Q_f}}{Q_f} = \sqrt{0.01^2 + 0.01018^2} = 0.01427 \Rightarrow 1.43\%$$

d) Uncertainty of cantilever dimensions

The dimensions of cantilever used in experiment are provided from the manufacturer but its dimensions have too much uncertainty ($b = 40 \pm 3\mu m$ and $L = 230 \pm 5\mu m$). There are a number of different approaches that can be used to measure the film thickness or the dimensions of various structural features of a MEMS device, including use of scanning electron microscopy, mechanical or optical

profilometry, and optical inteferometry. The scanning electron microscopy (SEM) is used for measuring the cantilever dimensions in this experiment. SEM has its own intrinsic limitation on the accuracy that can be achieved, depending partly on the quality of its calibration. In addition, mechanical elements created by the sequential steps of deposition, lithography and etching typical in MEMS fabrication are rarely ideal structures with perfectly straight edges and 90° angles at all corners. As a result, it is typical to state the dimensions of a structure with an uncertainty of between $0.05 \sim 0.1 \mu m$ [60]. Therefore, the relative uncertainty of the width and length of the cantilever are

$$\frac{u_b}{b} = \frac{0.05}{40} = 0.00125 \Rightarrow 0.125\%$$
$$\frac{u_L}{L} = \frac{0.05}{230} = 0.000217 \Rightarrow 0.0217\%$$

e) Uncertainty of hydrodynamic function

The hydrodynamic function (Γ) is dimensionless and depends on the crosses section of the cantilever and Reynolds number (Re) of the system. Therefore, it is better to obtain the uncertainty of the Reynolds number in order to get the uncertainty of the hydrodynamic function. The Reynolds number of the system is defined by

$$\mathrm{Re} = \frac{\rho_f \omega_f b^2}{4\eta} \tag{78}$$

where η is the viscosity of air. The viscosity of air depends on the temperature and is ruled by

$$\eta_f = \eta_{f_0} T / T_0 \tag{79}$$

where η_{f_0} is the air viscosity at $0^\circ C\,(1.71\times10^{-5} kg/ms)$, T is the temperature.

The air density at experiment temperature $(25^\circ C)$ is $1.866\times10^{-5} kg/ms$. The uncertainty of temperature come from the temperature change during experiment and error of temperature measurement (assume $\pm1^\circ$). Considering the uncertainty of the temperature, the uncertainty of the viscosity is $0.006 kg/ms$. Therefore, the relative uncertainty of the air viscosity is

$$\frac{u_\eta}{\eta} = \frac{0.006}{1.866} = 0.0032 \;\Rightarrow\; 0.32\%$$

Therefore, the relative uncertainty of the Reynolds number is

$$\frac{u_{\mathrm{Re}}}{\mathrm{Re}} = \left[\left(\frac{u_{\rho_f}}{\rho_f}\right)^2 + \left(\frac{u_{\omega_f}}{\omega_f}\right)^2 + \left(\frac{2u_b}{b}\right)^2 + \left(\frac{u_\eta}{\eta}\right)^2\right]^{1/2} = 1.13\%$$

The Reynolds number is 27.1055 when all other factors are nominal value and its uncertainty is $u_{\mathrm{Re}} = 0.3063$. Therefore the ranges of the Reynolds number considering its uncertainty is

$$26.7992 \le \mathrm{Re} \le 27.4118$$

The hydrodynamic function Γ_i is 0.5719 at $\mathrm{Re} = 27.1055$ and the ranges of the hydrodynamic function with the uncertainty of the Reynolds number is

$$0.5686 \le \Gamma_i \le 0.5753$$

Therefore, the relative uncertainty of the hydrodynamic function is

$$\frac{u_{\Gamma_i}}{\Gamma_i} = \frac{0.0034}{0.5719} = 0.0059 \Rightarrow 0.59\%$$

Therefore, the total uncertainty of the spring constant (u_k) is

$$\begin{aligned}\frac{u_k}{k} &= \left[\left(\frac{u_{\rho_f}}{\rho_f}\right)^2 + \left(\frac{2u_b}{b}\right)^2 + \left(\frac{u_L}{L}\right)^2 + \left(\frac{u_{Q_f}}{Q_f}\right)^2 + \left(\frac{u_{\Gamma_i}}{\Gamma_i}\right)^2 + \left(\frac{2u_{\omega_f}}{\omega_f}\right)^2\right]^{1/2} \\ &= \left[(0.34)^2 + (2\times 0.125)^2 + (0.0217)^2 + (1.43)^2 + (0.59)^2 + (2\times 1.0)^2\right]^{1/2} \\ &= 2.56\%\end{aligned}$$

3) Uncertainty of Elastic Modulus

The uncertainty of the elastic modulus of the deposited material is associated with the spring constant of the cantilever which depends on many variables such as dimensional and material parameters. The relation between the elastic modulus of the deposited material and the spring constant is derived in (64). The effective Young's modulus of the composite cantilever is $168.08GPa$ and its thickness is $7.08\mu m \pm 10nm$. The nominal value of elastic modulus of nickel is $200GPa$ and its thickness is assumed as $1.0\mu m \pm 10nm$. The nominal spring constant of composite cantilever when the material is deposited is $75.9122N/m$. The uncertainty of spring constant (u_k) is $1.9434(N/m)$ and the spring constant of the composite cantilever is in the range of between 75.0476 and $76.7768(N/m)$.The elastic modulus of the nickel considering the uncertainty of spring constant is in the range of between 191.74 and $208.41GPa$ and its

uncertainty ($u_{E_{Ni}}$) is $8.41GPa$. Therefore the relative uncertainty of the elastic modulus of the nickel is

$$\frac{u_{E_{Ni}}}{E_{Ni}} = \frac{8.41}{200} = 0.0421 \Rightarrow 4.21\%$$

4) Uncertainty of Deflection due to the Misalignment of Two Cantilevers

In order to verify if residual stresses can be used as a means of the self-assembly during material deposition, two rectangular silicon cantilevers of AFM are connected to each other. However, the misalignment of two cantilevers happens in practice when they are put together. Fig. 17 represents the misalignment of two cantilevers, which combines the de-centered and rotational misalignment, and influences the deflection of the cantilevers during material deposition. However, the rotational misalignment of the cantilevers is not considered uncertain, since the variation in deflection due to the rotational misalignment is often small in practice comparing to that due to the de-centered misalignment. Therefore, the uncertainty due to the de-centered misalignment is only considered in this study.

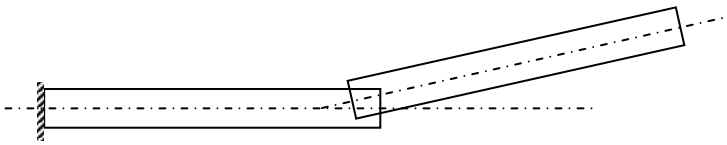

Fig. 17. Misalignment of two cantilevers in contact

The basic figure of the de-centered misalignment and its free body diagram when two cantilevers are putting together are shown in Fig. 18. Two cantilevers are linearly placed but connected to each other with the misaligned length of d .

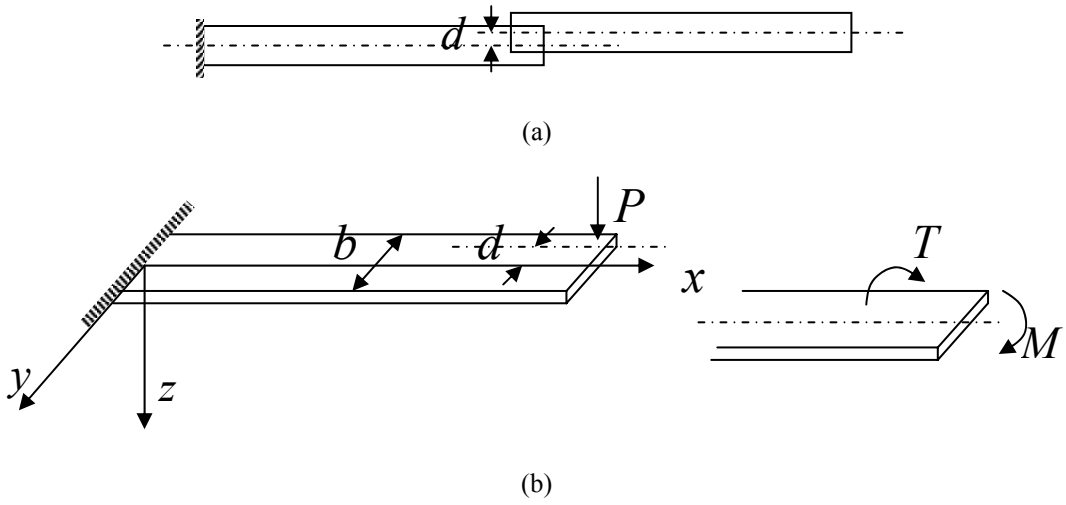

Fig. 18. Decentered misalignment (a) basic figure (b) free-body diagram

Material is electroplated onto the sensing cantilever, which produced residual stresses that deform the cantilever. This cantilever is attached to a second cantilever that is not electroplated. The sensing cantilever does work on the second cantilever during plating. Now simply assume that the de-centered force is acting on a second cantilever when two cantilevers are misaligned. The cantilever is bended and twisted due to the de-centered force and the end beam deflection is the sum of the deflection due to bending and due to torsion. The end beam deflection due to bending (ν_b) and due to torsion (ν_t) are expressed by

$$\nu_b = \frac{PL^3}{3EI} = \frac{4PL^3}{Ebh^3} \text{ and } \nu_t = \phi \frac{1}{2} b = \frac{PdL}{2\beta h^3 G} \tag{80}$$

where, ϕ is the twist angle of rectangular beam, expressed by

$\phi = \frac{TL}{\beta b h^3 G}$ and β is the value of parameter depends on the ratio of b/h.

Therefore, the total maximum end beam deflection due to de-centered force is

$$\nu_r = \nu_b + \nu_t = \frac{4PL^3}{Ebh^3} + \frac{PdL}{2\beta h^3 G} \tag{81}$$

The end beam deflection when two cantilevers are well aligned is

$$\nu = \frac{4PL^3}{Ebh^3} \tag{82}$$

The expected deflection error is

$$\Delta\nu = \nu_r - \nu = \frac{PdL}{2\beta h^3 G} \tag{83}$$

and the relative uncertainty of the deflection due to the de-centered force is

$$\frac{\Delta\delta}{\delta} = \frac{d \cdot E \cdot b}{8\beta G L^2} \tag{84}$$

When the de-centered length is assumed as 10% of the cantilever width, the relative uncertainty of the deflection is

$$\frac{\Delta\nu}{\nu} = 0.0017 \Rightarrow 0.17\%$$

IV. EXPERIMENTAL PROCEDURE

A. Experiment Set-up

Fig. 19 shows the experimental set-up for in-situ measurement of the deflection of the AFM sensing cantilever (which is also the working electrode of the electroplating process) during electroplating process with linear spring attached to the end point of cantilever.

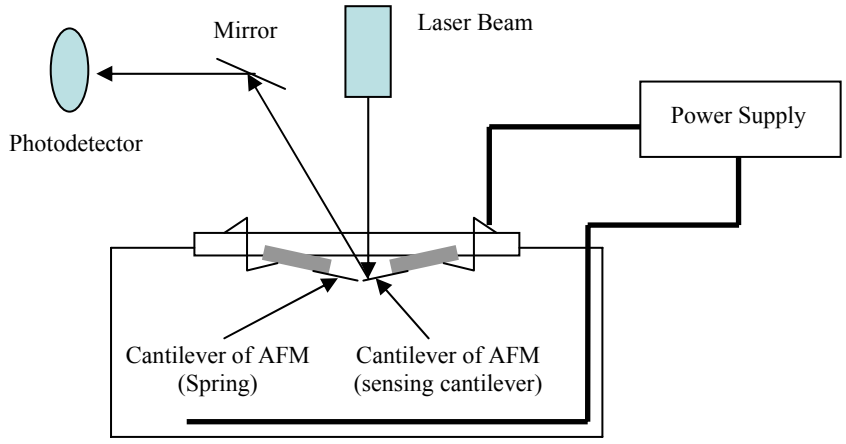

Fig. 19. Experimental set-up for measuring the deflection of AFM cantilevers

A standard atomic force microscope (Nanoscope IIIA of Digital Instruments Inc.) with its standard electrochemical cell is used for experiment [34]-[37].

The AFM cantilever used in experiment is shown in Fig. 20. The cantilever itself is rectangular and usually has a tapered free end for visibility during positioning. The cantilevers have a trapezoidal cross section with a wide side to reflect the laser beam that detects its motion. Cantilever width is usually given as the average (mean) of the two

sides of the trapezoid. These cantilevers can be purchased from MikroMasch, USA (Type A: NSC16/ Si_3N_4 /Cr-Au BS, Type B: NSC16/ Si_3N_4). Cantilevers have the dimension of $230\mu m \times 40\mu m \times 7.0\mu m$, the spring constant of 40N/m, and the resonant frequency of 170 kHz.

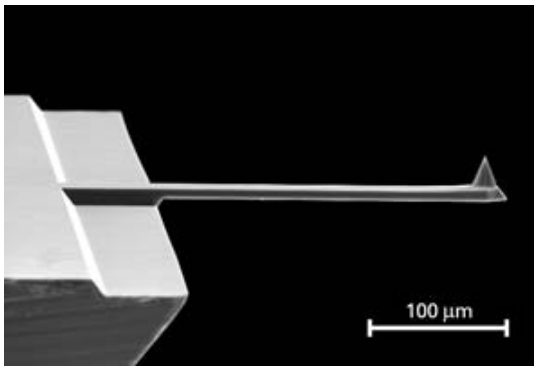

(a)

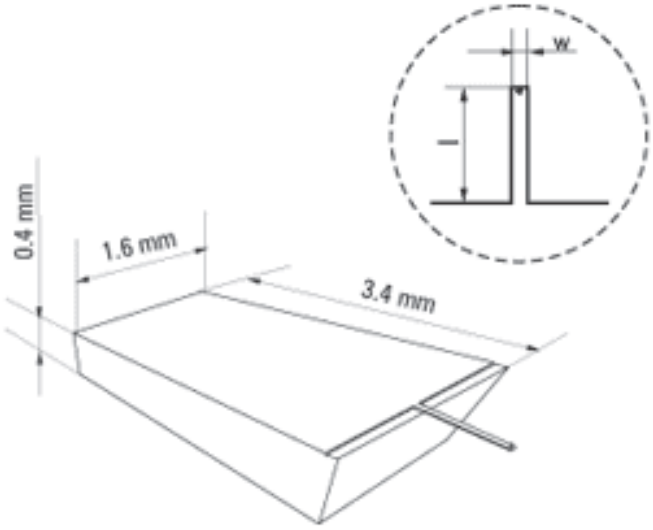

(b)

Fig. 20. SEM image of the silicon cantilever (a) and the dimension of the silicon chip (b)

Two kinds of silicon cantilever beams of AFM are used. Type A is the silicon cantilever with the silicon nitride and *Cr* / *Au* coating layers, which is used as a working electrode. Type B is the silicon cantilever with silicon nitride coating, which is used as a linear spring attached to the end point of the working electrode. Silicon nitride coating is applied to both sides of the cantilevers for electrical isolation. The coating thickness is about 10 nm. Thin layers of chromium (5 nm) and gold (50 nm) are coated onto the tip side of the plating cantilever. Thin layer of chromium is used in order to increase the adhesion of gold onto silicon nitride and the gold layer is used for the conductive seed layer during electroplating.

A standard power supply is used and connected to a two electrode system: the working electrode (WE), and the counter electrode (CE). The working electrode is the electrode where the potential is controlled and the current is measured. AFM cantilever of type A is used as the working electrode (WE) and the thin film during electroplating is deposited onto the tip side of the working electrode. The counter electrode is used to complete the cell circuit. The power supply measures the current between the working electrode and the counter electrode. Platinum wire counter electrode (Model: CHI115 from CH Instruments, Inc.) as the insoluble anode is used for the consistent experiment conditions.

Commercially available electrochemical cell (Fluid Image Cell & Accessory Kit from Digital Instrument) is used to measure the thickness of the deposited film and the deflection of the AFM cantilever in liquids. Fluid cells consist of a glass cantilever holder and silicon o-ring to form an enclosed fluid environment with the ability to

exchange liquids, as shown in Fig. 21. It also has the port holes to insert the electrodes and to deliver the solution into the cell. The cantilever holder consists of a small glass assembly with a wire clip for holding an AFM cantilever substrate. The glass surfaces provide a flat, beveled interface so that the AFM laser beam may pass into the fluid without being destroyed by an unstable fluid surface [61]. Generally AFM cantilever consists of the cantilever and the support chip. This cantilever is held in a small chip pocket on the bottom side of the cantilever holder by a gold-plated, stainless steel wire clip. The wire clip is held against the cantilever substrate by a tiny coil spring mounted on the top of the cantilever holder. The O-ring fits snugly and seals well around the cantilever chip pocket in the fluid cell. The electrochemical cell encloses the cantilever, and counter and reference electrodes are positioned within the cell for electrochemistry. Standard electrochemical cell has one chip pocket to hold the AFM cantilever. Another chip pocket with metallic spring clip is machined to hold another cantilever used as the spring attaching to the AFM cantilever for the second experiment.

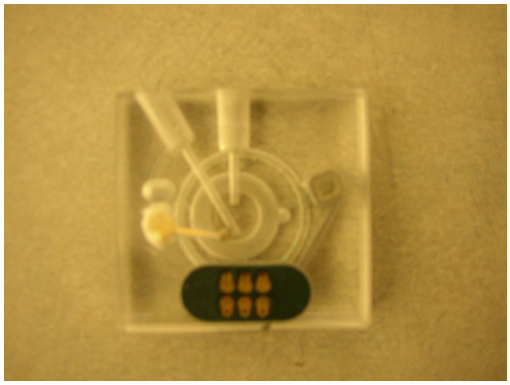

Fig. 21. Fluid cell used in AFM

The electrical contact with the coated side of the cantilever is achieved through the spring clip, a thin insulated wire glued with epoxy resin to the cantilever holder. The spring clip is then connected to the power supply. The counter electrode in the fluid cell is also connected to the power supply.

All-sulfate nickel solution is used for our experiments. This solution has been applied for the electrodepositing nickel where the auxiliary anodes are insoluble. The basic constituents for all-sulfate solution include: 225 ~ 410 g/L of nickel sulfate ($NiSO_4 \cdot 6H_2O$) as the primary source of nickel ions and 30 ~ 45 g/L of boric acid (H_3BO_3) to stabilize the pH of the solution and water. Nickel sulfate is nonvolatile, high conductive and soluble in water. Nickel carbonate ($NiCO_3$) can be added to control the pH and maintain the nickel ion concentration. Hydrogen peroxide and the activated carbon can be added into the solutions in order to remove the metallic and the organic contaminants.

All-sulfate solution has the optimized operating ranges for the minimum value of the residual stress, which are the pH of 1.5 to 4, the temperature of 38 to 70 $^{\circ}C$, and the current density of 1 to 10 A/dm^2. In order to have the high residual stress, the different operating conditions (pH>4 and the current density>10 A/dm^2) are used. To avoid bending of the cantilever due to temperature changes all solutions are kept at the same temperature. The constant current density using the power supply is used during electroplating process, which makes the thickness of the electrodeposited material is independent of the nickel ions concentration. The expected current density can be

obtained from the analytical results of the deposited film thickness. Demineralized water should be used in making up the bath, which has lower than 200 ppm of calcium content.

B. Experimental Procedure

The flowchart of the experimental procedure is given in Fig. 22. Each step in the flowchart will be discussed separately and sequentially.

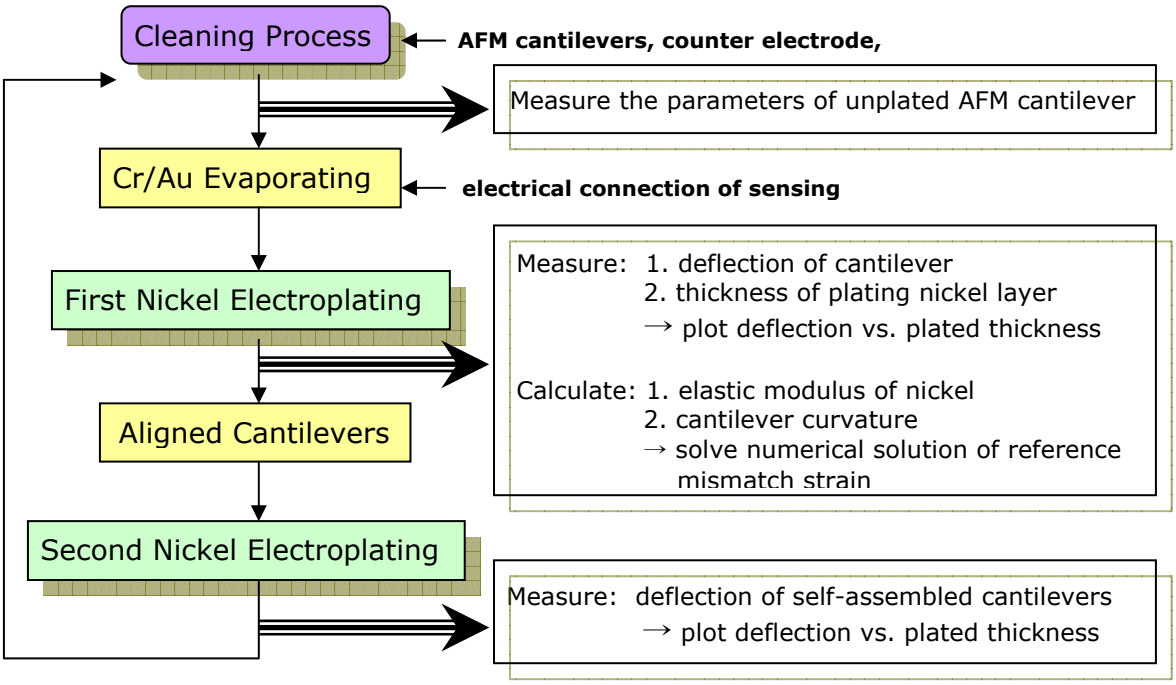

Fig. 22. Flowchart of the basic experiment procedure

1) Cleaning Process

The AFM cantilevers, counter electrode, tweezers, and beakers must be washed after any series of experiments by rinsing with water/methanol/water/acetone/water followed by vacuum drying. The purified DI water should be used.

The AFM's resolution can be limited by contaminations on the cantilever chip. In order to remove the contamination on the cantilever chip, position a UV lamp very close (3~5mm) to the cantilever chips and allow the unit to be irradiated for 15~30 minutes at full intensity.

In order to reduce contamination problems and obtain high-quality images, the fluid cell and O-ring must be as clean as possible. While soaking in warm, soapy water, place a few drops of liquid disk soap on the fluid cell and o-ring, then rub gently with a cotton swab or finger. Take care not to scratch the glass surface with any abrasive material. Rinse completely free of detergent with distilled water. Dry the fluid cell with $0.2\mu m$-filtered, compressed air or dry nitrogen until all moisture is evaporated.

2) Measure the Parameters of the Unplated AFM Cantilever

Take scanning electron microscope (SEM) pictures of the cantilevers and measure the length, width and thickness of the cantilevers before they are plated with nickel. Measure the resonant frequencies and quality factors of each cantilever in air using the AFM. Calculate the spring constant of each cantilever using Sadar's equation. Compare the calculated spring constant to the value determined by the Euler-Bernoulli beam theory.

The cantilever is supplied by the manufacturer with an electrical isolation layer of silicon nitride. This isolation layer will prevent the cantilever from plating on areas which are not coated with an evaporated Cr/Au layer. The quality of the silicon nitride isolation layer is verified by ensuring, using AFM and voltmeter, that there is no plating

onto the silicon nitride. Each cantilever is immersed into the plating solution without connecting the voltage source and the resonant frequency is measured. Then each cantilever is connected to the voltage source, and after some time, the resonant frequency is measured. If there is no plating and no chemical attack of the silicon nitride, then the resonant frequency should not be changed during immersing and connection to the voltage source.

3) Cr/Au Evaporation

Evaporate the Cr/Au layer ($Cr:5nm, Au:50nm$) onto the tip side of the cantilever (sensing cantilever) in order to have the conductivity. Cr/Au layer is only evaporated on the portion of the tip side cantilever and the step between the evaporated and un-evaporated layer is used for measuring the deposited layer thickness during electroplating, as shown in Fig. 23. Check if the current can pass through the cantilever using AFM and voltmeter. Measure the resonant frequencies and calculate the spring constants of each cantilever using Sadar's equation. The spring constants are also calculated using the Euler-Bernoulli theory.

Fig. 23. Making the step during the evaporation process

4) Nickel Plating Solution

Use a separate treatment tank to dissolve the nickel sulfate of 225 to 400 g/L in hot water at 38 to 49 $^{\circ}C$ to about 80% of desired volume. Add 1 to 2 m/L (0.8 to 1.6 pints/100gal) of 30% hydrogen peroxide; agitate briefly and allow settle for one hour. Add 1.2 to 2.4 g/L the activated carbon and agitate thoroughly. Heat to 66$^{\circ}C$, the add 1.2 to 2.4 g/L of nickel carbonate to the solution, with agitation to adjust the pH of 5.0 to 5.5. More nickel carbonate may be required and the mixture should be stirred to assist the dissolution of the carbonate. Allow to settle for 8 to 16 hours. Add and dissolve the boric acid of 30 to 45 g/L; add water to bring bath to its desired volume. Deionized or demineralized water which has lower than 200 ppm of calcium content should be used.

5) First Nickel Plating

The objective of this experiment is to measure the deflection of self-assembled cantilevers as a function of the deposited thin film thickness. However, AFM provides the function to measure the mechanical response of the cantilevers as a function of time. Therefore, the film thickness to be deposited on the surface of the sensing cantilever is in situ measured as a function of time during nickel electroplating at the first experiment. Then the deflection of self-assembled cantilevers is in situ monitored as a function of time at the second experiment with the same experiment conditions. Finally, the deflection of self-assembled cantilevers is expressed as a function of the deposited film thickness.

Experimental set-up for in-situ measurement of the film thickness to be deposited on the cantilever of AFM as a function of time during electroplating process is shown in Fig. 24.

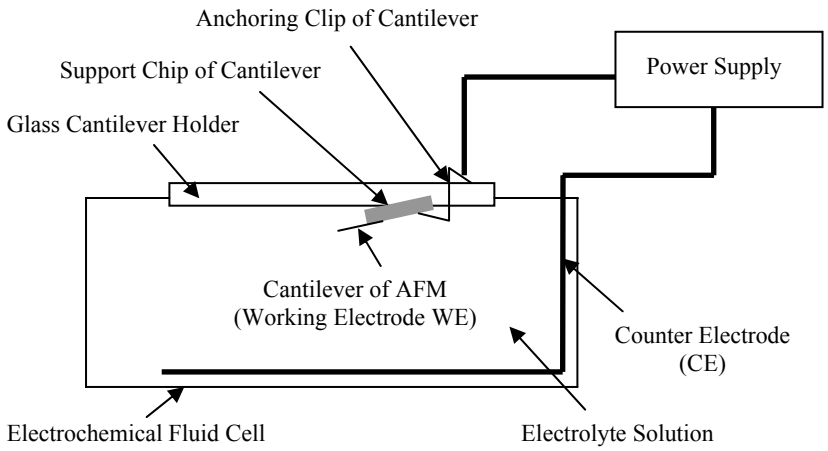

Fig. 24. Experimental set-up for measuring the deposited layer thickness

Plate the nickel onto the tip side of cantilever and measure the resonant frequency and quality factor in each plating time step. Measure the plated layer thickness in each plating time step using the profilometer. Calculate the spring constant using measured resonant frequency and quality factor. Calculate the elastic modulus (average value) of plated nickel layer using measured plated nickel thickness and the calculated spring constant. Measure the end beam deflection in every time step. Plot the plated layer thickness as a function of plating time. Plot the cantilever deflection as a function of plating time.

6) Make the Aligned AFM Cantilevers

Fig. 25 shows the experimental process for making the aligned AFM cantilevers. Two cantilevers are rectangular typed silicon cantilevers with silicon nitride coated. The tip side (bottom side) of the plating cantilever is coated with a layer of evaporated Cr/Au. These cantilevers are aligned and attached at their ends. The tip side of the plating cantilever should be placed on the back side of the other cantilever. Top view and side view of microscopes, two xyz positioners, tweezers and connecting bar are used for the experiments. The experimental procedures are as followed.

- Prepare the fixed AFM cantilever (Fig. 25 (a))

One AFM cantilever chip is placed on the post-it of the plate. The plate is connected to the holder which is anchored to the lab table.

- Bond one side of connecting bar on the surface of the cantilever chip (Fig. 25 (b))

One end of the connecting bar is dipped into the glue and grabbed at the end of the tweezers (scissor type) which is connected to the xyz positioner. The connecting bar is properly positioned on the surface of the cantilever chip using the xyz positioner. In plane alignment and the contact of the cantilever chip and the connecting bar is monitored through the top-viewing and the side-viewing microscope, respectively. Wait for complete bonding. After complete bonding, remove the tweezers carefully.

- Make the assembled cantilevers (Fig. 25 (c))

Second AFM cantilever chip is placed on the post-it of the plate which is connected to the xyz positioner. The other side of the connecting bar is glued and well positioned on the top of the second cantilever by controlling the second cantilever through xyz

positioner. In plane alignment and the contact of the cantilevers is monitored through the top-viewing and the side-viewing microscope, respectively. Check the movement of the cantilever carefully if the cantilevers are attached to each other. Wait for complete bonding. Carefully remove the cantilever assembly from the post-it after complete bonding. Check in-plane and side alignment of the cantilever tips using the microscope.

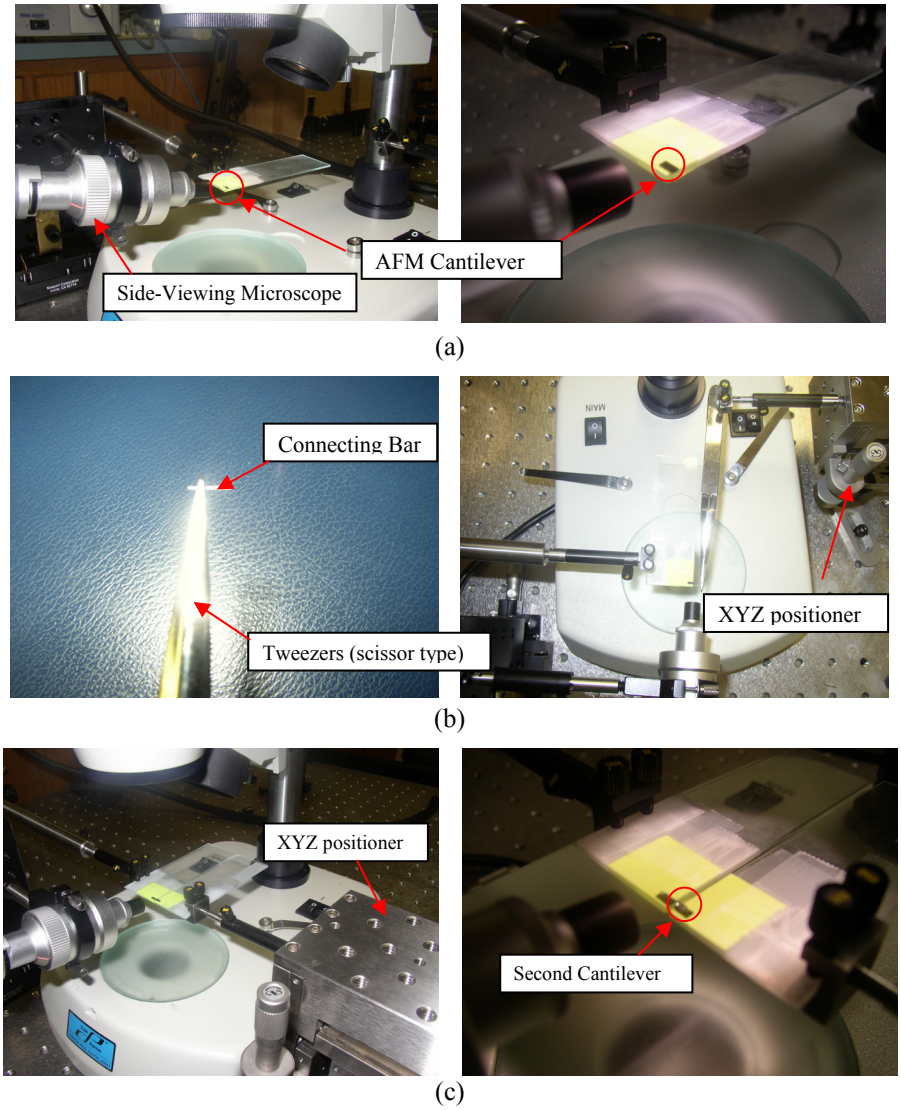

Fig. 25. The experimental process for making the aligned AFM cantilevers

7) Second Nickel Plating

Plate the nickel onto the tip side of the plating cantilever in each plating time step. The time step should be equal to that of the first plating. Measure and plot the end deflection of cantilever as a function of plating time.

V. RESULTS AND DISCUSSIONS

A. Experiment Results

1) First Plating Thickness Measurement

a) Geometry parameter and spring constant of cantilever

The typical dimensions of the cantilever used in this experiment are provided from the manufacturer and their variation ($L = 230 \pm 5 \mu m$, $b = 40 \pm 3 \mu m$ and $h = 7.0 \pm 0.5 \mu m$) significantly affects other parameters. Therefore, it is important that the cantilever dimensions be measured exactly. The scanning electron microscope (SEM) is used for measuring the cantilever dimensions in this experiment, which has the resolution of $10 nm$. Fig. 26 shows the SEM image of the cantilever.

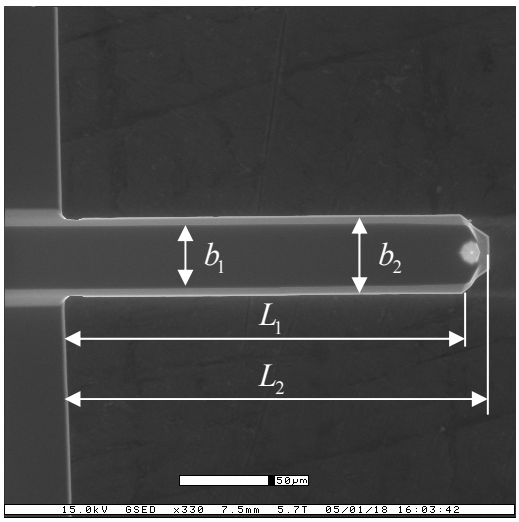

Fig. 26. SEM image of the cantilever sample

The cantilever has a trapezoidal cross section with a wide side to reflect the laser beam that detects its motion. It also has the non-perfect straight edge in length due to the probe tip. The average values of the measured dimensions are selected for the accuracy and listed in Table II. We now assess the accuracy of the measured dimensions and Sadar's method by presenting a detailed comparison with analytical method. Nine different samples of cantilevers were chosen for this comparison. First, the spring constants of these cantilevers were calculated using the Euler-Bernoulli beam theory, which used the measured cantilever dimensions. The resonant frequencies of these cantilevers were measured using Tapping Mode of the AFM, by driving the cantilever at a range of frequencies in the neighborhood of its fundamental mode resonance peak, and the spring constants using Sadar's method were determined. The measured resonant frequencies and the calculated spring constants of each cantilever are shown in Table II. The spring constants of each cantilever vary no more than 2.5%.

TABLE II

MEASURED DIMENSIONS AND SPRING CONSTANT COMPARISON FOR FIRST PLATING

	Cantilever Geometry (μm)				Spring Constant (N/m)	
#	L	b	h	$\omega_f(kHz)$	E - B	Sadar
A1	234.30	40.65	6.555	157.2480	37.6339	37.0664
A2	232.30	40.35	6.465	156.5593	36.7755	36.1594
A3	233.30	39.90	6.505	157.0243	36.5688	36.1226
A4	232.00	38.60	6.553	160.4008	36.7758	36.2583
A5	231.00	39.63	6.765	169.2104	42.0747	41.2498
A6	227.50	40.20	6.570	168.0084	40.9345	40.6273
A7	234.50	39.50	6.790	164.8308	40.5319	39.6051
A8	227.50	40.23	6.650	171.0988	42.4764	42.1667
A9	230.50	40.03	6.688	166.5630	41.3355	40.2865
average					39.4563	38.8380
standard deviation					2.4719	2.4271

Thin layers of chrome and gold ($Cr:5nm, Au:50nm$) are evaporated onto the tip side of the cantilever to serve as a seed layer for electroplating nickel. Cr/Au layers are only evaporated on the part of the tip side cantilever and the step between the evaporated and un-evaporated layer is used for measuring the deposited layer thickness during electroplating. The resonant frequencies of the Cr/Au coated cantilevers were measured and the spring constants were compared again. The measured resonant frequencies and the determined spring constants of each cantilever are shown in Table III. The spring constants of each cantilever vary 2.0% at most.

TABLE III

SPRING CONSTANT COMPARISON OF Cr/Au COATED CANTILEVERS FOR FIRST PLATING

	Cantilever Geometry (μm)				Spring constant (N/m)	
#	L	b	Cr/Au	$\omega_f(kHz)$	E - B	Sadar
A1	234.30	40.65	0.0502	153.6696	38.0624	37.3545
A2	232.30	40.35	0.0502	152.9954	37.2000	36.4400
A3	233.30	39.90	0.0502	153.4716	36.9883	36.4133
A4	232.00	38.60	0.0502	158.5048	37.2328	37.3641
A5	231.00	39.63	0.0502	166.8990	42.5814	42.3497
A6	227.50	40.20	0.0502	165.5390	41.4418	41.6228
A7	234.50	39.50	0.0502	162.2974	41.0183	40.5204
A8	227.50	40.23	0.0502	168.6088	42.9966	43.2127
A9	230.50	40.03	0.0502	164.5394	41.8389	41.4875
average					39.9289	39.6406
standard deviation					2.5104	2.7222

b) First measurement of the plating nickel thickness

Nickel was plated onto the tip side of the cantilevers and their thicknesses were measured using the surface profile measuring system. The recommended current density

for nickel plating is in the range of $2 \sim 10 A/dm^2$. The platinum counter electrode with area of $7.85 \times 10^{-4} dm^2$ was used for the nickel plating. Therefore, the input current of the power supply was set to $0.004 A$ which made the current density in the recommended range $(J = 5.1 A/dm^2)$. In order to make sure if the plating thickness is consistent, nickel was plated in two different plating time steps and its thickness was measured in every plating time step.

Fig. 27 and Fig. 28 show the total plating thickness of each cantilever and the comparison of the average and analytical plating thickness when the plating time step is $15 s$. The thickness of plated nickel is increased as increasing the plating time and the average value of the plating thickness is similar to the analytical plating thickness.

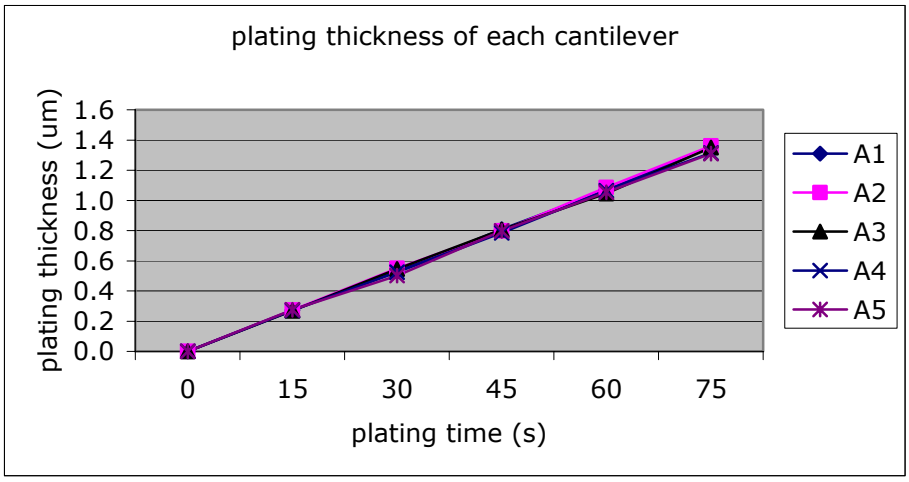

Fig. 27. Total plating thickness of each cantilever when plating time step is 15s

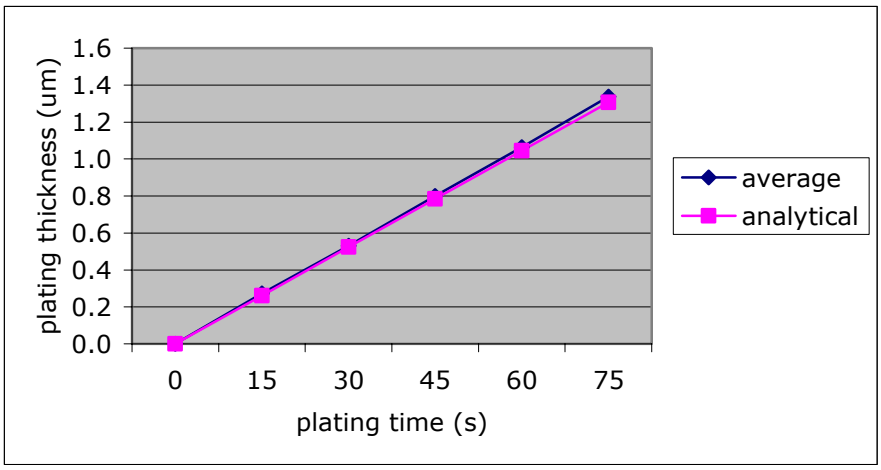

Fig. 28. Comparison of the average and the analytical plating thickness when plating time step is 15s

Fig. 29 and Fig. 30 give the measured plating thickness of each cantilever and a comparison of the average and analytical plating thickness in each plating time step. The plating thicknesses of each cantilever in each plating time step should be identical but they were different due to the errors of the thickness measurement and the plated time. The maximum thickness difference of each cantilever to the average thickness is 13% and the maximum difference of the average thickness to the analytical value is less than 4% .

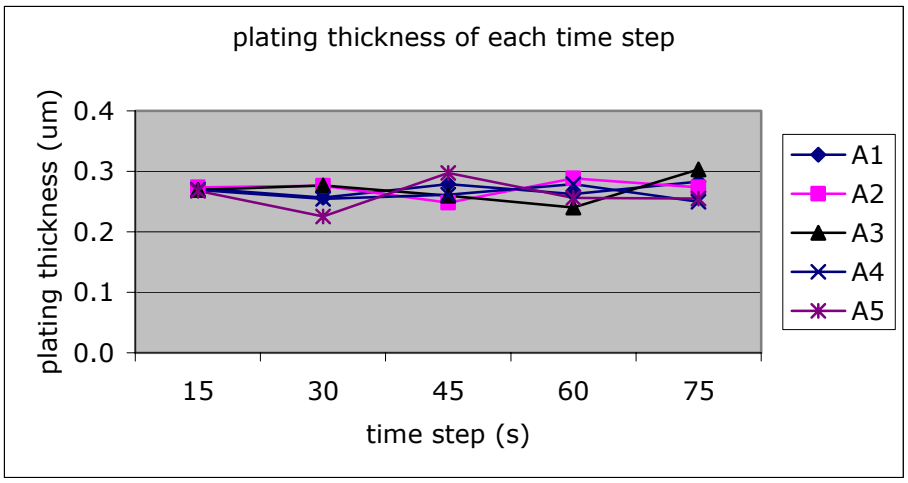

Fig. 29. Plating thickness of each cantilever in each plating time step when plating time step is 15s

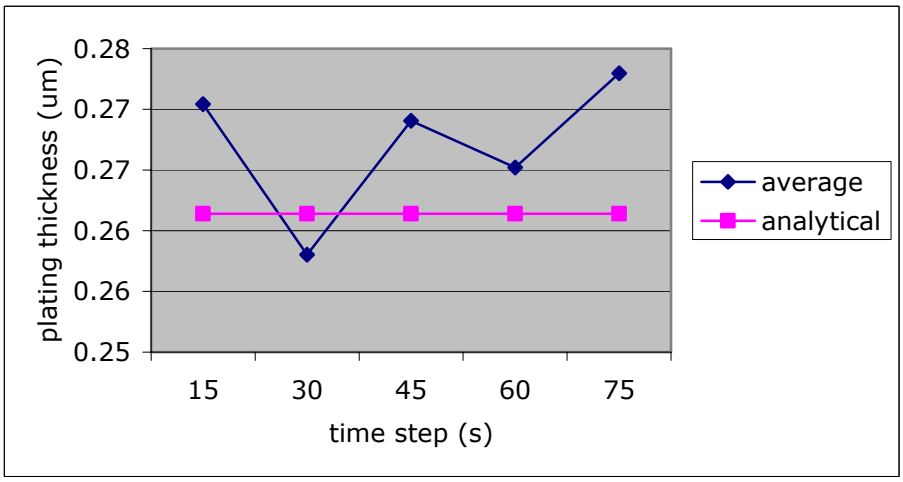

Fig. 30. Comparison of average and analytical plating thickness in each plating time step when plating time step is 15s

The resonant frequencies of each cantilever were also measured in each plating time step and the spring constants were calculated using Sadar's equation. The measured resonant frequencies (kHz) and the calculated spring constants (N/m) in each plating

time step are listed in Table IV. The elastic moduli of the plated nickel were also determined by using Euler-Bernoulli beam theory, expressed in equation (64). The measured elastic modulus of nickel in each time step is in the range of between $162.68 \sim 175.71 GPa$ and the average elastic modulus is $170.73 GPa$.

TABLE IV

RESONANT FREQUENCY AND SPRING CONSTANT WHEN PLATING TIME STEP IS 15s

	15 sec		30 sec		45 sec		60 sec		75 sec	
	ω_f	k_{Sadar}	ω_f	k_{Sadar}	ω_f	k_{Sadar}	ω_f	k_{Sadar}	ω_f	k_{Sadar}
A1	154.2	42.9	154.9	48.3	155.8	54.3	156.9	60.4	158.3	67.2
A2	153.9	42.1	154.2	47.5	155.3	52.9	156.4	59.4	157.9	65.9
A3	154.3	41.9	155.0	47.6	155.9	53.3	157.2	58.8	158.7	65.9
A4	157.6	42.1	157.8	47.0	158.8	52.6	159.8	58.7	161.3	64.8
A5	166.3	48.0	166.6	53.1	167.2	59.9	167.9	66.1	169.3	72.9

For checking the consistency of the plating thickness, nickel was plated on different sets of cantilevers in different plating time steps and its thickness was measured in every plating time step. Fig. 31 and Fig. 32 show total plating thickness of each cantilever and the comparison of the average and analytical plating thickness when the plating time step is $20\,\mathrm{s}$. The thickness of plated nickel is also increased as increasing the plating time and the average value of the plating thickness is similar to the analytical plating thickness.

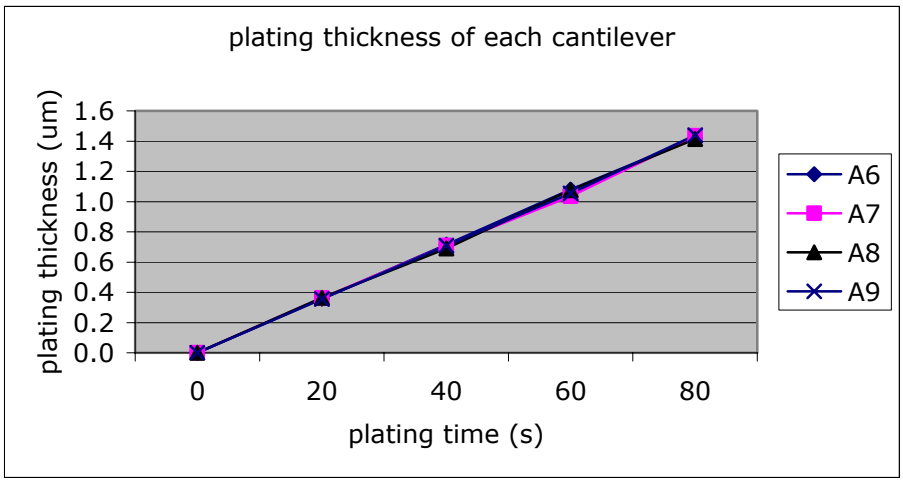

Fig. 31. Total plating thickness of each cantilever when plating time step is 20s

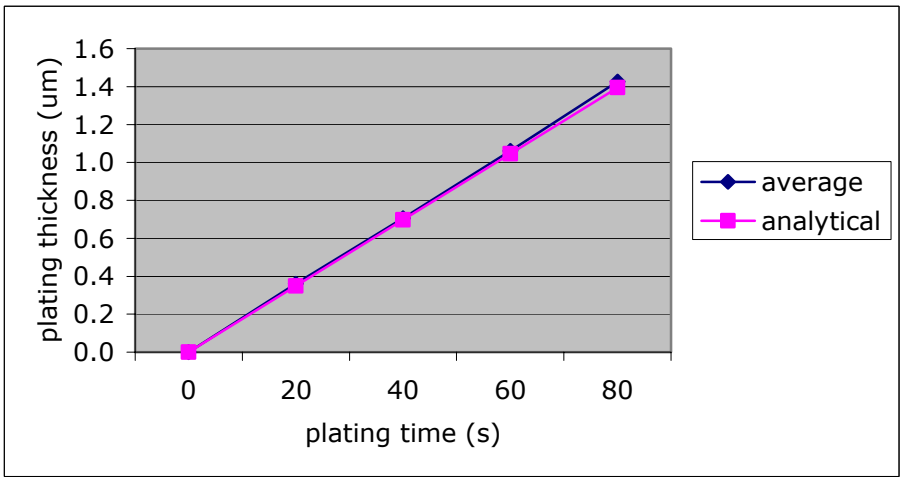

Fig. 32. Comparison of average and the analytical plating thickness when plating time step is 20s

Fig. 33 and Fig. 34 give the measured plating thickness of each cantilever and comparison of the average and analytical plating thickness in each plating time step. As with the 15s time step, the plating thicknesses of each cantilever in each plating time step were also different. The maximum thickness difference of each cantilever to the

average thickness is 12% and the maximum difference of the average thickness to the analytical value is less than 2% .

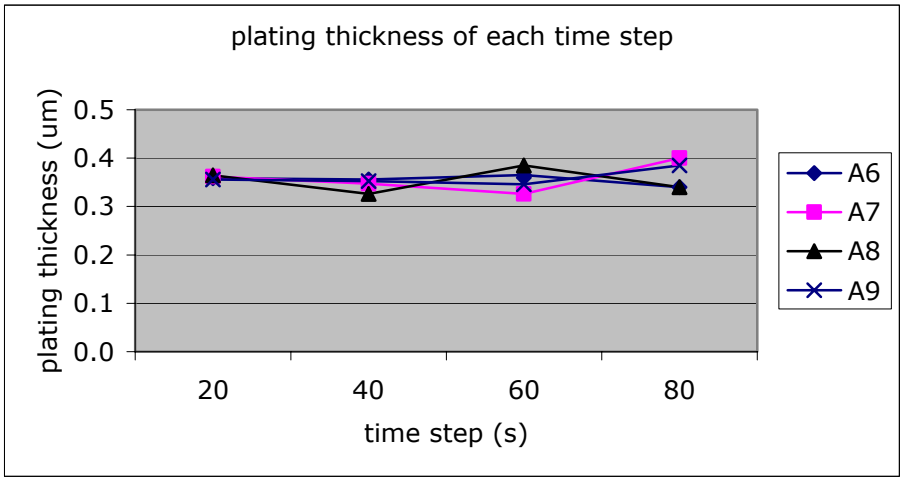

Fig. 33. Plating thickness of each cantilever in each plating time step when plating time step is 20s

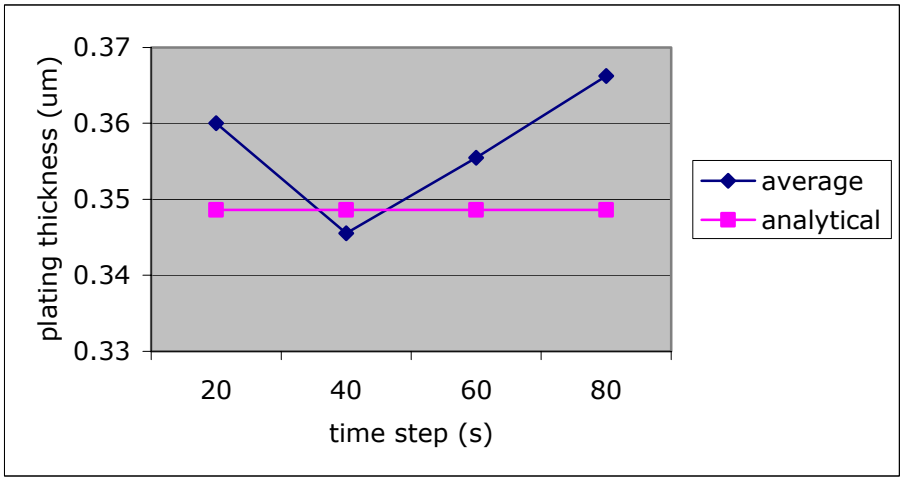

Fig. 34. Comparison of average and analytical plating thickness in each plating time step when plating time step is 20s

The resonant frequencies of each cantilever were also measured in each plating time step and the spring constants were calculated using Sadar's equation. Table V gives the measured resonant frequencies (kHz) and the calculated spring constants (N/m) in each plating time step. The elastic moduli of the plated nickel were also determined by using Euler-Bernoulli beam theory. The elastic modulus of nickel in each time step is in the range of between $162.09 \sim 174.88 GPa$ and the average elastic modulus is $171.06 GPa$.

TABLE V

RESONANT FREQUENCY AND SPRING CONSTANT WHEN PLATING TIME STEP IS 20s

	20 sec		40 sec		60 sec		80 sec	
	ω_f	k_{Sadar}	ω_f	k_{Sadar}	ω_f	k_{Sadar}	ω_f	k_{Sadar}
A6	164.7	48.8	165.6	56.9	167.0	65.8	169.0	75.0
A7	162.4	48.1	162.9	55.7	163.8	63.2	165.3	73.0
A8	167.6	50.7	168.1	58.2	169.5	67.7	171.3	77.0
A9	165.0	49.4	165.7	57.4	166.8	65.7	168.4	75.6

As shown in Fig. 27 and Fig. 31, the total plating thicknesses of two different plating time steps are consistent and the maximum difference of plating thickness in each step is less than 5% . Fig. 35 and Fig. 36 represent the images and surface roughness of the cantilever after plating. The nickel was well plated onto the surface of the cantilever and its average surface roughness is less than 30 nm.

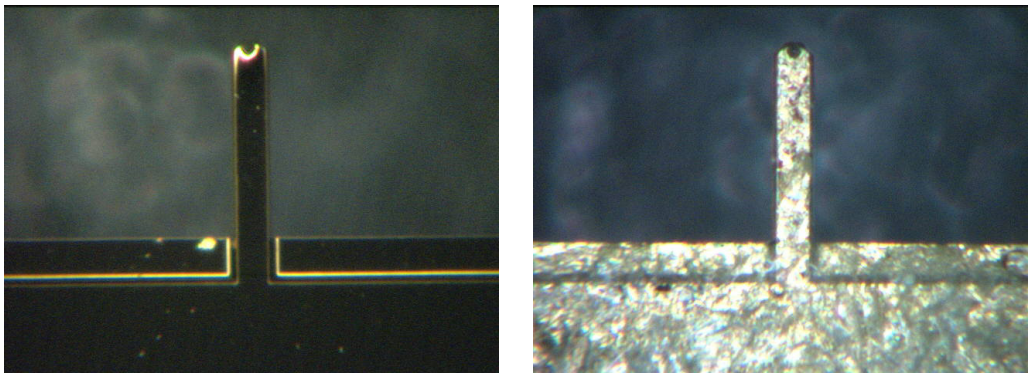

(a) (b)

Fig. 35. Images of the cantilever during plating (a) initial (b) after plating

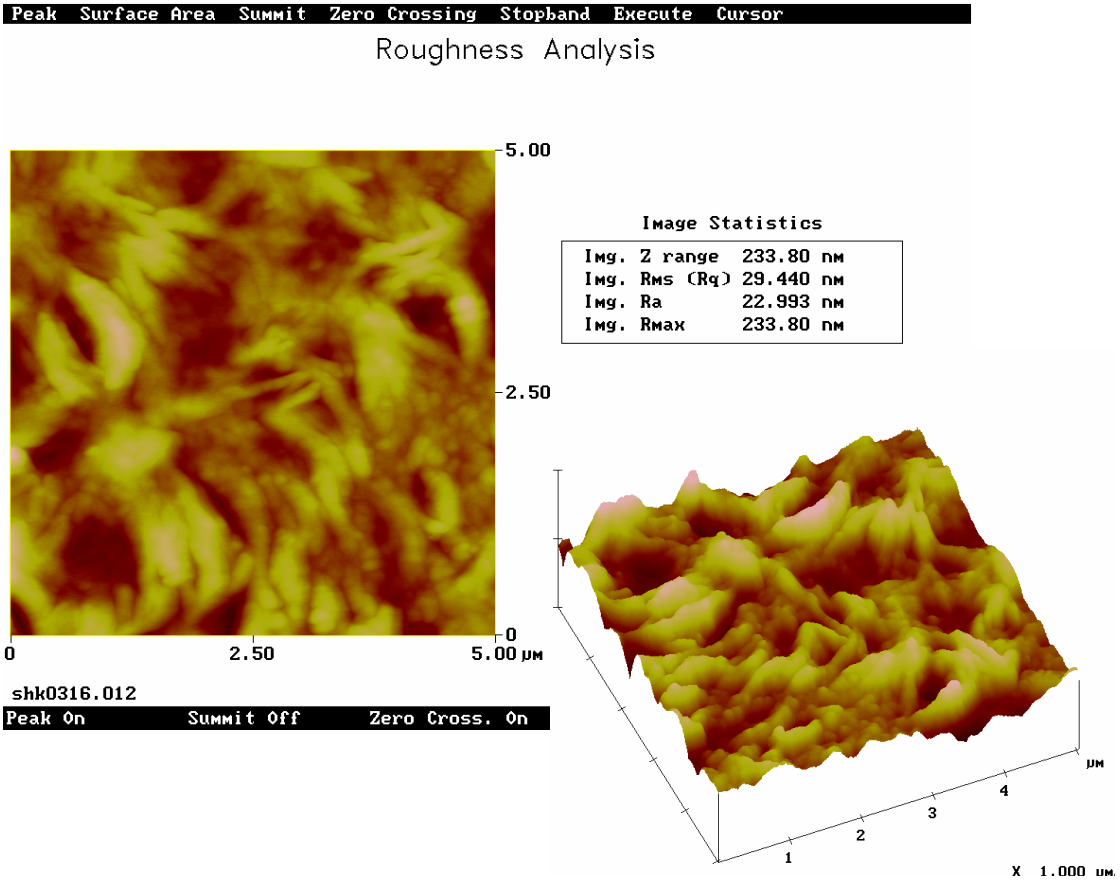

Fig. 36. Surface roughness of the cantilever after plating

2) Second Plating Thickness Measurement

As explained in chapter III, the nickel ion dissolved in the solution is deposited onto the cantilever during plating. Generally the nickel ion in the solution can be refreshed from the soluble counter electrode, but there is no refreshment of the nickel ion due to the use of the insoluble counter electrode in this experiment. In previous section, the nickel is plated onto each cantilever surface in the beaker. However, the plating is done in liquid cell for measuring the deflection of the cantilever. The volume of the liquid cell is relatively smaller than the beaker used in the previous experiment and the concentration change of the nickel in the solution during plating might affect the plating thickness. In order to verify the consistency of the experiment condition, the nickel is plated again in liquid cell and its plating thickness is compared.

a) Geometry parameter and spring constant of cantilever

Four different cantilevers were selected for this experiment and their dimensions were measured by scanning electron microscopy. Table VI gives the average values of the measured dimensions and the spring constant comparisons of each cantilever. The spring constants of each cantilever are almost similar and less than 1.0% difference range.

TABLE VI

MEASURED DIMENSIONS AND SPRING CONSTANT COMPARISON FOR SECOND PLATING

	Cantilever Geometry (μm)				Spring constant (N/m)	
#	L	b	h	$\omega_f(kHz)$	E - B	Sadar
B1	240.80	39.96	6.795	157.5230	37.9526	37.5776
B2	240.79	41.04	6.695	154.1588	37.2908	36.9637
B3	240.80	39.74	6.825	158.5970	38.2447	37.8814
B4	241.23	39.96	7.015	164.8308	41.5284	41.2174
average					38.7541	38.4100
standard deviation					1.8921	1.9101

Thin layers of chrome and gold ($Cr:5nm, Au:50nm$) were evaporated onto the tip side of the cantilever in order to have the conductivity for a seed layer for electroplating nickel. The resonant frequencies of the Cr/Au coated cantilevers were measured and the spring constants were compared again. The measured resonant frequencies and the determined spring constants of each cantilever are shown in Table VII. The spring constants of each cantilever are almost similar and less than 1.2% difference range.

TABLE VII

SPRING CONSTANT COMPARISON OF Cr/Au COATED CANTILEVERS FOR SECOND PLATING

	Cantilever Geometry (μm)				Spring constant (N/m)	
#	L	b	Cr/Au	$\omega_f(kHz)$	E - B	Sadar
B1	240.80	39.96	0.0502	154.0968	38.3696	37.9494
B2	240.79	41.04	0.0502	150.6956	37.7065	37.2747
B3	240.80	39.74	0.0502	155.1968	38.6670	38.2844
B4	241.23	39.96	0.0502	161.2164	41.9707	41.6101
average					39.1785	38.7797
standard deviation					1.9043	1.9331

b) Second measurement of the plating nickel thickness

Nickel was plated onto the tip side of the cantilevers in the liquid cell and their thicknesses were measured using the surface profile measuring system in air. The plating time step is 15s and its thickness was measured in every plating time step. Fig. 37 shows the experiment set-up for plating in the liquid cell.

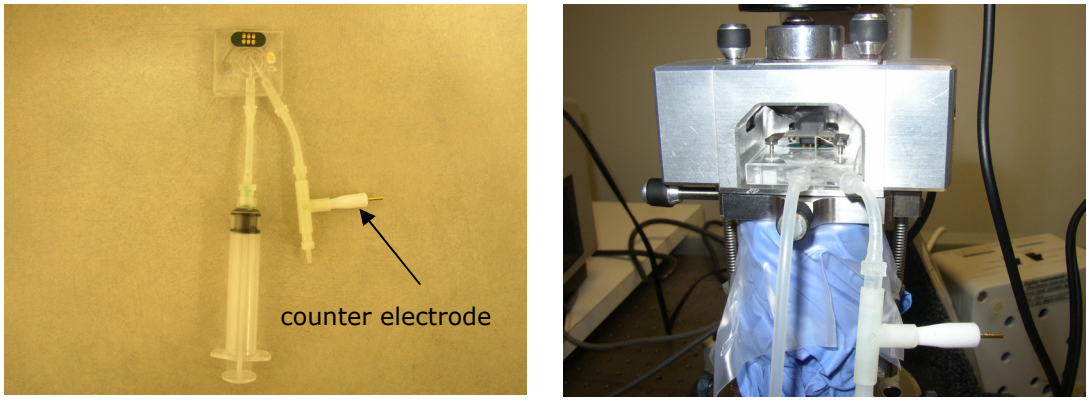

(a) (b)

Fig. 37. Experiment set-up for plating in liquid cell (a) connection of counter electrode into liquid cell (b) loading the liquid cell into AFM holder

Fig. 38 and Fig. 39 show the total plating thickness of each cantilever and the comparison of the average and analytical plating thickness. The thickness of plated nickel is increased with increasing plating time and the average value of the plating thickness is similar to the analytical plating thickness.

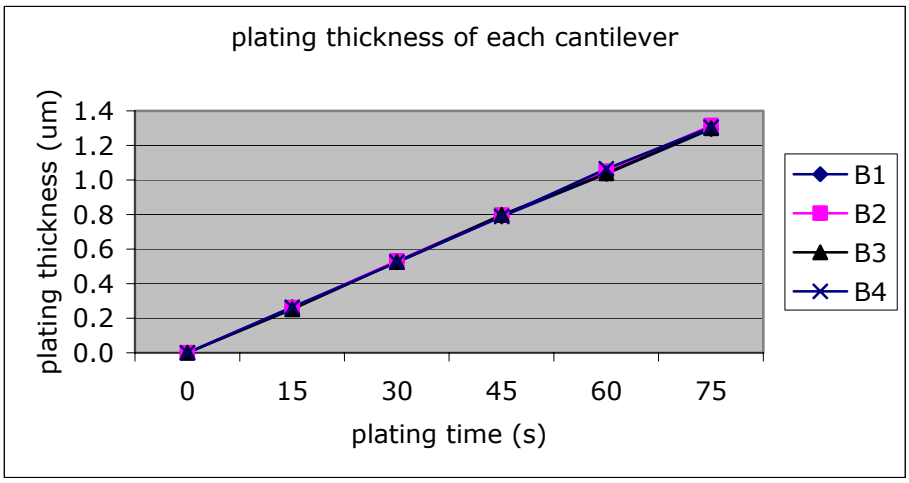

Fig. 38. Total plating thickness of each cantilever (plated in liquid cell)

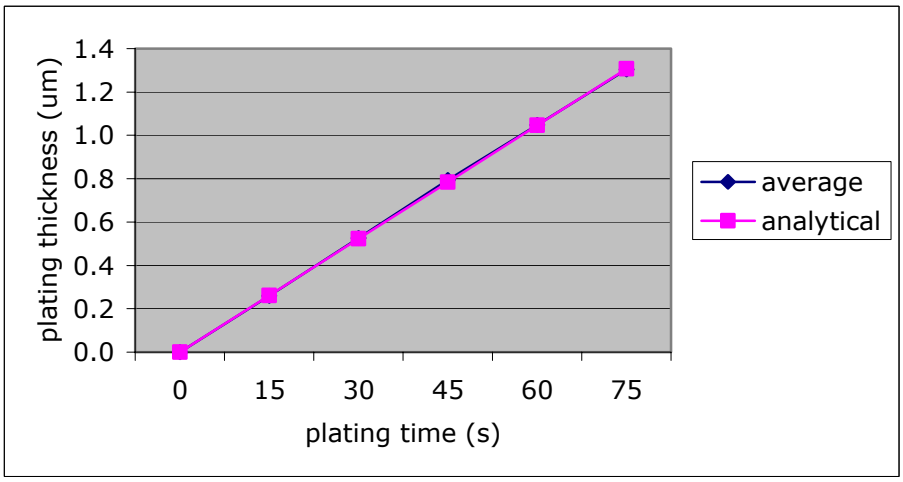

Fig. 39. Comparison of the average and analytical plating thickness (plated in liquid cell)

Fig. 40 and Fig. 41 give the measured plating thickness of each cantilever and comparison of the average and analytical plating thickness in each plating time step. Like the previous plating, the plating thicknesses of each cantilever in each plating time step were also different. The maximum thickness difference of each cantilever to the

average thickness is 8% and the maximum difference of the average thickness to the analytical value is less than 0.5% .

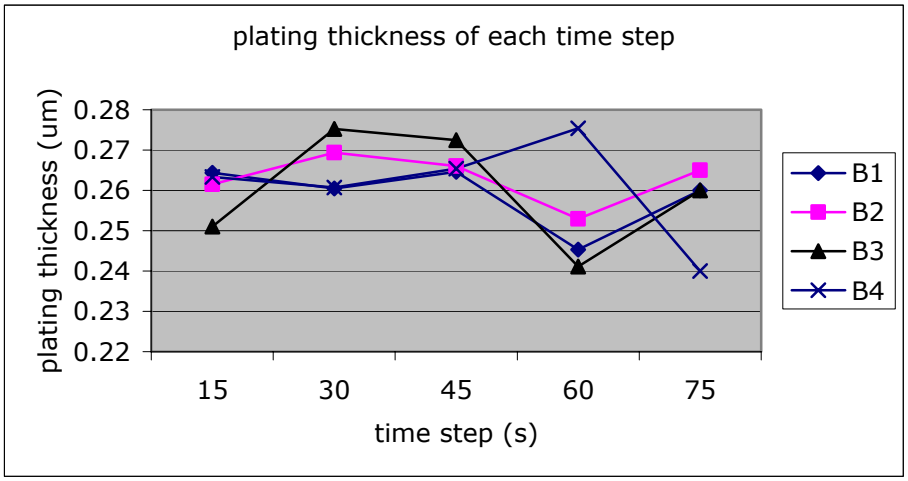

Fig. 40. Plating thickness of each cantilever in each plating time step (plated in liquid cell)

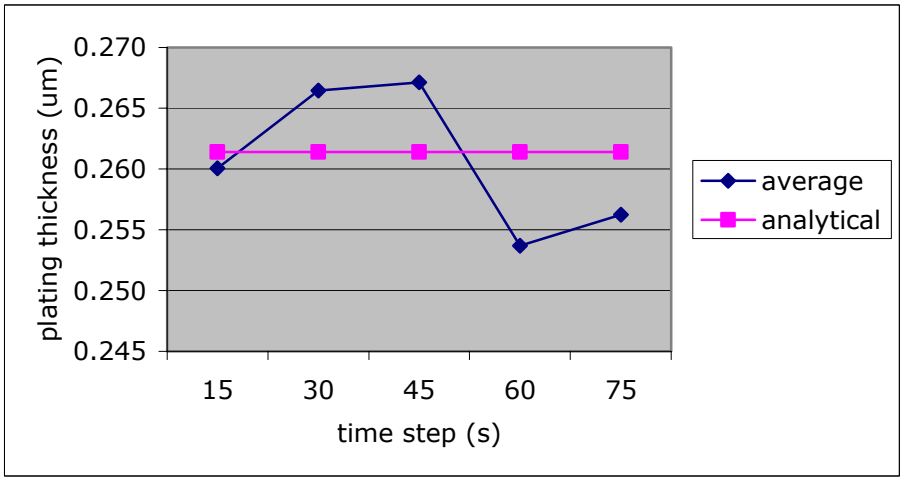

Fig. 41. Comparison of the average and analytical plating thickness in each plating time step (plated in liquid cell)

The resonant frequencies of each cantilever were also measured in each plating time step and the spring constants were calculated using Sadar's equation. Table VIII gives the measured resonant frequencies (kHz) and the calculated spring constants (N/m) in each plating time step. The elastic moduli of the plated nickel were also determined by using Euler-Bernoulli beam theory. The measured elastic modulus of nickel in each time step is in the range of between $163.48 \sim 176.29 GPa$ and the average elastic modulus is $171.31 GPa$.

TABLE VIII

RESONANT FREQUENCY AND SPRING CONSTANT DURING SECOND PLATING

	15 sec		30 sec		45 sec		60 sec		75 sec	
	ω_f	k_{Sadar}	ω_f	k_{Sadar}	ω_f	k_{Sadar}	ω_f	k_{Sadar}	ω_f	k_{Sadar}
B1	153.9	43.0	154.1	48.2	154.2	53.4	155.4	59.1	156.9	65.5
B2	150.6	42.2	151.4	47.9	151.7	53.2	152.5	58.7	153.9	65.1
B3	154.9	43.0	155.2	48.6	156.0	54.5	156.5	59.7	157.9	66.1
B4	160.8	47.0	160.8	52.6	161.1	58.4	161.6	64.7	162.3	70.4

As shown in Fig. 27 and Fig. 38, the measured total plating thicknesses plated in the beaker and the liquid cell are consistent and the maximum difference of plating thickness in each step is less than 2% . Fig. 42 and Fig. 43 represent the images and surface roughness of the cantilever after plating in liquid cell. Nickel was also well plated onto the surface of the cantilever and its surface roughness was similar to that of the cantilever plated in the beaker.

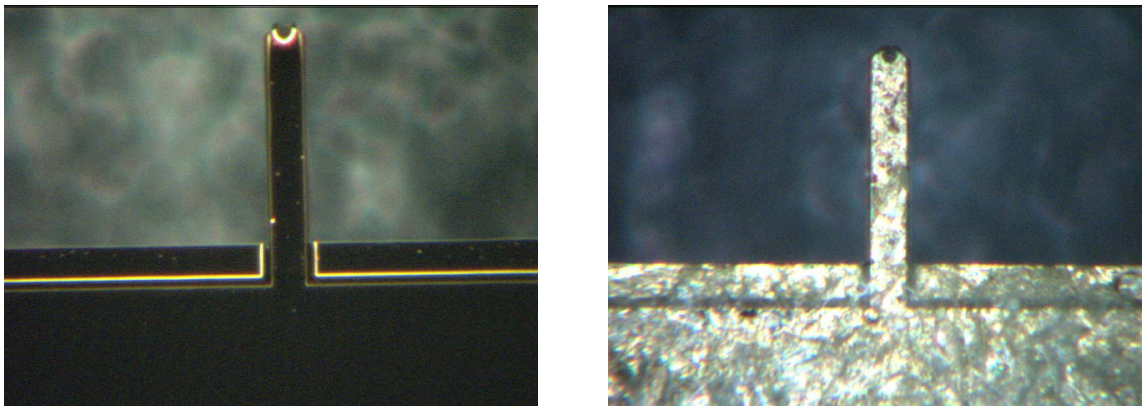

(a) (b)

Fig. 42. Images of the cantilever during plating (a) initial (b) after plating in liquid cell

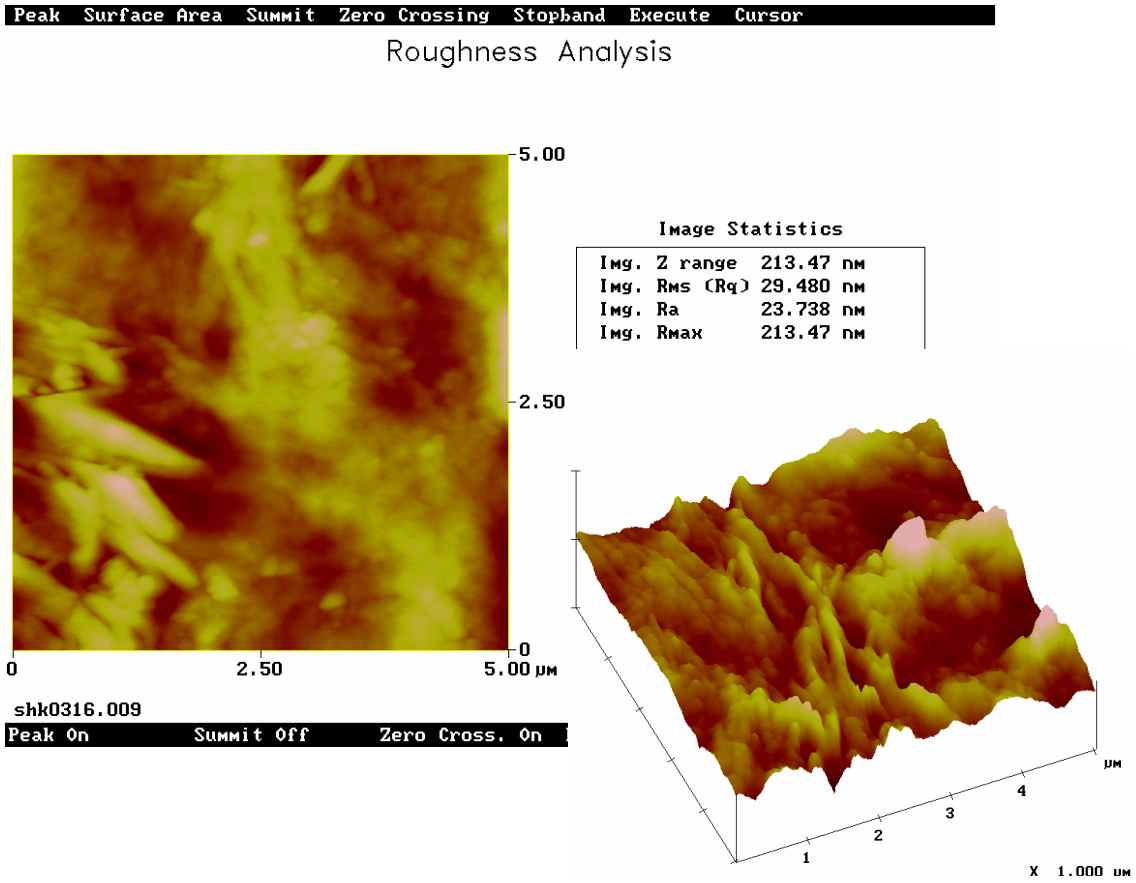

Fig. 43. Surface roughness of the cantilever after plating

Nickel was sometimes not well plated onto the cantilever in the liquid cell due to the dust on the cantilever surface and the air bubbles around the cantilever, which induced wrong results, that is, the measured resonant frequency during plating in liquid cell was sometimes out of limit or much greater. Fig. 44 shows the example of the bad plating cantilever.

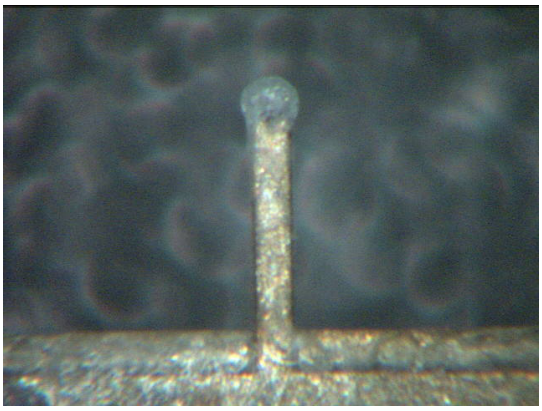

Fig. 44. Image of the bad plating cantilever

3) Measurement of the Deflection of Single Cantilever

a) Geometry parameter and spring constant of cantilever

Six different cantilevers were selected for this experiment and their dimensions were measured by scanning electron microscopy. Table IX gives the average values of the measured dimensions and the spring constant comparisons of each cantilever. The spring constants of each cantilever are almost similar and less than 1.7% difference range.

TABLE IX

MEASURED DIMENSIONS AND SPRING CONSTANT COMPARISON FOR SINGLE CANTILEVER DEFLECTION

	Cantilever Geometry (μm)				Spring constant (N/m)	
#	L	b	h	$\omega_f(kHz)$	E - B	Sadar
C1	225.63	39.84	6.265	159.0154	36.0696	35.7724
C2	225.83	39.84	6.215	156.2248	35.1214	34.5588
C3	222.15	40.05	6.370	168.0040	39.9284	39.5214
C4	221.35	40.47	6.350	168.5170	40.4041	40.0363
C5	223.78	38.35	6.230	159.9530	34.9971	34.5529
C6	223.79	39.41	6.320	163.0664	37.5370	36.9072
average					37.3429	36.8915
standard deviation					2.3729	2.4070

Thin layers of chrome and gold were evaporated onto the tip side of the cantilever. The resonant frequencies of the Cr/Au coated cantilevers were measured and the spring constants were compared again. The measured resonant frequencies and the determined spring constants of each cantilever are shown in Table X. The spring constants of each cantilever are almost similar and less than 1.1% difference range.

TABLE X

SPRING CONSTANT COMPARISON OF Cr/Au COATED CANTILEVERS FOR SINGLE CANTILEVER DEFLECTION

	Cantilever Geometry (μm)				Spring constant (N/m)	
#	L	b	Cr/Au	$\omega_f(kHz)$	E - B	Sadar
C1	225.63	39.84	0.0502	156.5542	36.4987	36.5910
C2	225.83	39.84	0.0502	153.7994	35.5425	35.3462
C3	222.15	40.05	0.0502	165.3708	40.3958	40.4098
C4	221.35	40.47	0.0502	165.9910	40.8785	40.9931
C5	223.78	38.35	0.0502	157.4744	35.4157	35.3424
C6	223.79	39.41	0.0502	160.1686	37.9797	37.5763
average					37.7852	37.7098
standard deviation					2.3967	2.4711

b) Deflection measurement

Nickel was plating onto the tip side of the cantilevers in the liquid cell and the end deflection of each cantilever was measured using the Atomic Force Microscopy. Before plating, the signal sensitivities of each cantilever were measured. The signal sensitivity is the sensitivity measurement of the photodetector's voltage output signal to the cantilever deflection by using the force calibration plot. Fig. 45 shows the example of the force calibration plot of the cantilever.

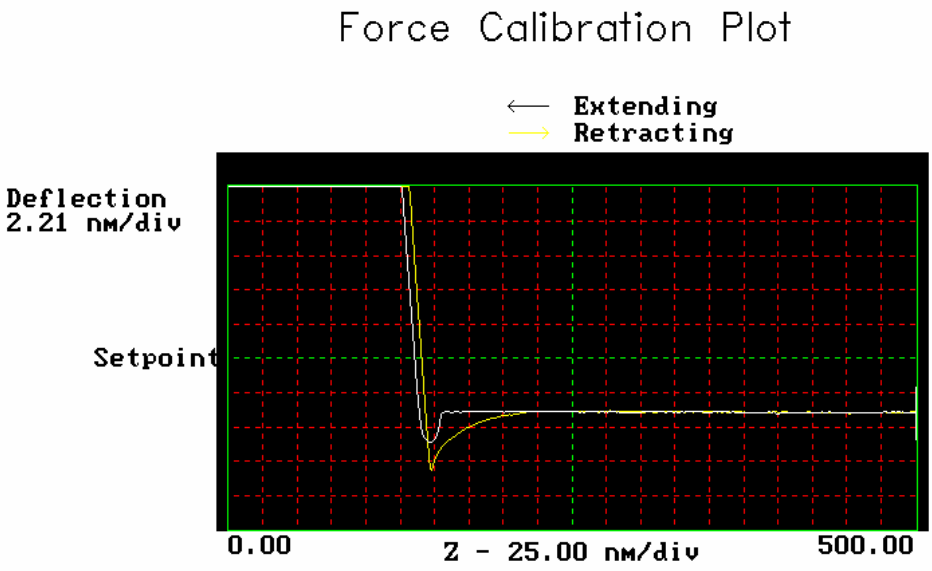

Fig. 45. Force calibration plot for detector's sensitivity of the cantilever

After that, nickel was plated onto the tip side of the cantilevers in the liquid cell and the end deflections of each cantilever during plating were measured by simply

multiplying the detector's voltage output signal difference to the photodetector sensitivity of each cantilever.

Fig. 46 shows the total end deflection of each cantilever during plating. As expected, the total deflection of each cantilever is increased as the plating time is increased. The deflection of the cantilever with lower spring constant is greater than that with higher spring constant. The end deflections of each cantilever in each plating time step are shown in Figure 47. The rate of deflection with plating time of each cantilever is decreasing, which agrees with other experimental results [62], except the cantilever $C1$. The end deflection of the cantilever $C1$ in last plating step is increased due to the error of the output voltage change measurement or the plated time.

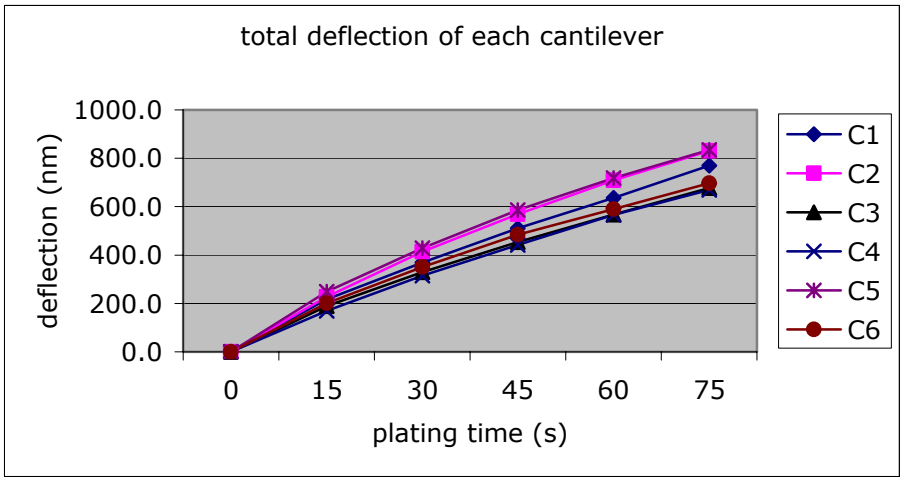

Fig. 46. Total end deflection of each cantilever during plating

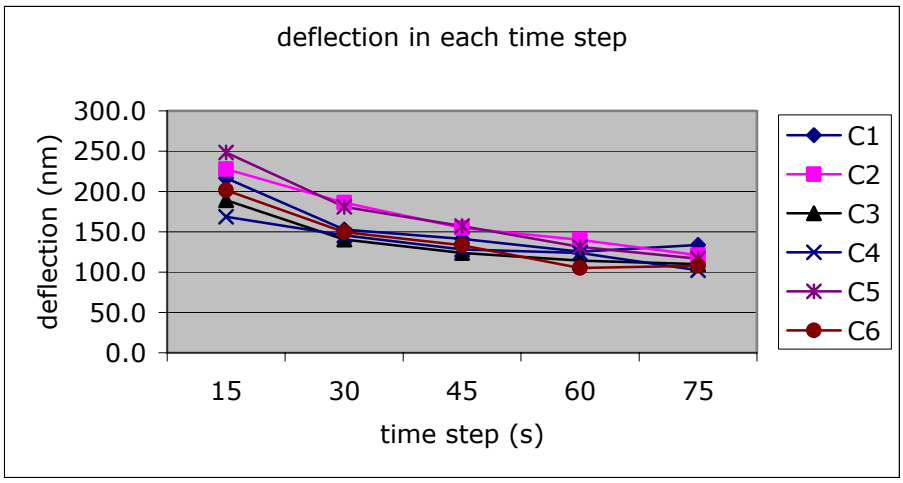

Fig. 47. End deflection of each cantilever in each plating time step during plating

Fig. 48 and Fig. 49 present the average total deflection and the average deflection in each plating time step as a function of the plating thickness. The average deflection is obtained by averaging the deflection of each cantilever and the plating thickness is determined from the average thickness of each cantilever plated in liquid cell.

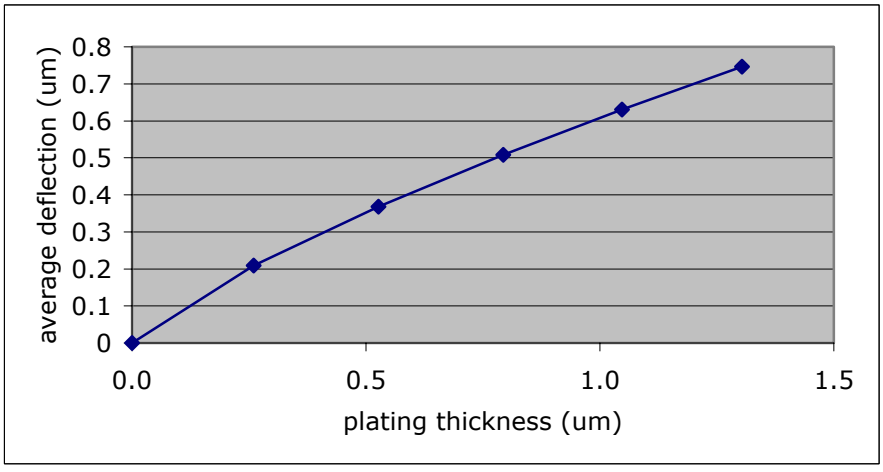

Fig. 48. Average total deflection as a function of the average plating layer thickness

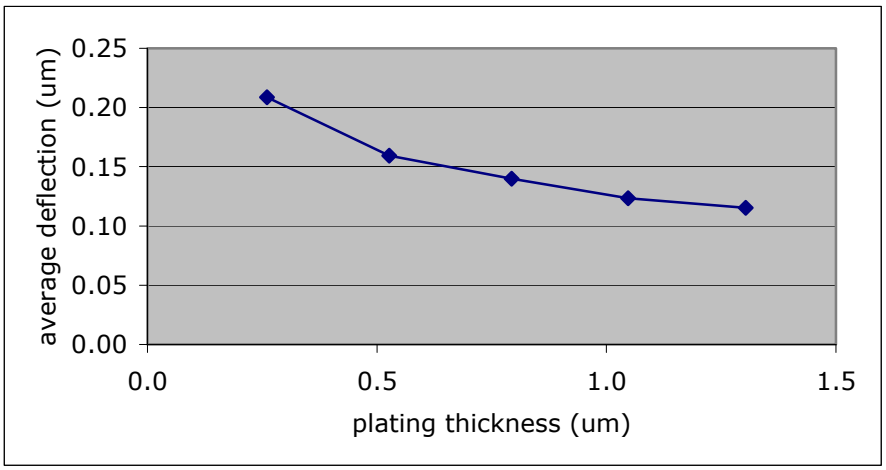

Fig. 49. Average deflection in each time step as a function of average plating thickness

4) Measurement of the Deflection of Aligned Cantilevers

a) Geometry parameter and spring constant of cantilever

Five different cantilevers were selected for this experiment and their dimensions were measured by scanning electron microscopy. Table XI gives the average values of the measured dimensions and the spring constant comparisons of each cantilever. The spring constants of each cantilever differ by 2.6% at most.

TABLE XI

MEASURED DIMENSIONS AND SPRING CONSTANT COMPARISON FOR ALIGNED CANTILEVER DEFLECTION

	Cantilever Geometry (μm)				Spring constant (N/m)	
#	L	b	h	$\omega_f(kHz)$	E - B	Sadar
D1	235.50	41.15	6.505	155.4330	36.6673	36.8487
D2	235.00	40.80	6.515	156.4123	36.7566	36.9176
D3	231.00	39.50	6.665	165.6734	40.1081	39.4138
D4	231.50	39.88	6.710	166.3890	41.0508	40.2251
D5	230.50	40.03	6.688	166.5630	41.3355	40.2865
average					39.1837	38.7383
standard deviation					2.3018	1.7284

Thin layers of chrome and gold are evaporated onto the tip side of the cantilever. The resonant frequencies of the Cr/Au coated cantilevers were measured and the spring constants were compared again. The measured resonant frequencies and the determined spring constants of each cantilever are shown in Table XII. The spring constants of each cantilever are almost similar and less than 2.5% difference range.

TABLE XII

SPRING CONSTANT COMPARISON OF Cr/Au COATED CANTILEVERS FOR ALIGNED CANTILEVER DEFLECTION

	Cantilever Geometry (μm)				Spring constant (N/m)	
#	L	b	Cr/Au	$\omega_f(kHz)$	E - B	Sadar
D1	235.50	41.15	0.0502	153.2715	36.9865	37.9199
D2	235.00	40.80	0.0502	154.1443	37.0761	37.9452
D3	231.00	39.50	0.0502	162.5968	40.5983	40.0630
D4	231.50	39.88	0.0502	164.1416	41.5492	41.3105
D5	230.50	40.03	0.0502	164.5394	41.8389	41.4875
average					39.6098	39.7452
standard deviation					2.3984	1.7435

b) Deflection measurement

First, the signal sensitivities of each cantilever were also measured. After that, the aligned cantilevers were made for self-assembly. Fig. 50 shows the images of the aligned cantilevers.

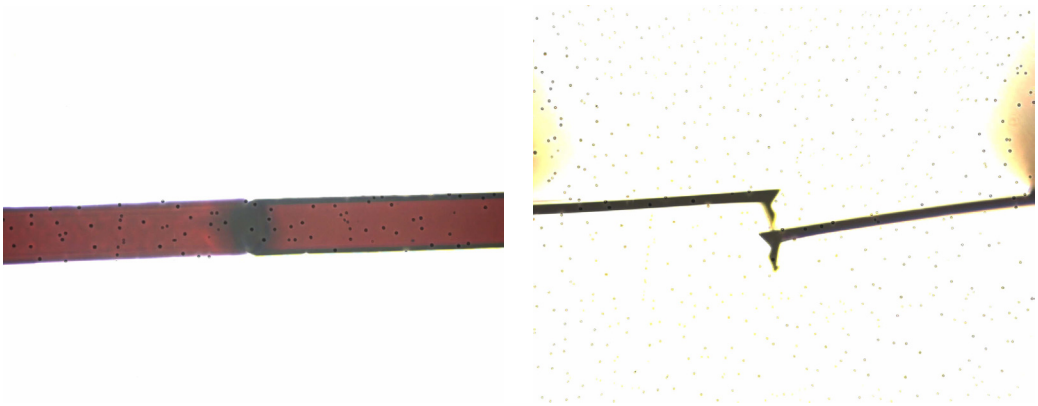

(a) (b)

Fig. 50. Images of the aligned cantilevers (a) top view (b) side view

Nickel was plated onto the tip side of the sensing cantilevers in the liquid cell and the end deflection of each cantilever during plating was measured by multiplying the detector's voltage output signal difference to the photodetector sensitivity of each cantilever.

Fig. 51 shows the total end deflection of the cantilevers during plating. As expected, the total deflection of each cantilever increases with increasing plating time. Comparing the deflection of the single cantilever shown in Fig. 46, it is found that the deflection of the aligned cantilevers is less than that of the single cantilevers due to the cantilever

working as the spring attaching to the deposition cantilever. The end deflection of each cantilever in each plating time step is shown in Fig. 52. The rate of deflection of each cantilever decreases with increasing plating time. The deflection of the cantilever with the lower spring constant is greater than that with higher spring constant, except cantilever $D4$. The spring constant of cantilever $D4$ is greater than that of cantilever $D2$ but its deflection in first plating step is larger than that of cantilever $D2$. This might be due to the error of the output voltage change measurement or the plated time. It also might occur because the cantilevers were not initially in contact and the deposit cantilever was deflected as a single cantilever until it contacted the spring cantilever.

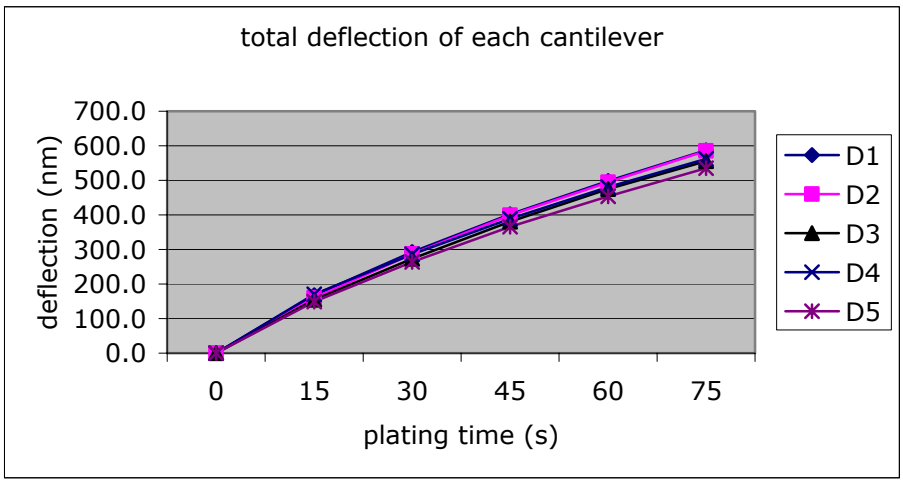

Fig. 51. Total end deflection of the aligned cantilever during plating

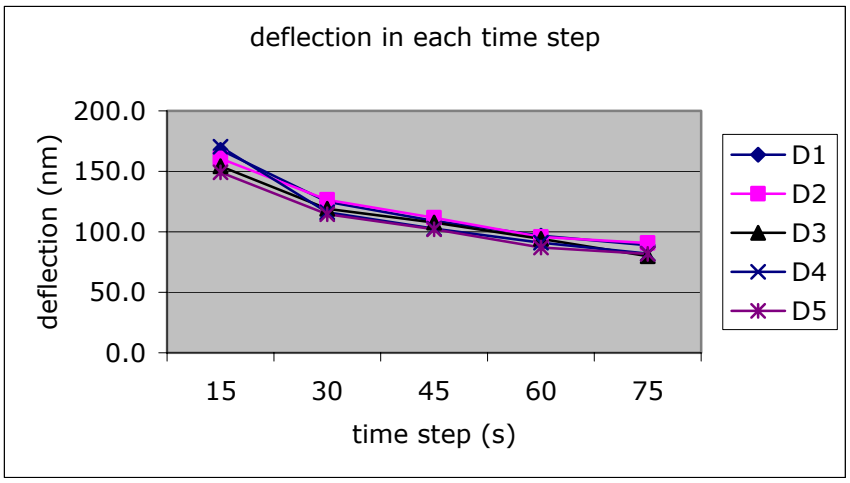

Fig. 52. Deflection of the aligned cantilever in each plating time step during plating

Fig. 53 and Fig. 54 show the average total deflection and the average deflection of the aligned cantilevers in each plating time step as a function of the plating thickness. The average deflection is also obtained by averaging the deflection of each cantilever.

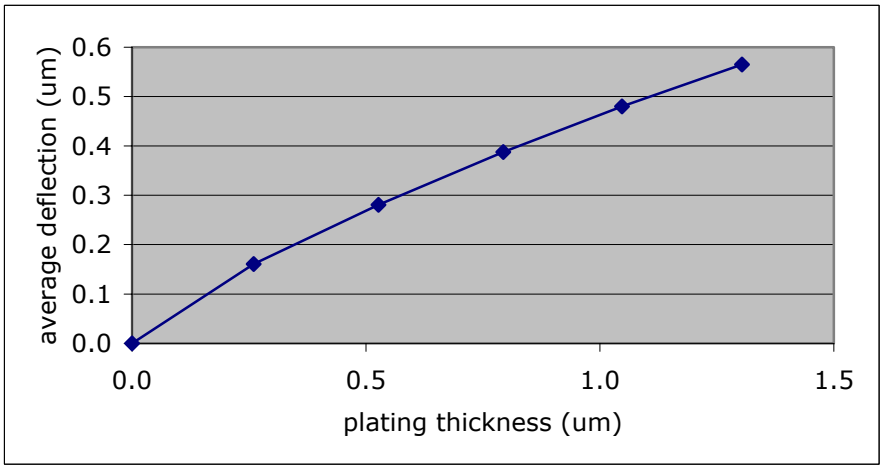

Fig. 53. Average total deflection as a function of average plating thickness

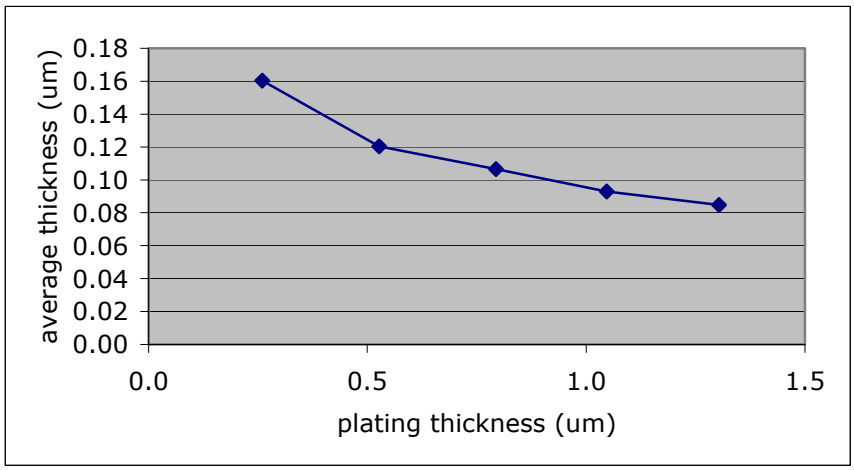

Fig. 54. Average deflection in each time step as a function of average plating thickness

B. Numerical Results of Mismatch Strain

The mismatch strain produced during the film growth is numerically solved by using the experiment results. First, the cantilever curvature is calculated using (44) and the measured total end beam deflections of single cantilevers, as shown in Fig. 46. Fig. 55 shows the calculated curvatures of each cantilever and the average curvature as a function of the plating thickness. As expected, the curvatures of each cantilever are increasing as increasing the plating thickness.

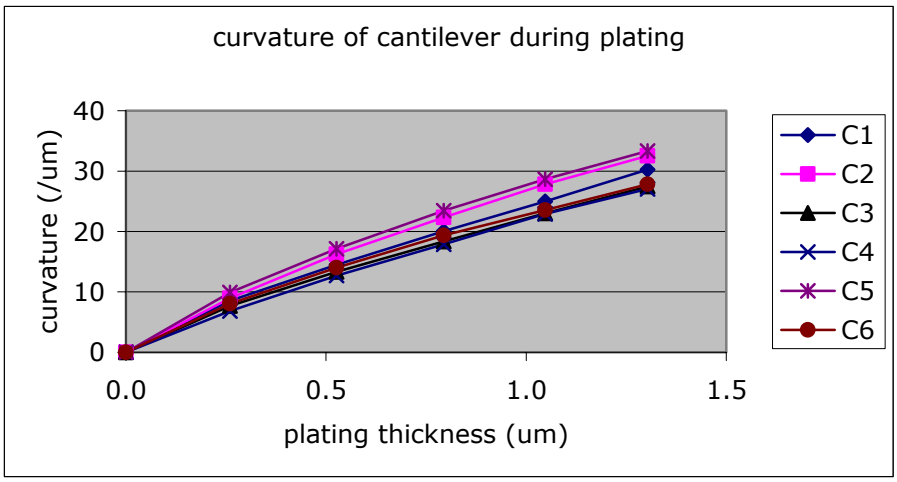

(a)

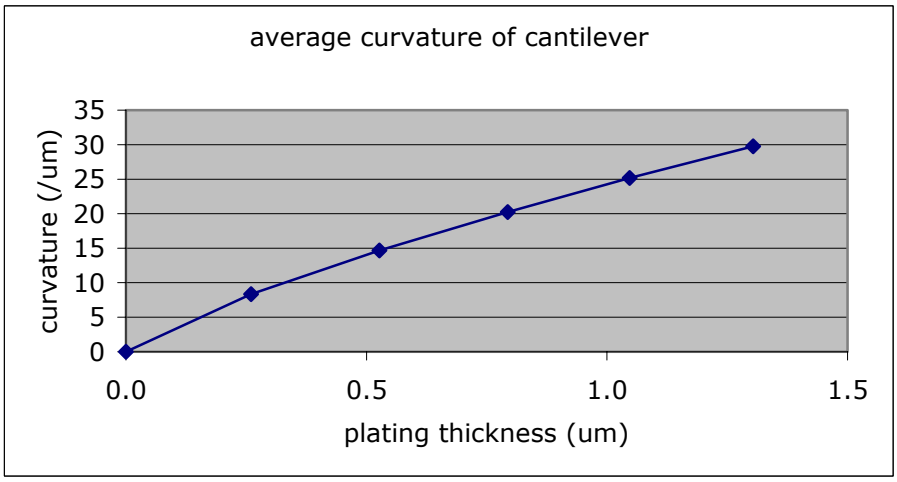

(b)

Fig. 55. Curvature as a function of plating thickness during plating (a) curvatures of each cantilever (b) average curvature of cantilever

Now the reference mismatch strain, which varies in the out-of-plane direction, is obtained using (39) and the calculated average cantilever curvature. Fig. 56 shows the calculated reference mismatch strain distribution in the thickness direction. This

analytical result indicates that the reference mismatch strain is decreasing in the out-of plane direction, which is similar to the other experiment results [62].

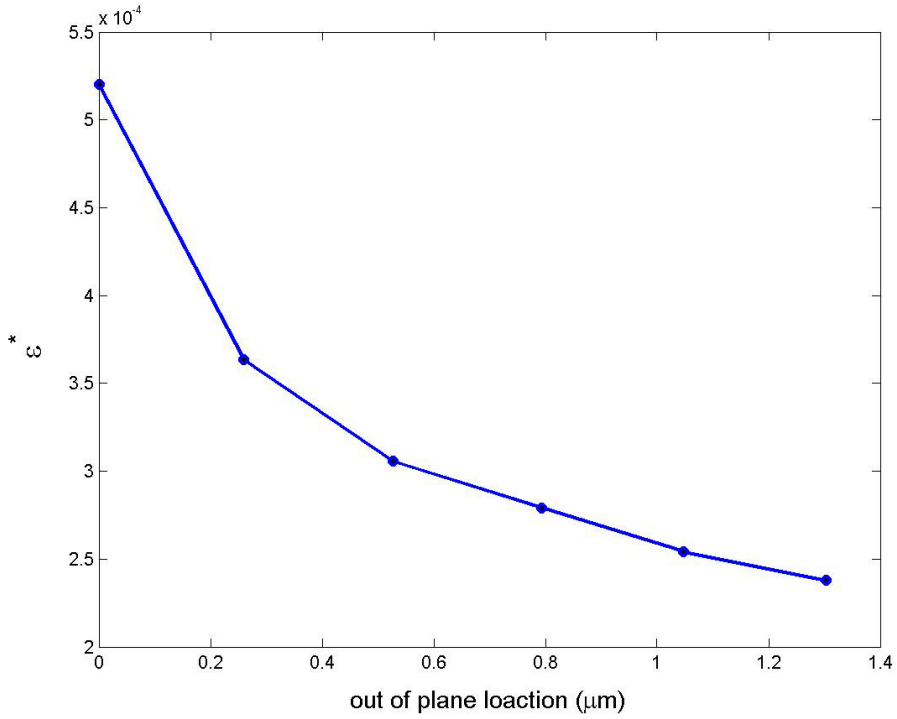

Fig. 56. Calculated reference mismatch strain from the experiment

The end deflection of the aligned cantilevers is analytically solved by using (31) and the calculated reference mismatch strain, and compared to the experimentally measured deflection during plating, which is shown in Fig. 53. Fig. 57 gives the comparison of the aligned cantilever deflection between analysis and experiment. The analytical result is well fit to the experimental result with the maximum difference of 10.0% , which indicates that the analytically derived deflection equation does well predict the

mechanical behavior of the structures due to the residual stress during material deposition.

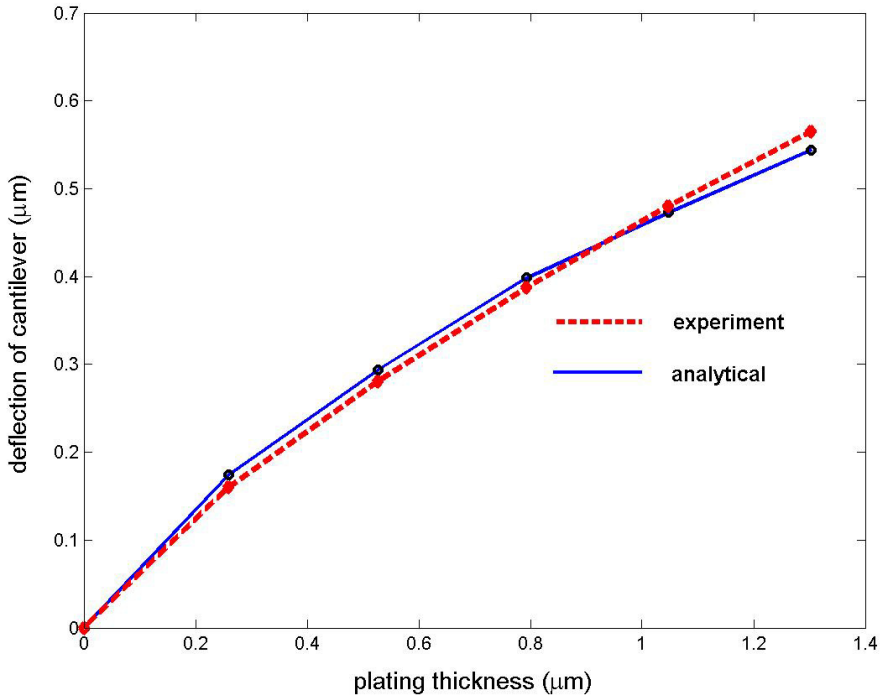

Fig. 57. Comparison of the cantilever deflection between analysis and experiment

Fig. 58 shows the comparison of the cantilever deflection during deposition between the cases when the reference mismatch strain is a constant and a function of out of plane location. The solid line indicates the approximately solved cantilever deflection which does not account for the through-thickness variation of the reference mismatch strain and has much difference comparing to the cantilever deflection which considers the through-thickness variation of the reference mismatch strain.

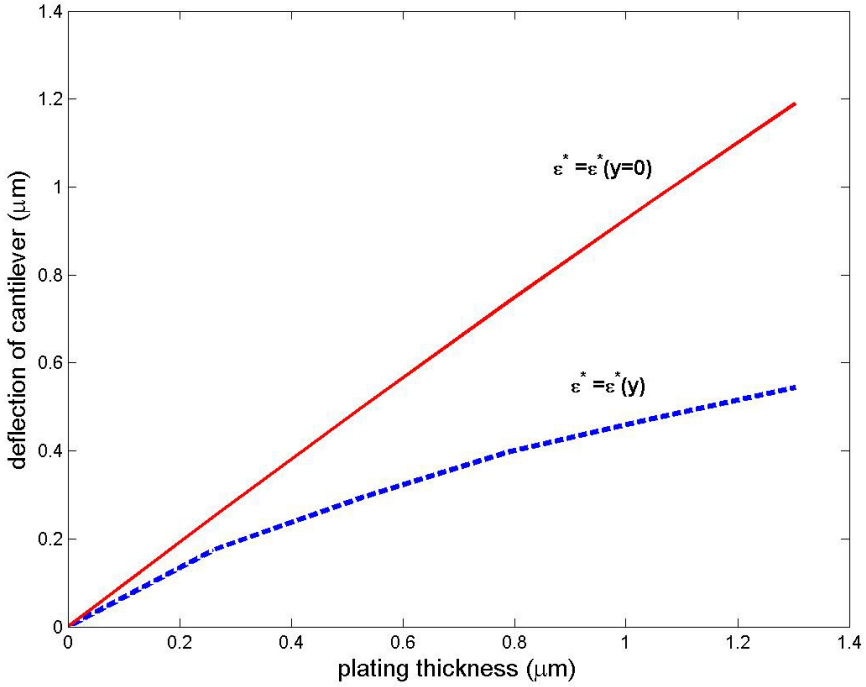

Fig. 58. Comparison of the cantilever deflection between the cases when the reference mismatch strain is a constant and a function of the out-of plane location

During deposition, the work done by the deposition cantilever on the spring cantilever is a monotonic function of the deposition thickness as shown in Fig. 59. That is to say that the work done increases with deposit thickness.

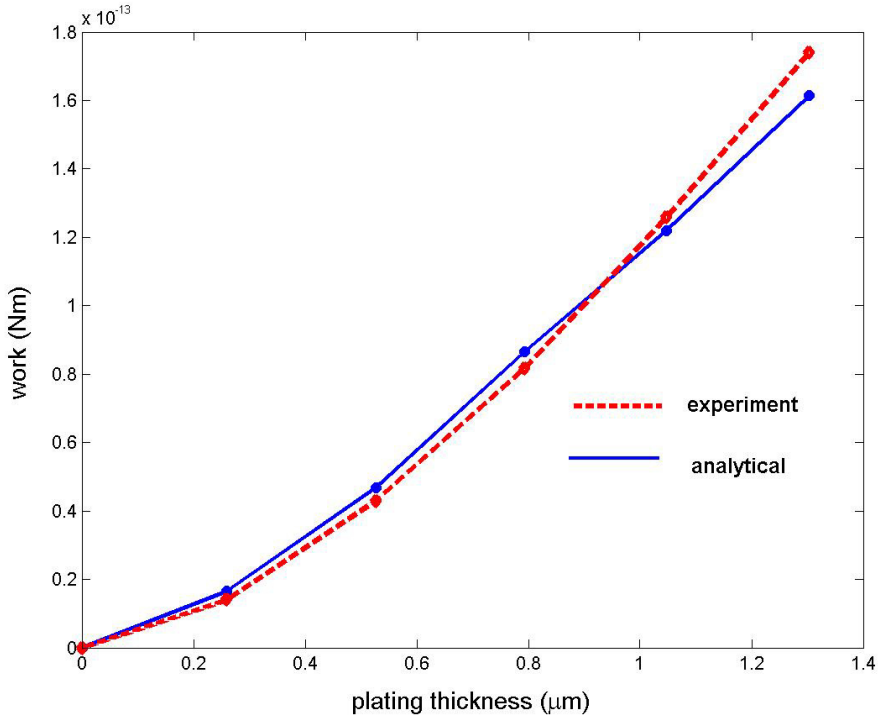

Fig. 59. Comparison of work done by the cantilever during deposition between analysis and experiment

Fig. 60 illustrates the cantilever deflection as a function of the plating thickness for various ratios of spring-to-deposition cantilever stiffness, c. It is seen that a stiffer spring (larger c) results in less cantilever deflection during deposition.

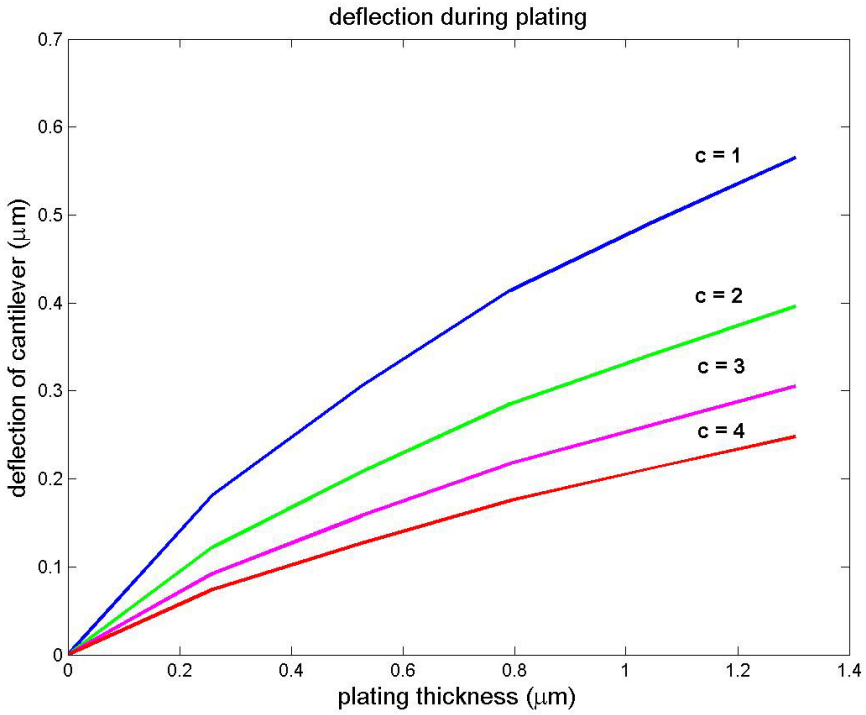

Fig. 60. Cantilever deflection for various ratios of spring-to-cantilever stiffness during deposition

VI. CONCLUSIONS AND FUTURE WORK

This thesis considered the possibility of using residual stresses favorably as a means of self-assembling MEMS during material deposition. A minimum criteria for self-assembly was that one beam must do work on another beam during material deposition. First, an analytical model was developed for the mechanics of an Euler-Bernoulli beam with moving boundaries during deposition, which accounts for the through-thickness variation of the mismatch strain. Second, the mismatch strain produced during the deposition was experimentally determined. Finally, it was experimentally demonstrated that residual stresses can be used to assemble two parts during material deposition.

The experiment consisted of two aligned AFM cantilevers. One was used for the deposition cantilever and the other was for the linear spring. Material was electroplated onto the deposition cantilever, which produced residual stresses that deformed the cantilever. This cantilever was attached to a second cantilever, the spring cantilever, that was not electroplated. The first cantilever did work on the second cantilever, thereby enabling the two structures to self-assemble. An isothermal insoluble nickel electroplating process and an all-sulfate nickel solution were used for the thin film deposition. The thickness of the film deposited on the deposition cantilever was measured using the stylus measurement method. The deflection of the self-assembled cantilevers was measured using the optical method of atomic force microscopy.

An uncertainty analysis, or sensitivity analysis, was performed to determine how uncertainties in measurands such as cantilever dimensions, air density, liquid damping, etc. affected functions of those measurands, such as cantilever stiffness and the elastic stiffness of the deposited nickel.

The results of the theoretical analysis and experiment are listed below:

1. The spring constants measured using Sadar's method which used the measured dimensions and the resonant frequencies of cantilevers have the accuracy of 2.5% comparing to the analytical spring constant calculated using Euler-Bernoulli beam theory.

2. The plating thicknesses measured in different plating time steps differ by no more than 5%. The measured plating thicknesses in different containers (beaker and liquid cell) are also similar and their maximum difference is less than 2%. The maximum difference of the plating thickness in each time step is less than 8%.

3. The measured elastic modulus of nickel in each plating time step is in the range of $163.48 \sim 176.29 GPa$ and the average elastic modulus is $171.31 GPa$, which is reasonable comparing to other experiment results in the literatures [55].

4. The measured total deflections of cantilevers increase with increasing plating time. The deflection of the cantilever with a low spring constant is greater than that with high spring constant. The rate of deflection of the cantilevers decreases with plating time for a constant plating current density.

5. The measured total deflection of aligned cantilevers increases with increasing plating time. The deflection of aligned cantilevers are less than that of the single cantilevers due to the spring cantilever working as the spring attached to the deposition cantilever. The rate of end deflection of aligned cantilevers decreases with plating time for a constant plating current density.

6. The numerically calculated reference mismatch strain decreases in the out-of-plane direction.

7. The analytically derived cantilever deflection agrees well with the experimentally measured deflection of two aligned cantilevers.

It is recommended that future work address three issues: 1) etching experiments; 2) torsional and translational motion; and 3) alternative deposition methods.

1. Etching experiments: The work reported herein was performed in part to experimentally validate the analytical model of Mani [27]. Mani analyzed self-assembly

by both material deposition and material removal, i.e. etching. However, the research reported herein consisted of only deposition, and not etching. Therefore, future research should experimentally verify the possibility of self-assembly during etching. The experiment could be performed by depositing material onto a deposition cantilever that is not attached to a spring cantilever. Then, after deposition is complete, the spring cantilever would be attached to the deposition cantilever, and the deposited layer would be etched away. The deposition cantilever would deform during etching and do work on the spring cantilever.

2. Torsion and translational motion: The analysis and experiments reported herein considered only bending deformations of a beam. However, torsional beam deformation and translational motion of generic structures may also be useful for self-assembly.

3. Alternative deposition methods: The deposition method used herein was electroforming. Other common deposition methods used in microfabrication include evaporation, sputtering, and chemical vapor deposition. Future work should verify that evaporation, sputtering, and chemical vapor deposition can be used to create residual stresses for self-assembly.

REFERENCES

[1] M. C. Wu, L.-Y. Lin, S.-S. Lee, and K. S. J. Psitor, "Micromachined free-space integrate micro-optics," *Sensors and Actuators*, vol. A50, pp. 127-134, 1995.

[2] N. C. Tien, O. Solgaard, M-H. Kiang, M. Daneman, K. Y. Lau, and R. S. Muller, "Surface-micromachined mirrors for laser-beam positioning," *Sensors and Actuators*, vol. A52, pp. 76-80, 1996.

[3] M. H. Kiang, O. Solgaard, R. S. Muller, and K. Y. Lau, "Silicon-micromachined micromirrors with integral high-precision actuators for external-cavity semiconductor laser," *IEEE Photonics Technology Letters*, vol. 8, no. 1, pp. 95-97, Jan. 1996.

[4] L. Fan, M. C. Wu, K. D. Choquette, and M. H. Crawford, "Self-assembled microactuated XYZ stages for optical scanning and alignment," *Transducers '97, 1997 International Conference on Solid-State Sensors and Actuators*, Chicago, IL, Jun.16-19, 1997, pp. 319-322.

[5] T. Akiyama, D. Collard, and H. Fujita, "Scratch drive actuator with mechanical links for self-assembly of three-dimensional MEMS," *Journal of Microelectromechanical Systems*, vol. 6, no. 1, pp. 10-17, Mar. 1997.

[6] J. R. Reid, V. M. Bright, and J. T. Butler, "Automated assembly of flip-up micromirrors," *Sensors and Actuators*, vol. A66, pp. 292-298, 1998.

[7] Y. W. Yi, and C. Liu, "Assembly of micro-optical devices using magnetic actuation," *Sensors and Actuators*, vol. 78, pp. 205-211, 1999.

[8] J. Zou, J. Chen, C. Liu, and J. E. Schutt-Aine, “Plastic deformation magnetic assembly (PDMA) of out-of-plane microstructures: Technology and Application,” *Journal of Microelectromechanical Systems*, vol. 10, no. 2, pp. 302-309, Jun. 2001.

[9] L. Li, J. Zawadzka, and D. Uttamchandani, “Integrated self-assembling and holding Technique applied to a 3-D MEMS variable optical attenuator,” *Journal of Microelectromechanical Systems*, vol. 13, no. 1, pp. 83-90, Feb. 2004.

[10] P. W. Green, R. R. A. Syms, and E. M. Yeatman, “Demonstration of three-dimensional microstructure self-assembly,” *Journal of Microelectromechanical Systems*, vol. 4, no. 4, pp. 170-176, Dec. 1995.

[11] R. R. A. Syms, “Rotational self-assembly of complex microstructures by the surface tension of glass,” *Sensors and Actuators*, vol. A65, pp. 238-243, 1998.

[12] K. F. Harsh, V. M. Bright, and Y. C. Lee, “Solder self-assembly for three-dimensional microelectromechanical systems,” *Sensors and Actuators*, vol. A77, pp. 237-244, 1999.

[13] K. F. Harsh, V. M. Bright, and Y. C. Lee, "Study of micro-scale limits of solder for MEMS self-assembly," *Proceedings of the 2000 Electronic Components and Technology Conference (ECTC 2000)*, Las Vegas, NV, May 21-24, 2000, pp. 1690-1695.

[14] R. R. A. Syms, C. Gormley, S. Blackstone, “Improving yield, accuracy and complexity in surface tension self-assembled MOEMS,” *Sensors and Actuators*, vol. A88, pp. 273-283, 2001.

[15] R. R. A. Syms, C. Gormley, "Surface tension powered self-assembly of 3-D micro-optomechanical structures," *Journal of Microelectromechanical Systems*, vol. 8, no. 4, pp. 448-455, Dec. 1999.

[16] T. Ebedors, E. Kalvesten and G. Stemme, "New small radius joints based on thermal shrinkage of polyimide in v-grooves for robust self-assembly 3D microstructures," *Journal of Micromechanics and Microengineering*, vol. 8, pp. 188-194, 1998.

[17] L. I. Maissel, and R. Glang, *Handbook of Thin Film Technology*, New York, NY: McGraw-Hill, 1983.

[18] L. Eckertova, *Physics of Thin Films*, New York, NY: Plenum Press, 1986.

[19] A. A. R. Elshabini-Riad, and F. D. Barlow, *Thin Film Technology Handbook*, New York, NY: McGraw-Hill, 1997.

[20] M. Ohring, *The Materials Science of Thin Films*, San Diego, CA: Academic Press, 1992.

[21] R. Koch, "Intrinsic stress of polycrystalline and epitaxial thin metal films," *Journal of Physics Condensed Matter*, vol. 6, pp. 9519-9550, 1994.

[22] M. Madou, *Fundamentals of Microfabrication*, Boca Raton, FL: CRC Press, Inc., 1993.

[23] J. N. Mitchell, and H. S. Hanson, "Investigation of micro electromechanical systems-fabricated actuators for use in optical and mechanical applications," *www.swri.edu*, IR&D Report, Accessed in October 2002.

[24] V. Y. Prinz, D. Grutzmacher, A. Beyer, C. David, B. Ketterer, and E. Deckardt, "A new technique for fabricating three-dimensional micro-and nanostructures of various shapes," *Nanotechnology*, vol.12, pp. 399-402, 2001.

[25] B. Min, D. A. Smith, H. Khan, F. L. Merat, A. H. Heuer, and S. M. Phillips, "Static and electrically actuated shaped MEMS mirrors," *Journal of Microelectromechanical Systems*, vol.14, no.1, pp.29-36, 2005.

[26] M. W. Judy, Y. H. Cho, R. T. Howe, and A. P. Pisano, "Self-adjusting microstructures (SAMS)," *Proceedings of IEEE Micro Electro Mechanical Systems, (MEMS '91)*, Nara, Japan, Jan. 30-Feb. 2, 1991, pp. 51-56.

[27] G. G. Stoney, "The tension of metallic films deposited by electrolysis," *Proceedings of the Royal Society of London*, *Series A*, vol. 82, pp. 172, 1909.

[28] L. B. Freund, "Some elementary connections between curvature and mismatch strain in compositionally graded thin films," *Journal of the Mechanics and Physics of Solids*, vol. 44, no. 5, pp. 723-736, 1996.

[29] S. Mani, "Residual stress and self-assembly during deposition and etching," M.S. Thesis, Texas A&M University, College Station, 2002.

[30] J. W. Dini, *Electrodeposition: the materials science of coatings and substrates*, Park Ridge, NJ: Noyes, 1993.

[31] M. Schlesinger and M. Paunovic, *Modern Electroplating*, 4th edition, New York, NY: John Wiley & Sons, Inc., 2000.

[32] W. A. Wesley, D. S. Carr, and E. J. Roehl, "Nickel plating with insoluble anodes," *Plating*, vol. 38, pp. 1243-1255, 1951.

[33] R. Weil, "The origins of stress in electrodeposits," *Platings*, vol. 57, pp. 1231-1237, 1970; vol. 58, pp. 137-146, 1971.

[34] Roberto Raiteri and Hans-Jurgen Butt, "Measuring electrochemically induced surface stress with an atomic force microscope," *Journal of Physical Chemistry*, vol. 99, pp. 15728-15732, 1995.

[35] T. A. Brunt, T. Rayment, S. J. O'Shea, and M. E. Welland, "Measuring the surface stresses in an electrochemically deposited metal monolayer: Pb on Au(111)," *Langmur*, vol. 12, pp. 5942-5946, 1996.

[36] H-J. Butt, "A sensitive method to measure changes in the surface stress of solids," *Journal of Colloid and Interface Science*, vol. 180, pp. 251-260, 1996.

[37] P. I. Oden, T. Thundat and R. J. Warmack, "Electrochemical deposition induced stress measurements on a microcantilever investigated with cyclic voltammetry", *Scanning Microscopy*, vol. 12, no. 3, pp. 449-454, 1998.

[38] A.S. Kobayashi, *Handbook on Experimental Mechanics*, Englewood Cliffs, NJ: Prentice-Hall, Inc., 1987.

[39] S. Basrour and L. Robert, "X-ray characterization of residual stresses in electroplated nickel used in LIGA technique," *Material Science & Engineering*, A288, pp. 270-274, 2000.

[40] J. P. Cleveland and S. Manne, "A nondestructive method for determining the spring constant of cantilevers for scanning force microscopy," *Review of Scientific Instruments*, vol. 64, pp. 403-405, 1993.

[41] S. Cherian and T. Thundat, "Determination of adsorption-induced variation in the spring constant of a microcantilever," *Applied Physics Letters*, vol. 80, no. 12, pp. 2219-2221, 2002.

[42] J. E. Sadar, "Method for the calibration of atomic force microscope cantilevers," *Review of Scientific Instruments*, vol. 66, pp. 3789-3798, 1995.

[43] S. J. O'Shea and M. E. Welland, "Atomic force microscopy stress sensors for studies in liquids," *Journal of Vacuum Science and Technology B*, vol. 14, pp. 1383-1385, 1996.

[44] D. A. Walters, J. P. Cleveland, N. H. Thomson, and P. K. Hansma, "Short cantilevers for atomic force microscopy," *Review of Scientific Instruments*, vol. 67, pp. 3583-3590, 1996.

[45] J. E. Sader, and L. White, "Theoretical analysis of the static deflection of plates for atomic force microscope applications," *Journal of Applied Physics*, vol. 74, pp. 1-9, 1993.

[46] J. E. Sadar, "Calibration of rectangular atomic force microscope cantilever," *Review of Scientific Instruments*, vol. 70, pp. 3967-3969, 1999.

[47] R. C. Weast, *CRC Handbook of Chemistry and Physics*, Boca Raton: FL: CRC Press, Inc., 1985.

[48] J. Sadar, "Frequency response of cantilever beams immersed in viscous fluids with applications to the atomic force microscope," *Journal of Applied Physics*, vol. 84, pp. 64-76, 1998.

[49] J. W. M. Chon, P. Mulvany, and J. E. Sadarr, "Experimental validation of theoretical models for the frequency response of atomic force microscope cantilever beams immersed in fluids," *Journal of Applied Physics*, vol. 87, no. 1, pp. 3978-3988, 2000.

[50] L. Rosenhead, *Laminar Boundary Layers*, Oxford, England: Clarendon, 1963.

[51] M. Abramowitz, and I. A. Stegun, *Handbook of Mathematical Functions*, New York, NY: Dover, 1972.

[52] R. J. King, M. J. Downs, P. B. Clapham, K. W. Raine, and S. P. Talim, "A comparison of methods for accurate film thickness measurement," *Journal of Physics E: Scientific Instruments*, vol. 5, pp. 445-449, 1972.

[53] A. Piegari, and E. Masetti, "Thin film thickness measurement: a comparison of various techniques," *Thin Solid Films*, vol. 124, pp. 249-257, 1985.

[54] *DEKTAK3 Installation, Operation and Maintenance Manual*, Revision 3.00, Vecco Metrology Group, Digital Instruments, Chadds Ford, PA.

[55] W. N. Sharpe, *MEMS Handbook: Chapter 3 – Mechanical Properties of MEMS Material*, Boca Raton, FL: CRC Press, Inc., 2002.

[56] R. F. Gibson, *Principles of Composite Material Mechanics*, New York, NY: McGraw-Hill, Inc, 1994.

[57] T. G. Beckwith, N. L. Buck, and R. D. Marangoni, *Mechanical Measurements,* 3rd edition, Reading, MA: Addison-Wesley, Inc., 1982.

[58] J. W. Wittwer, T. Gomm, and L. L. Howell, "Surface micromachined force guages: uncertainty and reliability," *Journal of Micromechanics and Microengineering*, vol. 12, pp. 13-20, 2002.

[59] A. Mawardi, and R. Pitchumani, "Design of microresonators under uncertainty," *Journal of Microelectromechanical System*, vol. 14, pp. 63-69, 2005.

[60] G. C. Johnson, P. T. Jones, and R. T. Howe, "Materials characterization for MEMS – a comparison of uniaxial and bending tests," *SPIE*, vol. 3874, p94-101, 1999.

[61] *Multimode SPM Instruction Manual*, Version 4.31ce, Vecco Metrology Group, Digital Instruments, Chadds Ford, PA.

[62] Y. Wang, R. Ballarini, H. Kahn, and A. H. Heuer, "Determination of the growth strain of LPCVD polysilicon," *Journal of Microelectromechanical Systems*, vol. 14, no. 1, pp. 160-166, Feb. 2005.

VITA

Sang-Hyun Kim

Dongnam Park 110
Youngju2-Dong, Jung-Gu,
Pusan, Korea 600-112

Education

2000 ~ 2005	Doctor of Philosophy in Aerospace Engineering Texas A&M University, College Station, TX.
1993 ~ 1995	Master of Science in Aerospace Engineering Pusan National University, Pusan, Korea.
1989 ~ 1993	Bachelor of Science in Aerospace Engineering Pusan National University, Pusan, Korea.

Work Experience

1995 ~ 2000	Research Engineer, Research & Development Team Aerospace Division, Korean Airline Co. Ltd.